30785

NATIONAL LIBRARY
OTTAWA

CANADA

BIBLIOTHÈQUE NATIONALE
OTTAWA

NAME OF AUTHOR....MYRON MORRIS OLESKIW.....

TITLE OF THESIS...SIMULATION OF GRAUPEL GROWTH IN A LABORATORY CLOUD CHAMBER

.....

UNIVERSITY.....UNIVERSITY OF ALBERTA.....

DEGREE FOR WHICH THESIS WAS PRESENTED...M. Sc.....

YEAR THIS DEGREE GRANTED.....1976.....

Permission is hereby granted to THE NATIONAL LIBRARY OF CANADA to microfilm this thesis and to lend or sell copies of the film.

The author reserves other publication rights, and neither the thesis nor extensive extracts from it may be printed or otherwise reproduced without the author's written permission.

(Signed)...Myron Oleskiw.....

PERMANENT ADDRESS:

...200 JUPITER RD....

...KELOWNA, B.C.....

.....

DATED...July 22.....1976

NL-91 (10-68)

INFORMATION TO USERS

THIS DISSERTATION HAS BEEN MICROFILMED EXACTLY AS RECEIVED

This copy was produced from a microfiche copy of the original document. The quality of the copy is heavily dependent upon the quality of the original thesis submitted for microfilming. Every effort has been made to ensure the highest quality of reproduction possible.

PLEASE NOTE: Some pages may have indistinct print. Filmed as received.

Canadian Theses Division
Cataloguing Branch
National Library of Canada
Ottawa, Canada K1A ON4

AVIS AUX USAGERS

LA THESE A ETE MICROFILMEE TELLE QUE NOUS L'AVONS RECUE

Cette copie a été faite à partir d'une microfiche du document original. La qualité de la copie dépend grandement de la qualité de la thèse soumise pour le microfilmage. Nous avons tout fait pour assurer une qualité supérieure de reproduction.

NOTA BENE: La qualité d'impression de certaines pages peut laisser à désirer. Microfilmee telle que nous l'avons reçue.

Division des thèses canadiennes
Direction du catalogage
Bibliothèque nationale du Canada
Ottawa, Canada K1A ON4

THE UNIVERSITY OF ALBERTA

SIMULATION OF GRAUPEL GROWTH IN A LABORATORY CLOUD CHAMBER

by

MYRON MORRIS OLESKIW ©

A THESIS

SUBMITTED TO THE FACULTY OF GRADUATE STUDIES AND RESEARCH

IN PARTIAL FULFILMENT OF THE REQUIREMENTS FOR THE DEGREE OF

MASTER OF SCIENCE

IN

METEOROLOGY

DEPARTMENT OF GEOGRAPHY

EDMONTON, ALBERTA

FALL, 1976

THE UNIVERSITY OF ALBERTA

FACULTY OF GRADUATE STUDIES AND RESEARCH

The undersigned certify that they have read, and recommend to the Faculty of Graduate Studies and Research, for acceptance, a thesis entitled "Simulation of Graupel Growth in a Laboratory Cloud Chamber", submitted by Myron Morris Oleskiw in partial fulfilment of the requirements for the degree of Master of Science in Meteorology.

Edward Lozowski
.....
Supervisor

Robert E. Stewart
.....

Leslie W. Lock
.....

Date June 25, 1976

DEDICATION

To my parents

whose encouragement, support, and understanding

over the years

have made this work possible

ABSTRACT

Recent studies have led some researchers to hypothesize a much more important role for graupel [1] in the hailstone and cold rain formation processes. This study investigates the potential for conical graupel formation on hexagonal plate ice crystals according to Knight and Knight's hypothesized process, by simulation of the appropriate growth conditions in a cloud chamber.

A survey of the literature was carried out to provide an insight into the physical conditions likely to occur during natural graupel formation. These conditions include the air temperature and humidity, the cloud droplet size distribution and water content, the dimensions of the hexagonal plate ice crystals, and the terminal velocities of these crystals and of conical graupel.

The simulation was carried out by propelling two growth substrates, located at the ends of a rotating boom, within a cloud chamber. A method for producing the 1 mm diameter, 50 μm thick hexagonal plates used as substrates,

[1] Graupel, or snow pellets, are small rimed ice particles with primarily their surface appearance, shape, and density distinguishing them from either snow flakes, or hailstones.

and a new technique developed by R. S. Babington for producing sprays of cloud-sized droplets are explained. The construction of such sprayers is also outlined.

The experiments have demonstrated that riming on hexagonal plates occurs first at the edge, and then primarily near the corners of the plate. Continued growth results in deposits fanning out into the wind with few, if any, common points of attachment, other than to the plate. The fragile nature of the growths results in a potential for breaking near their point of attachment, and then either pivoting outward about this point, or breaking completely away from the substrate.

Investigations into the quantitative aspects of the riming process have generally been less successful. The final two chapters include discussions on the probable causes of the problems encountered, and recommendations for improvements of the apparatus and the techniques employed in order to alleviate these problems.

ACKNOWLEDGEMENTS

I am indebted to various people and organizations whose cooperation and support have enabled me to complete this thesis.

My sincerest thanks go to my departmental supervisor, Dr. E. P. Lozowski, for his patience, understanding, and enthusiastic guidance throughout the period required to complete this degree. I also would like to thank Drs. R. B. Charlton and G. S. Lock for serving on my examining committee.

I wish to express my appreciation to Drs. Lock and R. R. Gilpin of the Mechanical Engineering Department for the use of one of their cold-rooms and their icing wind-tunnel; and to Dr. D. D. Cass of the Department of Botany for the use of his Zeiss Photomicroscope II with facility for Nomarski interference analysis.

I have had valuable discussions with Dr. R. S. Schemenauer, of the Atmospheric Environment Service, Toronto; and Dr. C.A. Knight of the National Center for Atmospheric Research, Boulder, Colorado. Many of my colleagues in the Meteorology Division have contributed suggestions during discussions I have held with them from

time to time. In particular I wish to acknowledge the aid provided by Mr. D. L. Oracheski in diagnosing problems that were encountered with the photographic synchronization unit. In addition, Mr. D. Sortland of the Atmospheric Environment Service, Edmonton, kindly contributed samples of graupel that he had carefully collected for me. Finally, Mrs. L. Smith, the Divisional Secretary, aided with the photocopying of this manuscript. To all of these people I wish to express my gratitude.

I would also like to thank the Atmospheric Environment Service, Environment Canada, for providing support in the form of a fellowship, and a research grant to the university.

TABLE OF CONTENTS

		Page
DEDICATION		iv
ABSTRACT		v
ACKNOWLEDGEMENTS		vii
TABLE OF CONTENTS		ix
LIST OF TABLES		xiii
LIST OF FIGURES		xv
LIST OF PHOTOGRAPHIC PLATES		xvii
CHAPTER		
I	INTRODUCTION	1
1.1	Background: Hailstone Embryos and Hail Suppression	1
1.2	The Definition of Graupel	4
1.3	The Formation and Growth of Conical Graupel	7
1.4	The Objectives of This Study	17
II	THE SIMULATION CONDITIONS	19
2.1	The Conditions Required for a Conical Graupel Growth Simulation	19
2.2	Air Temperature	21

CHAPTER		Page
2.3	Humidity	24
2.4	Ice and Cloud Condensation Nuclei	25
2.5	The Cloud Droplet Size Distribution and Water Content	25
2.6	Dimensions of Hexagonal Plate Ice Crystals	30
2.7	Ice Crystal and Graupel Terminal Velocities	32
2.8	A Summary of the Simulation Conditions	37
III	THE EXPERIMENTAL APPARATUS	39
3.1	An Overview of the Equipment	39
3.2	The Spraying System	40
3.3	The Hexagonal Plate Substrate and its Suspension	48
3.4	The Rotating Boom	51
3.5	The Cloud Chamber	56
3.6	The Cold-room	58
3.7	The Photographic System	58
3.8	Temperature Measurement	60
3.9	The Measurement of the Cloud Droplet Size Distribution	61
IV	THE TECHNIQUES EMPLOYED IN DATA ANALYSIS	66
4.1	The Calibration of Gelatin Coated Slides	66
4.2	The Determination of Cloud Droplet Water Concentration	71

CHAPTER		Page
4.3	The Determination of the Cloud Droplet Size Distribution	75
4.4	The Effects of Sublimation Upon the Determination of the Cloud Droplet Water Concentration	76
4.5	The Effects of Sublimation Upon the Hexagonal Plate Substrate	77
4.6	Determination of the Rate of Accretion on the Substrate	78
4.7	Determination of the Density of the Growths	79
V	THE RESULTS OF THE SIMULATIONS	80
5.1	The Onset and Early Stages of Accretion	80
5.2	The Qualitative Analysis of Accretion for Prolonged Periods	87
5.3	The Cloud Droplet Water Content and Size Distribution During the Prolonged Accretion Experiments	100
5.4	The Quantitative Analysis of Prolonged Accretion	106
VI	CONCLUSIONS AND RECOMMENDATIONS	118
6.1	A Summary of the Results	118
6.2	Conclusions	120
6.3	Recommendations for Future Studies of Graupel Formation	121
REFERENCES		125

APPENDIX		Page
A	DROPLET HEAT AND MASS TRANSFER CALCULATIONS	132
B	THE PHOTOGRAPHIC SYNCHRONIZER	136
C	DATA OBTAINED FROM THE CLOUD DROPLET DISTRIBUTION SLIDES	139
D	DATA ON THE CHARACTERISTICS OF THE PROLONGED GROWTH DEPOSITS	149
E	THE MAGONO AND LEE METEOROLOGICAL CLASSIFICATION OF SNOW CRYSTALS	162

LIST OF TABLES

TABLE		Page
1	The sprayer operating characteristics, and the parameters derived from the gelatin-coated slides	104
2	The parameters derived from the uncoated slides	104
3	Properties of the substrate accreted deposit	112
4	The mean linear growth rates and mass growth rates for the deposits	112
5	The mean frontal area of the growth along with Type 1 and 2 collection efficiencies	114
6 & 7	The data of calibration slides CAL. IA and IB respectively	140
8 & 9	The data of calibration slides CAL. IC and IIA respectively	141
10 & 11	The data of calibration slides CAL. IIA and IIB respectively	142
12 & 13	The data of calibration slides CAL. IIC and IIIA respectively	143
14	The data of calibration slide CAL. IIIB	144
15	A further analysis of calibration slide CAL. IIIA	145
16 & 17	A further analysis of calibration slide CAL. IIB, and the analyzed data from Slide 21 for SEQ. II, respectively	146

TABLE		Page
18 & 19	The analyzed data from Slide 19, SEQ. II′; and Slide 23, SEQ. VI, respectively	147
20 & 21	The analyzed data from Slide 27, SEQ. XII; and Slide 25, SEQ. XI, respectively	148
22 & 23	The rate of growth of the maximum length of the deposit during prolonged growth periods	150
24 & 25	As in Tables 22 and 23	151
26 & 27	As in Tables 22 and 23	152
28 & 29	As in Tables 22 and 23	153
30 & 31	As in Tables 22 and 23	154
32 & 33	As in Tables 22 and 23	155
34 & 35	The dimensions of the deposit as used for estimating its volume	156
36 & 37	As in Tables 34 and 35	157
38 & 39	As in Tables 34 and 35	158
40 & 41	As in Tables 34 and 35	159
42 & 43	As in Tables 34 and 35	160
44 & 45	As in Tables 34 and 35	161

LIST OF FIGURES

FIGURE		Page
1	Arenberg's hypothesized mode of conical graupel formation	9
2	Knight and Knight's suggested mode of origin of conical graupel	14
3	Distribution of the amounts of accretion, given as areal rime coverage, on planar and radiating crystals with graupel added to the 100+% rime coverage category	16
4	Cumulative mass distribution of cloud droplets in a cumulus cloud measured by Gagin (1975) through simultaneous use of a Formvar replicator and a sampler developed by CSIRO of Australia.	28
5	Cumulative mass distribution of cloud droplets as measured by McLeod (1976) at three levels in the updraft of an Alberta thunderstorm	29
6	Cumulative mass distribution of cloud droplets as measured by Christensen et al. (1974) in two Colorado prehail convective clouds	31
7	Variation with water sphere radius of the collision efficiency of an oblate spheroid of ice	32
8	The terminal velocity of hexagonal plate ice crystals (P1a), rimed hexagonal plates (R2a), and thick hexagonal plates (C1g) as a function of plate diameter	34

FIGURE		Page
9	The terminal velocity of conical graupel as a function of graupel base diameter	35
10	A schematic diagram outlining the principle of operation of the Babington nebulizer	41
11	The cumulative percentage of droplet number as a function of droplet diameter for the calibration runs of Case I	68
12	As in Fig. 11 except for the calibration runs of Case II	69
13	As in Fig. 11 except for the calibration runs of Case III	72
14	The percentage of mass contained in droplets smaller than or equal to a given diameter as a function of the diameter	102
15	The maximum length of the accreted deposit as a function of its time of growth	107
16	As in Fig. 15	108
17	As in Fig. 15	109
18	As in Fig. 15	110
19	A schematic diagram of the camera synchronizer	138
20a	The Nagono and Lee (1966) meteorological classification of snow crystals	163
20b	The continuation of Fig. 20a	164

LIST OF PHOTOGRAPHIC PLATES

PLATE		Page
1	A section through a conical graupel photographed using transmitted light	6
2	Cutting the slot in the glass sphere for the sprayer	44
3	The cloud droplet sprayer	45
4	The spray production system	46
5	A view of the manner in which the microtome was used to produce the nylon hexagonal plates	49
6	The boom as seen near the bottom of the cloud chamber	52
7	The equipment partition of the cloud chamber showing the motor, the balance wheel, and the camera trigger sensor and associated light source	54
8	The cloud chamber and associated equipment	56
9	Microscopic photograph of an oil-coated slide obtained with transmitted light showing the droplet diameters	65
10	Microscopic photograph of a gelatin-coated slide obtained with Normarski interference relected lighting showing the droplet crater diameters	65
11 & 12	Two views of the initial stages of riming at a velocity of 50 cm s^{-1}, with an air temperature of $-3.8^{o}C$, over a period of 5 min	81

PLATE		Page
13 & 14	As in Plates 11 and 12 except with a mean temperature of −19.4°C and over period of 8 s	82
15 & 16	As in Plates 11 and 12 except with a mean temperature of −15.2°C, and over a period of 60 s	84
17 & 18	As in Plates 11 and 12 except with a mean temperature of −7°C, and over a period of 4 min	85
19 & 20	As in Plates 15 and 16 execpt with a mean temperature of −9.5°C	86
21 & 22	As in Plates 15 and 16 except with a mean temperature of −21.5°C	86
23	A sequence of photographs taken at a mean air temperature of −5.4°C with no motion of the substrate	89
24	An enlarged form of Frame 23(3,4)	90
25	As in Plate 23 but with a mean temperature of −14.6°C and a substrate velocity of 50 cm s^{-1}	91
26	The continuation of Plate 25	92
27	An enlarged form of Frame 26(2,2)	93
28	As in Plate 23, but with a mean temperature of −15.4°C and a substrate velocity of 2.5 m s^{-1}	94
29	An enlarged form of Frame 28(3,5)	96
30	As in Plate 23 but with a needle rather than a hexagonal plate substrate	97
31	As in Plate 30 but with a mean temperature of −17.7°C and a velocity of 2.5 m s^{-1}	98
32	An enlarged form of Frame 31(3,1)	100

CHAPTER I

INTRODUCTION

1.1 Background: Hailstone Embryos and Hail Suppression.

Hailstorms are a significant component of the weather affecting the inhabitants of various continental areas throughout the world. Some of these regions are: the Prairie Provinces of Canada (and Alberta in particular); the High Plains of the United States Mid-West; the Central Plains of the United States; some of the valleys of Switzerland and Northern Italy; the high plains of Kenya and South Africa; and the plains of France, Argentina, Australia, and the Western USSR.

An estimated $300 million in annual crop and property damage was caused by hailstorms in the United States during the early 1970'S (Knight and Knight, 1971). For a typical year, this was claimed to be a greater financial loss than that due to tornados, although the latter are responsible for greater human injury and death. In Alberta, Wojtiw and Renick (1973) estimated the average annual agricultural loss due to hailstorms to be near $25 million. Further, they estimated that 80% of this damage occurs on an average of 12 days each summer (25% of the

average annual number of hail days).

In an effort to reduce the losses produced by these storms, scientific research programs were begun in many of the hail afflicted areas to determine the scientific and economic feasibility of hail suppression. Many of the techniques that have evolved from this research are dependent upon the competing embryo concept of hail suppression. This concept is based upon the production of a sufficient number of additional hailstone embryos so that the supposedly limited quantity of liquid water (in the form of supercooled cloud droplets, drizzle drops, and rain drops) available for hailstone growth will constrain the size of the hailstones formed. Through subsequent partial or complete melting of the stones during their fall to the earth, there will be less severe hail damage at the ground, despite an increase in the number of in-cloud stones produced.

The competing embryo concept was put on a quantitative basis by Iribarne and dePena (1960). More recent studies, by modelling clouds through computer simulation (Charlton and List, 1972; Dennis and Musil, 1973; Dennis, 1974) have refined the concept, leading to the following basic changes:

(i) early theories on accumulation zones [1] (Iribarne and dePena, 1960; Sulakvelidze et al., 1967; Kartsivadze, 1968), their spatial relation to the storm updraft maximum, and the significance of their contribution to hailstone formation have been questioned;

(ii) the production of competing embryos by silver iodide crystals interacting directly with cloud droplets in the storm's strong updraft is thought to be an insignificant means of modification (Dennis, 1975);

(iii) the hypothesis that a significant fraction of the water content available for hailstone production is depleted in an unmodified storm, or more importantly, that almost all of it would be depleted in a seeded storm, has been questioned (Browning and Foote, 1975).

Knight et al. (1974) have observed that 80% of the hailstones collected and analyzed following the passage of thunderstorms in Northeast Colorado had graupel embryos, while only 14% had originated from precipitation sized water drops. The embryos of the remainder were not determined. The primary natural process of precipitation formation in these types of clouds thus consists of:

(i) the growth of ice crystals by sublimation to a size

---

[1] The accumulation zone consists of a portion of the updraft of a storm where the proper combination of drop size and updraft velocity result in a continuing capture of smaller droplets rising in the updraft, leading to an intensification of water content in a region of about a kilometer in depth (Sulakvelidze et al., 1974; and Dennis, 1975).

sufficiently large to allow the accretion of cloud droplets;

(ii) riming to form graupel particles; and

(iii) further accretion of more or larger droplets resulting in hailstones.

The implication of these observations together with the refinement of the competition concept suggest that silver iodide nuclei should be introduced so as to result in the growth of graupel as an intermediate step in hailstone formation. The AgI injection should occupy the correct space-time location within feeder clouds of multicell storms (Dennis, 1975) or within the embryo curtain of supercell storms (Browning, 1975) in order to promote competition for the available cloud water within these regions, thereby reducing embryo size, and thus hailstone size.

1.2 The Definition of Graupel.

Having demonstrated the importance of graupel to the hail formation and thus the hail suppression mechanisms, it is useful to define graupel and to delimit its mechanism of formation in relation to the other solid precipitation particles.

According to Knight and Knight (1973), the word graupel has its origin in the German language, and has been derived from the word for barley or hulled grain, apparently because of the likeness of these grains to small graupel. Graupel occupies a distinct niche in the classifications of solid precipitation proposed by Nakaya (1951),

Schaefer (1951), The International Commision on Snow and Ice of 1951, and Magono and Lee (1966). However, in the classification scheme adopted through international agreement for use by various national weather services, this type of solid precipitation is termed a 'snow pellet'.

Graupel have been defined by Schemenauer (personal communication) as

> ...white opaque ice particles with maximum dimensions ranging from perhaps 0.35 mm to 7.5 mm and densities that are typically 0.25 g cm^{-3} to 0.70 g cm^{-3}. They may be hexagonal, conical or irregular in shape [as categorized in the classification schemes noted above] and are formed as a result of the heavy riming of cloud droplets on an ice particle (usually a snow crystal).... The surface of a graupel is dry and has the appearance of soft rime. The individual graupel are 'compressible' but not 'squishable'; ie. the softness of graupel is not due to the presence of liquid water but to the presence of numerous air spaces within the particle.

However, as noted above, growth upon ice crystals may not be the only mode, as List (1965, p.481) states: "Even if no scientific proof is available, it is expected (Browning, Ludlam, and Macklin, 1963) that graupel may also start from frozen cloud droplets...." In addition, graupel may be distinguished quite readily from snowflakes, when they are observed falling together, by their higher terminal velocity and by the fact that they tend to rebound following impact with a hard object.

An example of a section through a conical graupel is given in Plate 1.

Graupel are limited in their size range by two

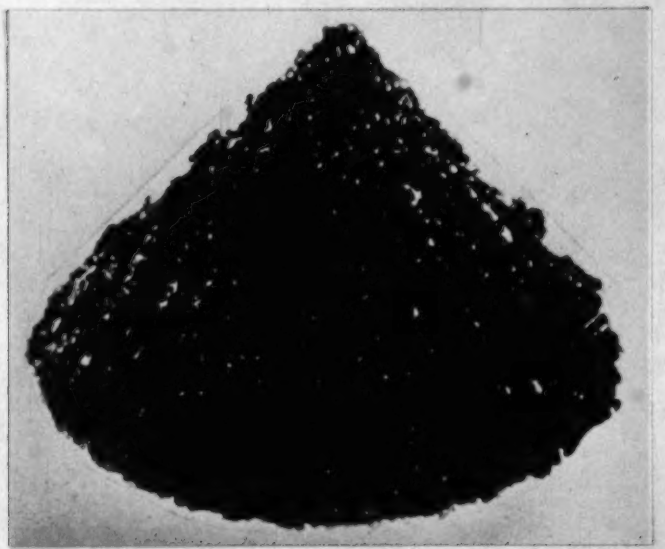

Plate 1. A section through a conical graupel photographed using transmitted light. The base diameter is 5.5 mm. (from List, 1960)

distinct factors. For those graupel originating on ice crystal kernels, the lower limit is defined by a rapid decrease in the collision efficiency of ice crystals for supercooled droplets as the size of the crystals falls below about 300 μm diameter. In a numerical investigation, Pitter and Pruppacher (1974) studied the accretion rates of simple ice crystal plates simulated by oblate spheroids, and discovered that the collision efficiency for 50 μm diameter droplets fell from about 0.8 for 800 μm plates to about 0.2 for 320 μm ones. In addition, plates of this latter size were able to collect droplets only within the 26 to 40 μm diameter range. Extrapolation from these results led them to conclude that plates smaller than about 250 μm in diameter would grow very little, if at all, by accretion.

The upper limit to the size range is defined by a change in the type of accretion from dry growth, to wet or just wet growth. As the graupel grows and its terminal velocity increases, both the rate of accretion and the kinetic energy imparted by the impacting droplets increase more rapidly than the ventilation effect. As a result the graupel surface temperature rises, leading to wet or just wet growth. The primary factor influencing this change is the increasing terminal velocity of the growing graupel, but other factors such as the air temperature, the air pressure, the graupel shape, cloud droplet and precipitation water content of the cloud, and the size distribution of the cloud droplets are also important. The features of the growth which change at this stage are the density, which rises as water flows into the relatively porous inner structure of the graupel and then freezes; and the surface appearance, which changes from matte to glassy. The particle then ceases to be defined as graupel, but should rather be termed small hail (Schemenauer, personal communication).

1.3 The Formation and Growth of Conical Graupel

As mentioned in the previous section, there are three types of graupel: conical, which shall be the primary concern of this paper; hexagonal; and irregular or lumpy. All varieties may occur in each of three situations: in winter snowstorms, where they will coexist with ice or snow crystals, either rimed or unrimed; in spring convective

showers where they may reach the ground in either a dry or wet form, the latter due to melting following formation; and in summer thunderstorms where they can be collected either by aircraft, or at the ground, in the form of hailstone embryos. Knight and Knight (1973) discuss their observations of the frequency of each type in each of these situations. The most important result for the purposes of this study is that conical graupel are found in all three situations. In addition they believe that the origin of each of the types of graupel does not vary substantially with the situation in which they are formed, that is, that the graupel formation mechanism is essentially constant throughout the year.

Knight and Knight (1973, p.118) conclude that "hexagonal graupel are obviously heavily rimed, hexagonal snow crystals that retain their general form. Lump graupel may be rimed spatial dendrites or any snow crystal that rimes while tumbling." While there may be some uncertainty as to whether lump graupel could form on frozen drops rather than crystals, it is the formation of conical graupel that has generated the greatest uncertainty, both as to the kernel upon which riming begins (if indeed one is required), and as to how the riming proceeds thereafter.

Six main theories have been advanced to explain conical graupel formation and growth, the only major agreement among them being that graupel are indeed formed by riming (Knight and Knight, 1973).

(i) One of the first comprehensive theories is due to Arenberg (1941). He proposed that the kernel is a plate-type ice crystal settling through a cloud of supercooled droplets and riming on the bottom. He expected that initially the rime accumulates most rapidly along the perimeter of the crystal (Fig. 1a,b), but that gradually accumulation occurs over the entire lower face (Fig. 1c). Because of the postulated flow field around the riming crystal, accretion gradually fills in the central portion and the deposit tapers to a point (Fig. 1d,e). As the

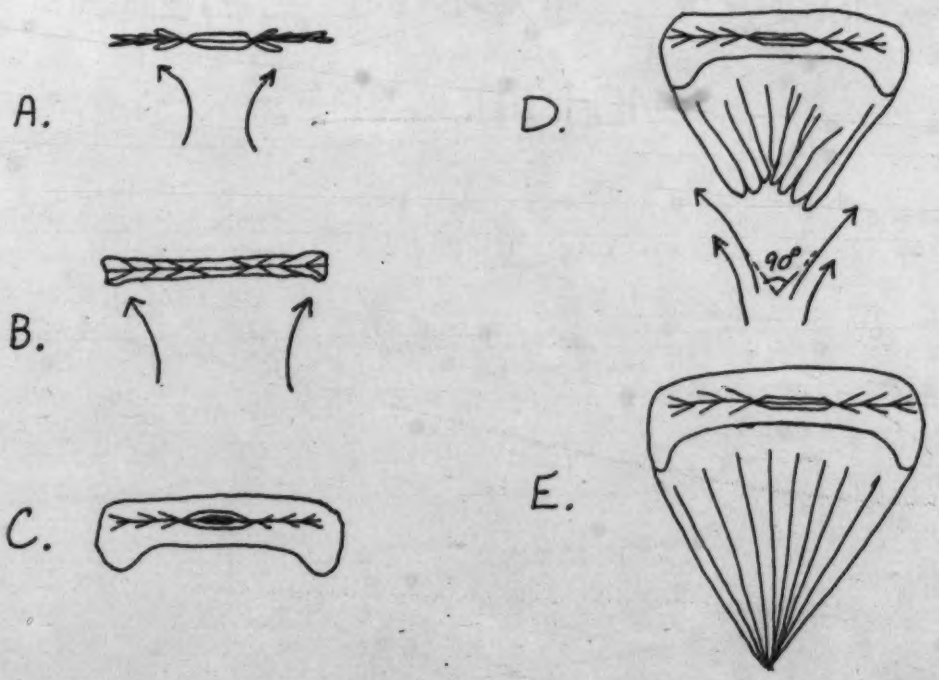

Figure 1. Arenberg's hypothesized mode of conical graupel formation.

growing graupel descends through the cloud, it encounters a decreasing mean size and number of droplets, and as a result the tip of the cone is composed of less dense rime, a feature observed in collected graupel. Arenberg suggests that the cone would be able to form in this manner, that is falling in its second most stable attitude (the first being point upward), because it assumes this position when riming begins, a time when there is little difference in stability between the two horizontal orientations. It is able to maintain the position because of a lack of sufficient turbulence to overturn it.

(ii) An alternate mechanism, suggested by Holroyd (1964), is based on accretion upon needle crystals. As the needles fall in a horizontal position (their most stable one), stochastic variations in riming rates lead to more rapid riming at one end than the other. This results in a more vertical orientation, and continued rapid riming at that end. As the riming needles fall past each other, they touch where widest (that is at the base end), and stick temporarily, since water droplet surface tension would keep them together long enough to allow the water to freeze. The air flowing past would then force the trailing tips together, and further collisions with other such needles, together with further riming, would lead to a conical graupel. Holroyd substantiated this mechanism by observations of graupel showers in which he noticed partially rimed conical graupel to be composed of two to six

rimed needles on one occasion, and to have a long, clear, needle sticking out of their apex, with little rime on this extended needle, on another occasion.

An implication of this theory is that while lumpy or hexagonal graupel must begin at temperatures of −16 to −20°C in order to form their ice crystal kernel, conical graupel could originate at warmer temperatures (−5 to −7°C), and lower cloud supersaturations.

(iii) The theory that has had the greatest acceptance amongst researchers in the field is that first advanced by Reynolds (1876). He expected that as a kernel in the form of a snow crystal fell through a cloud of supercooled droplets, riming would occur on the underside, "and as some of the particles would strike the face so close to the edge that they would overhang, the lower face would continually grow broader" (1876, p.164), with a conical graupel as the result. He also explained the increasing graupel density towards the base as due to the greater force with which cloud droplets were collected, driving them into a more compact mass, and resulting in a variation in density. Presumably in order to obtain a proper conical shape, with a pointed tip, some wake capture would have to take place if the embryonic droplet or crystal was larger than about 500 μm. The phenomenon of wake capture was studied by Sasyo (1971), but unfortunately the work was not sufficiently advanced to confirm or reject the hypothesis that sufficient wake capture occurs in order to produce the

conical tip. Knight and Knight (1973) and others, on the other hand, have frequently observed graupel to occur at the ground with the apexes truncated. While this would preclude the necessity of wake capture, sectioning of such graupel, as well as many others where the tips were intact, revealed extremely few cases which indicate the existence of a crystalline kernel. However, two pictures of hailstones suggesting such kernels are included in the paper by Knight and Knight (1973).

(iv) A variation of the preceding theory was advocated by Weickmann (1953), where the ice crystal kernel was replaced by a frozen droplet. Even in thin sections of graupel or hailstones formed on graupel, this type of kernel, if sufficiently small, would be indistinguishable from other droplets accreted later. However, Knight and Knight (1973, p.120) claimed, "riming on a frozen drop would be no faster than coalescence with an unfrozen drop of the same size. Therefore, it would seem that if riming of small frozen drops could proceed fast enough to make graupel, then coalescence should be proceeding at a good rate also, making supercooled water drops of substantial size." It is possible, however, that the large droplets might be eliminated through freezing or breakup.

(v) A suggestion that has not received much attention is that of Nakaya (1951, p.213): "The cone-like form [of graupel] R4c [1] is considered to be due to the rotational motion around the vertical axis during its fall." Because

no evidence has been presented to substantiate this mechanism, and no explanation is given as to the reason for such rotation, it remains as an idea that requires verification or dismissal based upon observations of the free-fall behavior of conical graupel.

(vi) Knight and Knight (1973) expect that accretion on a planar or dendritic crystal falling in its most stable position, that is with its axis of hexagonal symmetry vertical, will begin along the edge, and will be most pronounced at the corners. Evidence of the occurrence of this process is given in Fig. 8 of Pitter and Pruppacher (1974). The accreted growth will fan out into the wind in a fashion similar to that described by Reynolds (Fig. 2). This form is readily observed when accretion occurs upon stationary objects near the ground. The accretion will continue until conical graupel-like appendages are formed on the underside of the crystal. These will then break off, either singly, or in groups, and after additional riming, will result in conical graupel of varying sizes.

One of the problems with this explanation, as noted by the Knights themselves, is the lack of observational evidence of the intermediate stage of this process, that is of graupel-like appendages on the corners

---

[1] The use of this and similar codes refers to the solid precipitation (ice crystal) classification scheme of Magono and Lee (1966). This scheme is illustrated in Appendix E.

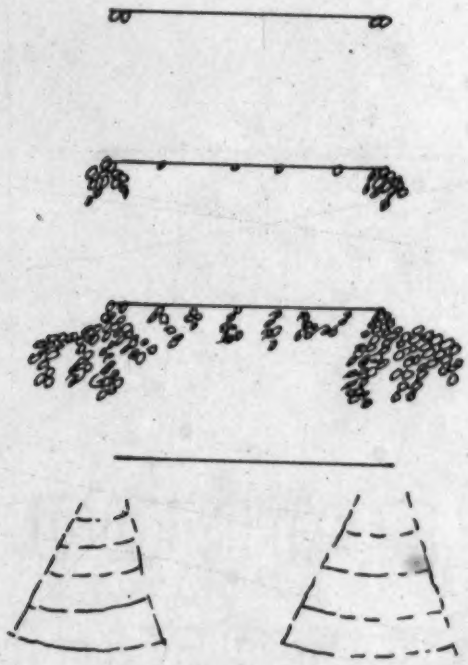

Figure 2. Knight and Knight's suggested mode of origin of conical graupel.

of the parent crystal. They suggest however, that while the apparent rarity of that stage may indeed by real, it may also be due to the great difficulty that would be experienced in attempting to observe it, as well as the lack of a previous effort to do so. Alternatively, "it is possible that in general only a modest rime development of this sort is necessary before breakage, and that much of the growth of some conical graupel takes place after breakage." (1973, p.123) This could explain the scarcity of observations of the intermediate stage.

Observations of the precipitation falling from Sierran convective snowstorms have allowed Reinking (1975) to draw some conclusions as to the relative merits of these

proposed methods of conical graupel formation. While there are differences between the conditions prevalent in these artificially seeded snowstorms and the conditions in High Plains thunderstorms, Reinking expects that the nature of the riming process should be very similar in both cases. Since two precipitation cases were observed accompanied by only needles, sheaths, and hollow columns, Reinking concludes that "the availability of planar crystals to serve as kernels is not prerequisite for graupel formation." (1975, p.749)

From Reinking's observations of the concentrations of the various types of solid precipitation (categorized according to Magono and Lee (1966)), he was able to determine the distribution of solid precipitation forms according to their maximum dimension and the areal rime coverage, visually estimated in six categories. The results for planar and radiating crystals with the graupel distribution added to the 100+% category are given in Fig. 3. From a point representing virtually 100% of the crystals at minimum size and no riming, the distribution broadens through the mid-ranges of rime coverage and crystal size, and then peaks more strongly, once again, at about 90% coverage on crystals 3.5 mm in size. Since this ridge in the distribution bypasses the mode of the graupel distribution, which is at 1.0 mm, Reinking concludes that the graupel cannot be generated by kernel crystals that grow for the longest times to the largest sizes by continual

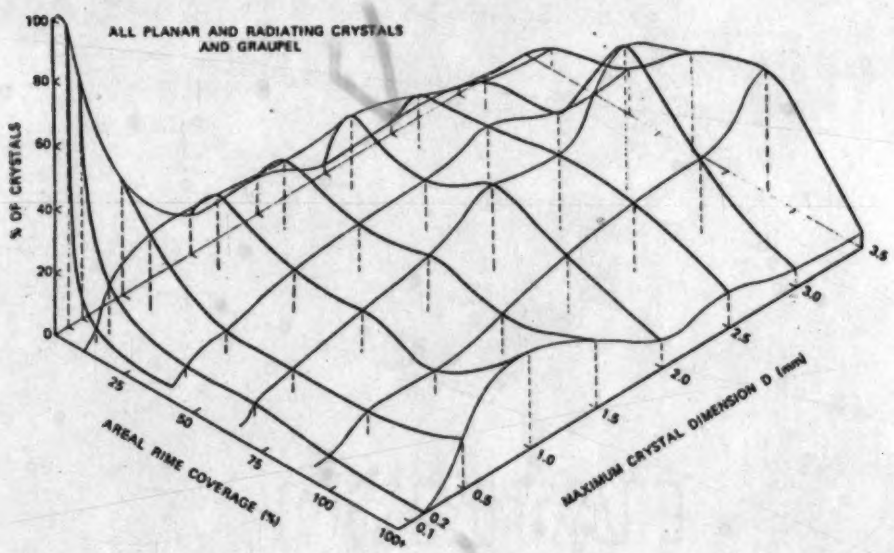

Figure 3. Distribution of the amounts of accretion, given as areal rime coverage, on planar and radiating crystals with graupel added to the 100+% rime coverage category. (after Reinking, 1975)

deposition and accretion, since such growths will make up the ridge in the distribution. Furthermore, there is a distinct minimum within the 75-100% rime category at 1.0 mm (and at adjacent sizes) which separates the main body of the distribution from the graupel distribution. If consistent slopes (no sign change) were apparent (along a given diameter) from the modal point for the crystals, to the 100+% category (for graupel), then it could be concluded that a process of elimination was occurring, "whereby some modal percentage of crystals that reach a given size collects a given amount of rime, a smaller percentage collects more rime, and still fewer collect enough rime to become graupel." (Reinking, 1975, p.752) From the data it may be estimated that a maximum of 25% of the graupel could

have formed in this way.

It appears that a basic underlying assumption in this argument is that there is no variation of the distributions with time, and furthermore that the ice crystals are forming in the same general region and are reaching the observer by similar trajectories. While such an assumption may be valid, Reinking does not present evidence to support it.

The formation of the remaining 75% of the graupel could be explained by theory (vi) since it "does not require graupel particles to be as large as the parent crystals..., and permits graupel to occur in greater numbers than the parent particles." (Reinking, 1975, p.753) It could thus also account for the separation between the mode for the 75-100% riming category occurring at 3.5 mm and the mode for the graupel at 1.0 mm.

1.4 The Objectives of This Study.

Knight and Knight (1973, p.124) concluded that "conical graupel are probably very important. Their commonness in convective storms in spring, and as hail embryos, suggests that in many cloud situations they are the fastest growing of all the precipitation forms. As such, they could be very important as a rain producing mechanism. A detailed, accurate, and reliable knowledge of their mode of origin could be most important in either rain-making or hail suppression."

This study is a contribution to an increase of that knowledge through the experimental simulation of the process of accretion of cloud droplets upon planar ice crystals. Aspects of the process that have been investigated include the onset of riming and the initial manner of accretion, the rate of growth of accreted material, the collection efficiency and density of the growth, and the variation of these aspects with variations in the growth temperature, and the terminal velocity of the crystal for relatively constant values of the cloud droplet size distribution and water content. [1] To the best of the author's knowledge, a similar investigation has not been carried out previously.

---

[1] For the purposes of this study, cloud droplet water content shall refer to the ratio of cloud droplet concentration to air density, and shall normally be expressed in g kg^{-1}. There will also be a distinction made between liquid water in the form of cloud droplets and in precipitation sized drops. The contribution of the former shall be referred to as cloud droplet water content, and the latter as precipitation water content.

CHAPTER II

THE SIMULATION CONDITIONS

2.1 The Conditions Required for a Conical Graupel Growth Simulation.

The laboratory conditions used for the simulation of graupel growth should be as close as possible to those expected in the graupel growth region of a cumulus or cumulonimbus cloud. The characteristics of the cloud which influence graupel growth are the air temperature and pressure, the humidity, the turbulence, the cloud droplet water content, the ice nuclei, the electric fields, the cloud condensation nuclei, the cloud droplet size distribution, and the electric charges on the cloud droplets, rain drops, and ice particles. The growth substrate must conform in shape, diameter, and thickness to a hexagonal plate ice crystal (Type P1a). In addition, the rate of flow of air past the substrate should duplicate a plate's terminal velocity both initially, and following the initiation of riming. Each of these characteristics shall be dealt with in the following sections of this chapter.

A difficulty in achieving accurate simulation arises from the paucity of field observations available for

most of the above-mentioned cloud characteristics in the graupel growth region. The best data of this type are those obtained by aircraft. However the factors of high capital and operating costs for the instrument platform; the difficulty of maintaining the operational readiness of aircraft, instruments and associated personnel; the time-consuming task of data reduction involved with many of the instruments; and the hazard involved in making such measurements, particularly in areas associated with developing cumulonimbus clouds, have all contributed to the scarcity of data. The situation regarding ice crystal and graupel characteristics is somewhat better, because measurements of these characteristics have been possible at high altitude laboratories during winter graupel growth conditions (Locatelli and Hobbs, 1974; Zikmunda and Vali, 1972). However once again the very slow process of data reduction necessitated by individual measurements of crystal dimensions, percentage of riming, and terminal velocity, has resulted in a small data base from which to make generalizations and draw conclusions. As a result of this situation, it has been necessary to draw upon a variety of sources for information regarding the properties of those clouds which might be suitable for the formation of graupel. In some cases, no graupel were actually detected, but in the observer's judgement, the properties of the cloud were suitable for graupel formation. Where graupel was observed, it was generally not classified as to its type ie. conical,

hexagonal, or lumpy.

2.2 Air Temperature.

Hobbs (1975) has measured the temperature of winter cumulus clouds embedded within stratiform orographic clouds during the passage of a front. He found that portions of the cloud at temperatures above about -8°C, frequently contained only supercooled water droplets. Between -8 and -14°C, rimed and unrimed frozen drops, irregular ice particles, dendrites and stellars were found. Graupel were also common, particularly along the western slopes of the mountains in Washington State. Unfortunately these data are not conclusive because the graupel could have formed either at higher levels, and have descended (while growing) to the collection point; or at levels below the observation location and have been orographically and convectively lifted to the observation location.

Christensen et al. (1974) have penetrated prehail convective clouds in Colorado to determine ice crystal concentrations. They discovered that at the -15°C level in a cumulus cloud which was rising through an ice cloud, there were regions of about 300 m along the flight path with ice completely absent. It appeared that the ice crystals had been mixed in only at the edges of the cumulus cloud, and were rimed there. Also observed were large regions of cumulus clouds at temperatures as low as -22°C where the ice particle concentration was below the detection limit of

their 16 mm Formvar particle replicator (capable of measuring 1 particle per 40 l of air), while the cloud droplet liquid water content was as high as 4 g m^{-3}. On the other hand, glaciation of receding towers was apparent from visual observations once the ascending tower had reached −25°C.

An investigation of the concentrations of ice nuclei, ice crystals, and graupel as well as of the air temperature of winter cumuli in Israel has been carried out by Gagin (1975). He determined that the cloud base is generally at about 750 m MSL and 8°C, while the mode of the cloud top height and temperature distribution is at 5.5 km and −20°C. The freezing level is commonly below 1.8 km. Since the ice concentration measurements were made by penetration of the clouds not more than 300 m below the cloud top, the resulting distribution of graupel concentration with temperature is actually also a function of cloud top height and thus cloud thickness. Gagin found that the graupel concentrations as measured by the continuous formvar sampler are less than 10^{-3} l^{-1} at temperatures less than −10°C, but that they rise to between 0.1 and 1.0 l^{-1} at −20°C. The observed graupel concentration is roughly one order of magnitude lower than the total ice crystal concentration. Furthermore, it increases at the rate of about one order of magnitude for every drop in temperature of 5°C. It should be noted though, that this temperature decrease is related to an

increase in cloud top height and cloud thickness.

The ice crystal concentrations are supported by the observations of Cannon and Sartor (1974) made from an instrumented sailplane flying through Colorado cumuli. Their measurements, made using a particle decelerator, show the ice particle concentration to vary from 5.3 l^{-1} near the cloud base (-2°C), to as high as 500 l^{-1} at 7.3 km and -18°C. In these clouds with tops at the -20°C level, Cannon and Sartor collected graupel and supercooled cloud droplets along with the ice crystals. They mention that the ice crystals and graupel appeared to be falling from above, and that the ice crystal concentrations near the top of the cloud were up to two orders of magnitude higher than those near the cloud base. They then conclude that "the smaller ice particle sizes, size ranges and much higher concentrations in the upper portions suggest that this is where the new ice particles are forming in the greatest numbers." (1974, p.127)

Dye (1974), and Knight et al. (1974) have described their penetrations of spring and summer Colorado cumuli with an instrumented sailplane. The height of graupel collection varied from just above the freezing level, to as high as 6.1 km MSL (at -9°C and 1.4 km above cloud base), the graupel collected being about 3 mm in diameter. In addition some graupel was collected in virga at temperatures above freezing. For this case the radar echo top of the cloud was above 8 km, which corresponded to

a temperature below -20°C.

In a paper recently submitted to The Journal of the Atmospheric Sciences, Knight et al. (personal communication) describe their observations of a rapid change in the crystal size found within artificially grown hailstones. This sharp transition from large to small crystals as the deposit cools through -15±2°C, has been found to be essentially independent of the drop size distribution, the air flow velocity past the growth, or the liquid water content of the air, provided that these parameters were within the ranges to be expected in natural conditions. Using these results, they examined graupel and small hail that had fallen from NE Colorado storms, and were able to conclude that many graupel had indeed passed through the -15°C level during their trajectories within the clouds.

2.3 Humidity.

Except in regions of entrainment near the edges of graupel producing clouds, the relative humidity of the air (with respect to a plane surface of pure water) is expected to be in the range of 100.1 to 101%. This corresponds to a supersaturation with respect to ice of up to 40% ie. sufficiently high to account for the growth of cloud droplets (and ice crystals, where ice nuclei exist, or the temperature is low enough). Of course, such droplet growth would also act to restrain a rise in the supersaturation.

2.4 Ice and Cloud Condensation Nuclei.

The concentrations of these nuclei are very important in determining the rate of production of graupel through their influence upon the production of the droplets or ice crystals from which the graupel form. However, this study will deal with the aspects of graupel growth following the formation of hexagonal plate ice crystals and a droplet distribution with a mass median diameter of near 10 μm. Thus the manner in which the crystals and the droplet distribution formed will not be of immediate concern.

2.5 The Cloud Droplet Size Distribution and Water Content.

The cloud droplet size distribution, concentration, and cloud droplet water content appear to be highly variable within graupel producing clouds. This variation is due to a number of factors. Some of them are: the temperature and humidity of the air parcel within the cloud; the cloud condensation nuclei available in the environment (their concentration and size are dependent to some extent upon the proximity to a body of salt water); the ice nuclei present; and the length of time over which the droplets have been able to grow from the vapor, and have been scavenged through accretion upon falling ice crystals, or through coalescence with raindrops.

The liquid water content of the graupel forming winter clouds examined by Hobbs (1975) varied from 0.5 to 2.0 g m^{-3} up to the 5 km level (at about $-20^{\circ}C$).

Ryan et al. (1972) used a cloud particle spectrometer to measure the distribution in a partially glaciated continental cumulus. They found that at the penetration level (5.55 km, -9.4°C) the cloud droplet water content varied from 0.02 to 0.3 g m^{-3}, while the concentration of droplets greater than 17 μm in diameter remained less than 0.1 cm^{-3} (μm radius interval)$^{-1}$. The cloud base and top were at the 4.7 and 6.1 km levels respectively.

The sailplane measurements of Cannon and Sartor (1974) show that at mid-levels (5.7 km and -7.5°C) in NE Colorado cumuli, the cloud droplets are distributed exponentially with diameter, the largest droplets generally being less than 22 μm in diameter. The droplet concentration is typically about 500 to 1000 l^{-1} resulting in a typical cloud droplet water content of 0.2 g m^{-3}. Dye et al. (1974) note that large droplets were encountered only very rarely, and in fact thin sections of graupel collected from such storms show no frozen water drops as large as 300 μm in diameter. In another paper, Dye (1974) states that examination of rimed ice which was collected from clouds with base and top temperatures of 2°C and less than -20°C respectively, shows that the largest droplets were on the order of 60 μm diameter. The cloud droplet water content of the upper part of these clouds was about 0.35 g m^{-3}. Fowler et al. (1974), using an optical cloud particle spectrometer mounted on a light plane, have found

that in small, fair weather cumuli, the cloud droplets were fairly equally distributed in the range of 5 to 20 μm diameter with the largest droplets $\leq$50 μm in diameter. For large towering cumuli, the diameters ranged up to 110 μm.

The penetrations by Gagin (1975) of winter continental cumuli in Israel, which in most aspects are very similar to the spring and summer cumulus clouds of NE Colorado (Dye, 1974), revealed that the concentration of droplets with diameters between 25 and 35 μm was less than 1 cm^{-3} for all temperatures warmer than $-8°C$, but that it rose to as high as 100 cm^{-3} for $-8 < T < -12°C$. In one particular case (at 470 m below the 4370 m top of a towering cumulus), the distribution of cloud droplets, expressed as the percentage of total droplet mass contributed by droplets smaller than or equal to a given diameter, was that shown in Fig. 4.

McLeod (1976) has made measurements of the droplet size distribution in the lower portions of the updraft region in a developing Alberta thunderstorm. The data for three levels in this storm are shown in Fig. 5. The mass median diameter at the lowest level, about 3.7 μm, is one of the smallest yet measured. It is thought that this is due to the lack of time available for the droplets to grow while rising in the relatively fast updraft from their formation region, at cloud base. It is seen that the mass median diameter increases with height in the cloud.

Christensen et al. (1974), in penetrations of

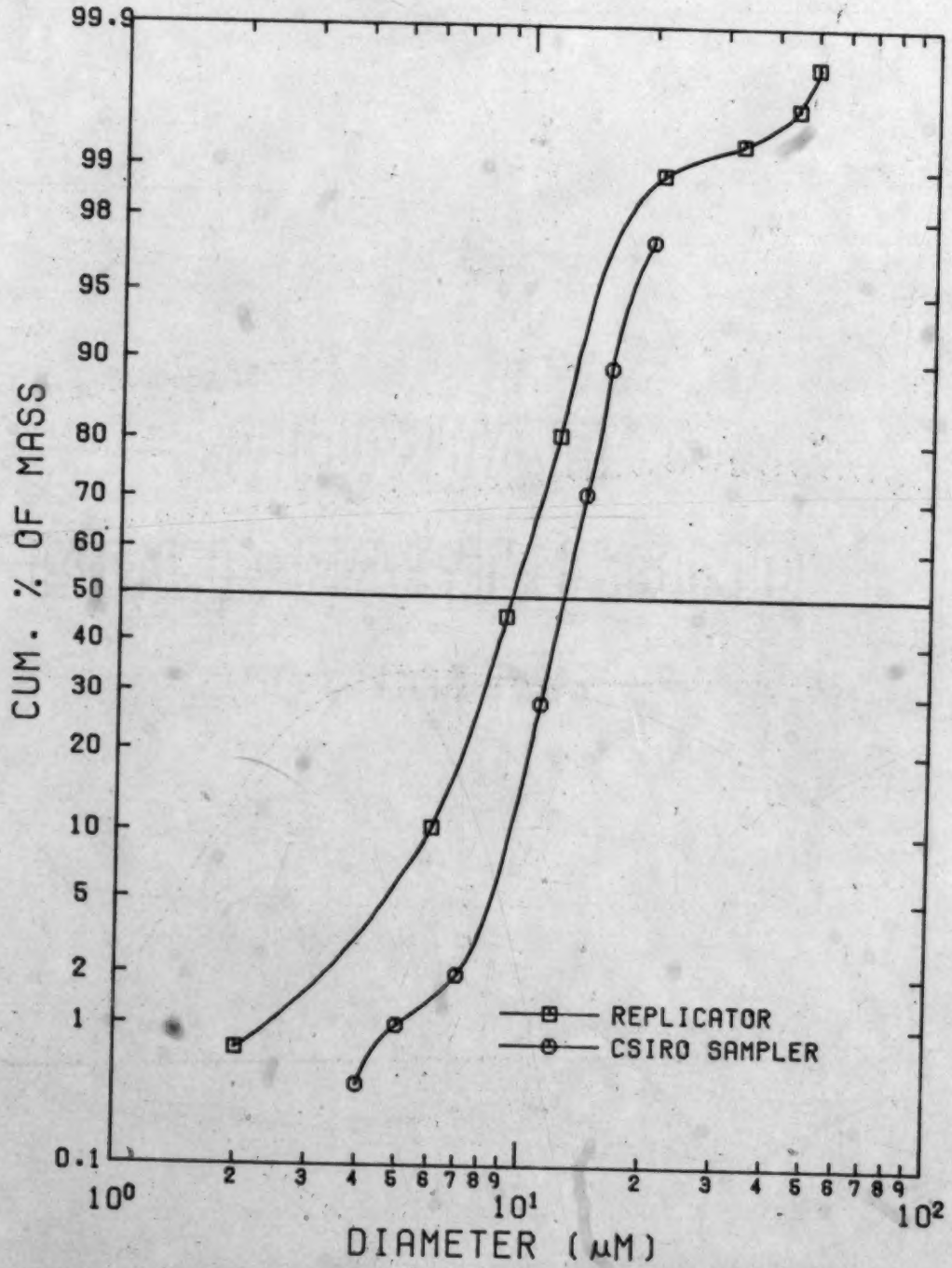

Figure 4. Cumulative mass distribution of cloud droplets in a cumulus cloud measured by Gagin (1975) through simultaneous use of a Formvar replicator and a sampler developed by CSIRO of Australia. The mass median diameters are 9.2 and 12.4 μm.

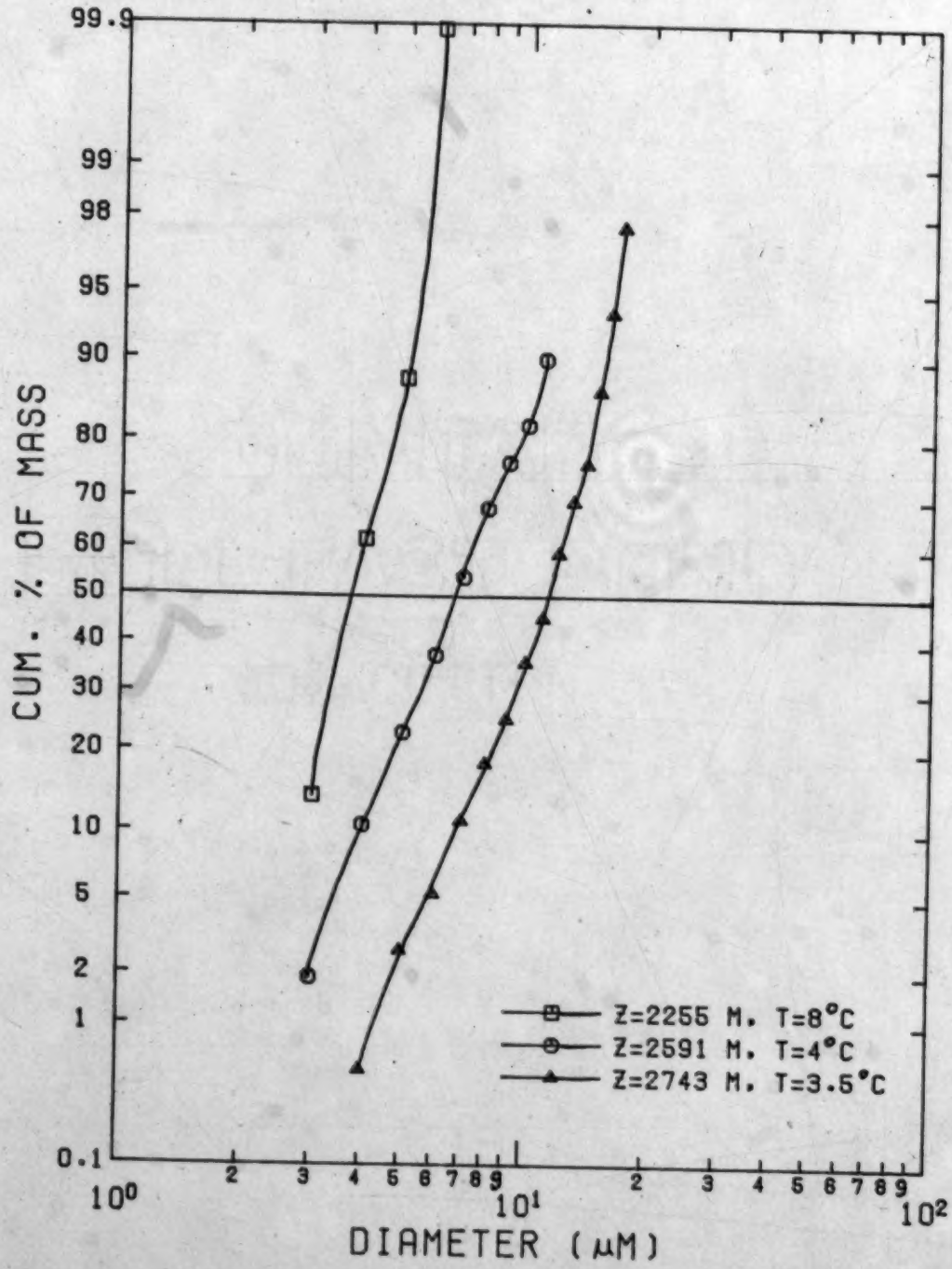

Figure 5. Cumulative mass distribution of cloud droplets as measured by McLeod (1976) at three levels in the updraft of an Alberta thunderstorm. The mass median diameters are 3.7, 6.6, and 11.5 μm.

Colorado prehail convective clouds lying between the -2°C and -25°C levels, detected the cloud droplet distributions shown in Fig. 6. The mass median diameters at two levels within these clouds were 14.8 and 23.5 μm. The cloud droplet water content rose as high as 4.0 g m^{-3} at the -14.2°C level.

2.6 Dimensions of Hexagonal Plate Ice Crystals.

Auer and Veal (1970) have made observations of the dimensions of hexagonal plate ice crystals occurring in orographic and cumuliform clouds. They found the diameter of such crystals to vary from about 2 μm to just over 1 mm, the most common size being of the order of 100 μm. From their observations, they were able to determine the following 'best fit' relationship for the crystal thickness as a function of diameter, (both h and d in μm)

$$h = 2.02\, d^{0.449} \qquad (2.1)$$

Thus a 1 mm plate should be 45 μm thick, and a 500 μm plate, 33 μm in thickness.

A theoretical study of the riming properties of hexagonal plate ice crystals (as simulated by oblate spheroids of high eccentricity) was carried out by Pitter and Pruppacher (1974). Their results, as shown in Fig. 7, indicate that for a plate with radius a_L, there is a limited range of droplet radii over which the collision efficiency of the plate is non-zero. This result is significant in

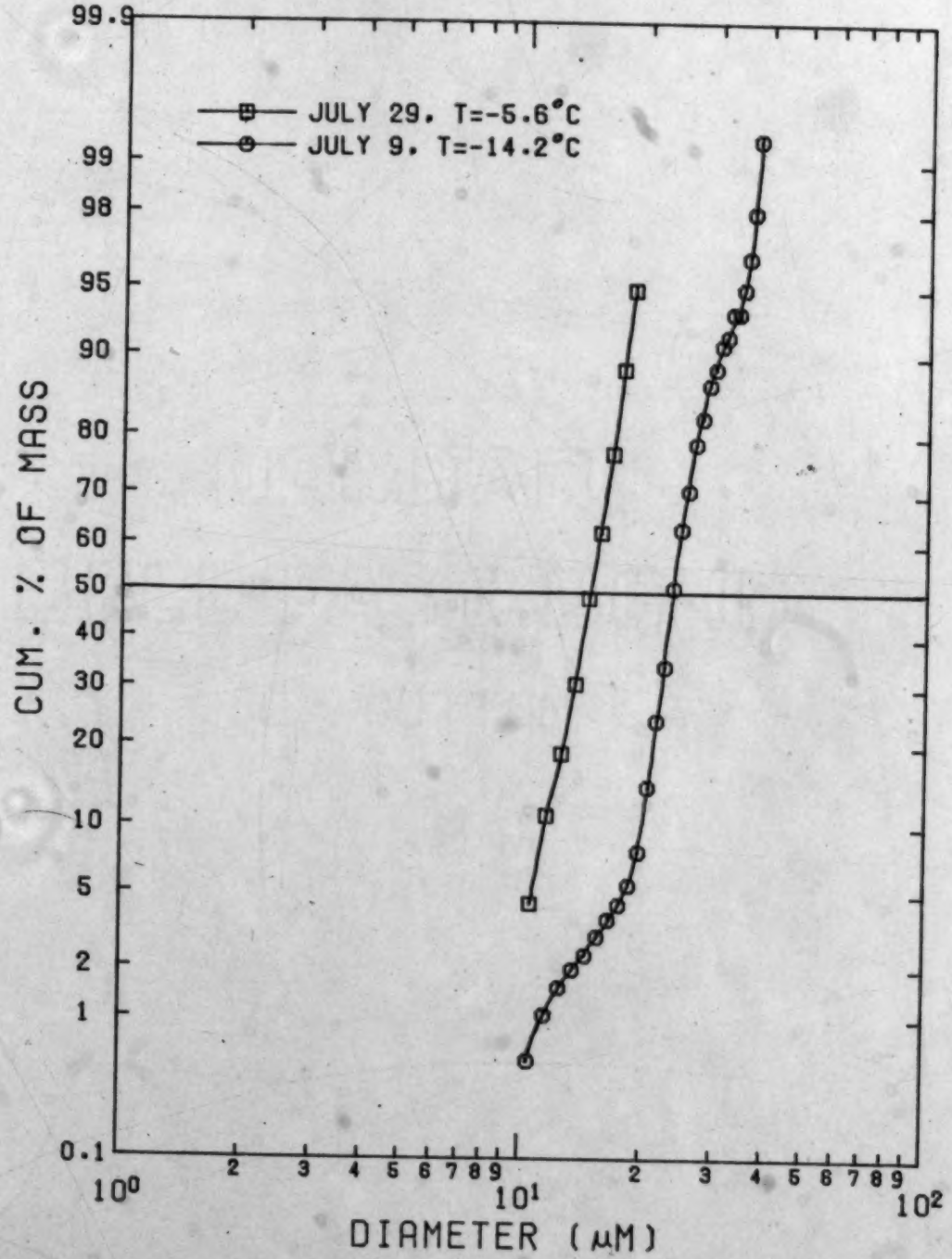

Figure 6. Cumulative mass distribution of cloud droplets as measured by Christensen et al. (1974) in two Colorado prehail convective clouds. The mass median diameters are 14.8 and 23.5 μm. The contribution of droplets smaller than 8 μm diameter has not been taken into account.

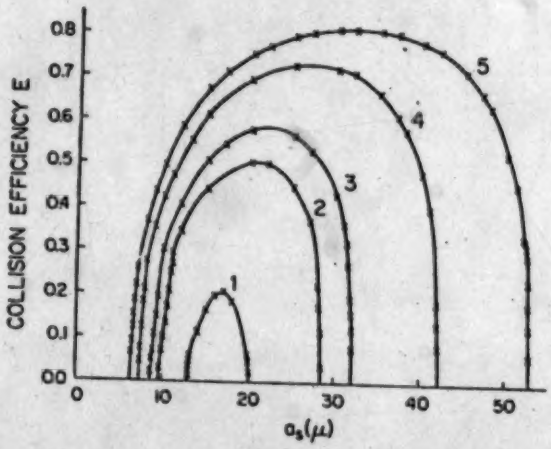

Figure 7. Variation with water sphere radius of the collision efficiency of an oblate spheroid of ice: (1) a_L=160, (2) a_L=194, (3) a_L=213, (4) a_L=289, (5) a_L=404 μm. (after Pitter and Pruppacher, 1974)

that it implies that the efficiency with which a hexagonal plate collects 20 μm radius droplets, for example, increases as the radius of the plate increases. Furthermore, as the plate size increases, the ability to collect smaller and larger drops also increases. An extrapolation of their results has led Pitter and Pruppacher to predict that riming upon hexagonal plates should not begin until the plate has grown by diffusion to a diameter of about 250 μm.

2.7 Ice Crystal and Graupel Terminal Velocities.

Zikmunda and Vali (1972) have used a stereoscopic camera system with stroboscopic illumination to measure the terminal velocities of various types of ice crystals and graupel during their fall through an outdoor coldroom at a high altitude observatory. Their fitted curves for the terminal velocities of densely rimed hexagonal plates (R2a)

and for conical graupel (R4c) are given in Figs. 8 and 9 respectively.

Heymsfield (1972) used drag coefficients determined by Jayaweera and Cottis (1969), aspect ratios determined by Auer and Veal (1970), as well as his own observations of plate density, to calculate the terminal velocity for hexagonal plates. His values are given in Fig. 8.

Combining the terminal velocity data of Bashkirova and Pershina (1964), Fukuta (1969), Jayaweera and Ryan (1972), Kajikawa (1972), and Zikmunda and Vali (1972), along with their own observations of the terminal velocities of hexagonal plates (P1a) and thick hexagonal plates (C1g), Davis and Auer (1974) derived the velocity-dimension relationships displayed in Fig. 8.

List and Schemenauer (1971) investigated the free-fall behavior of hexagonal plates and conical graupel by simulating the fall of these solid precipitation particles with idealized models falling in fluids of varying viscosity to achieve the appropriate Best number. They then presented 'best fit' curves giving the Best number versus Reynolds number relations for hexagonal plates, various models of conical graupel, as well as other crystalline forms. A transformation of these data into terminal velocity versus diameter relationships has been carried out. The results for hexagonal plates, and for cone-spherical sectors with apex angles of 70 and 90 degrees are given in

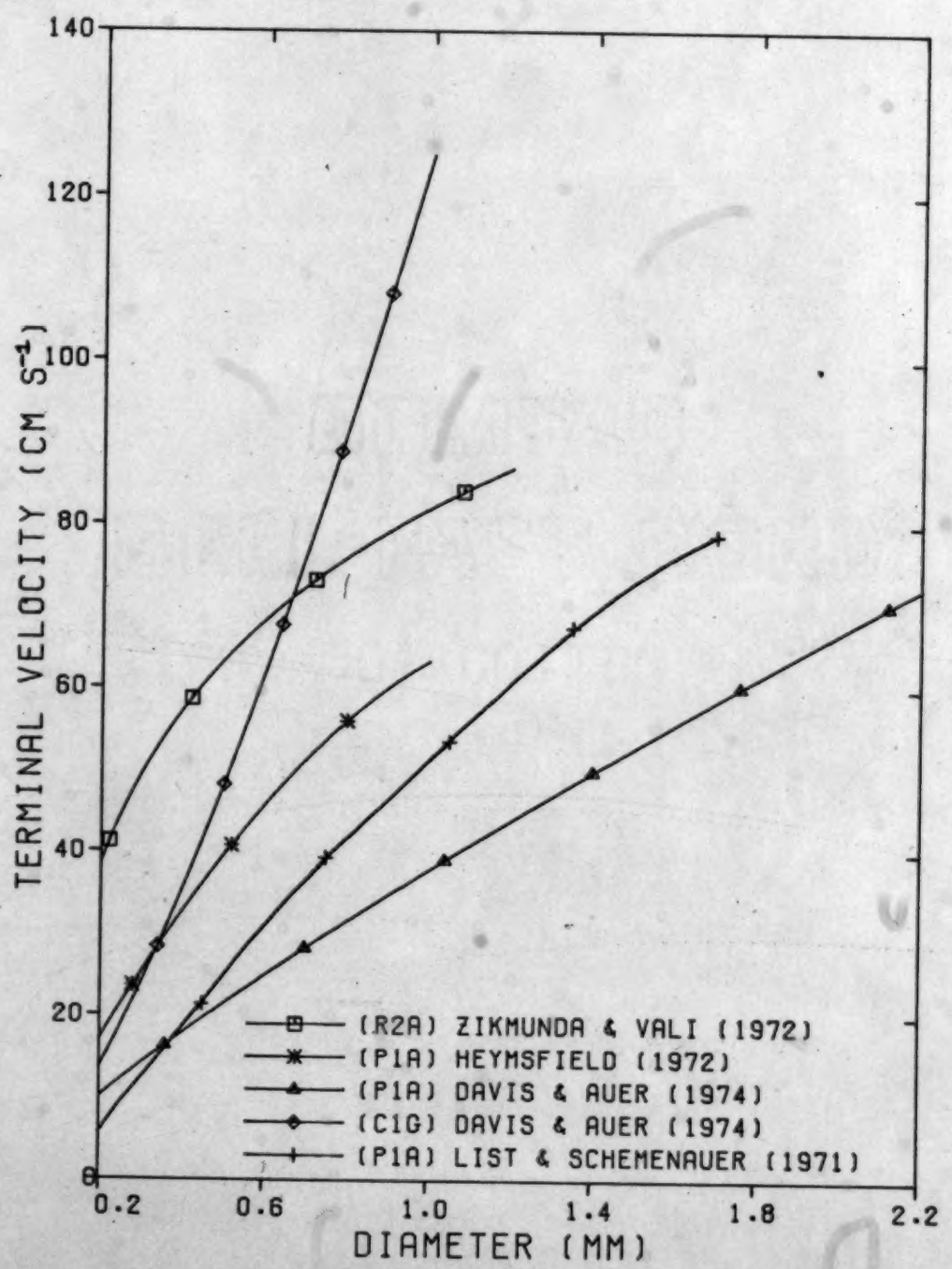

Figure 8. The terminal velocity of hexagonal plate ice crystals (P1a), rimed hexagonal plates (R2a), and thick hexagonal plates (C1g) as a function of plate diameter.

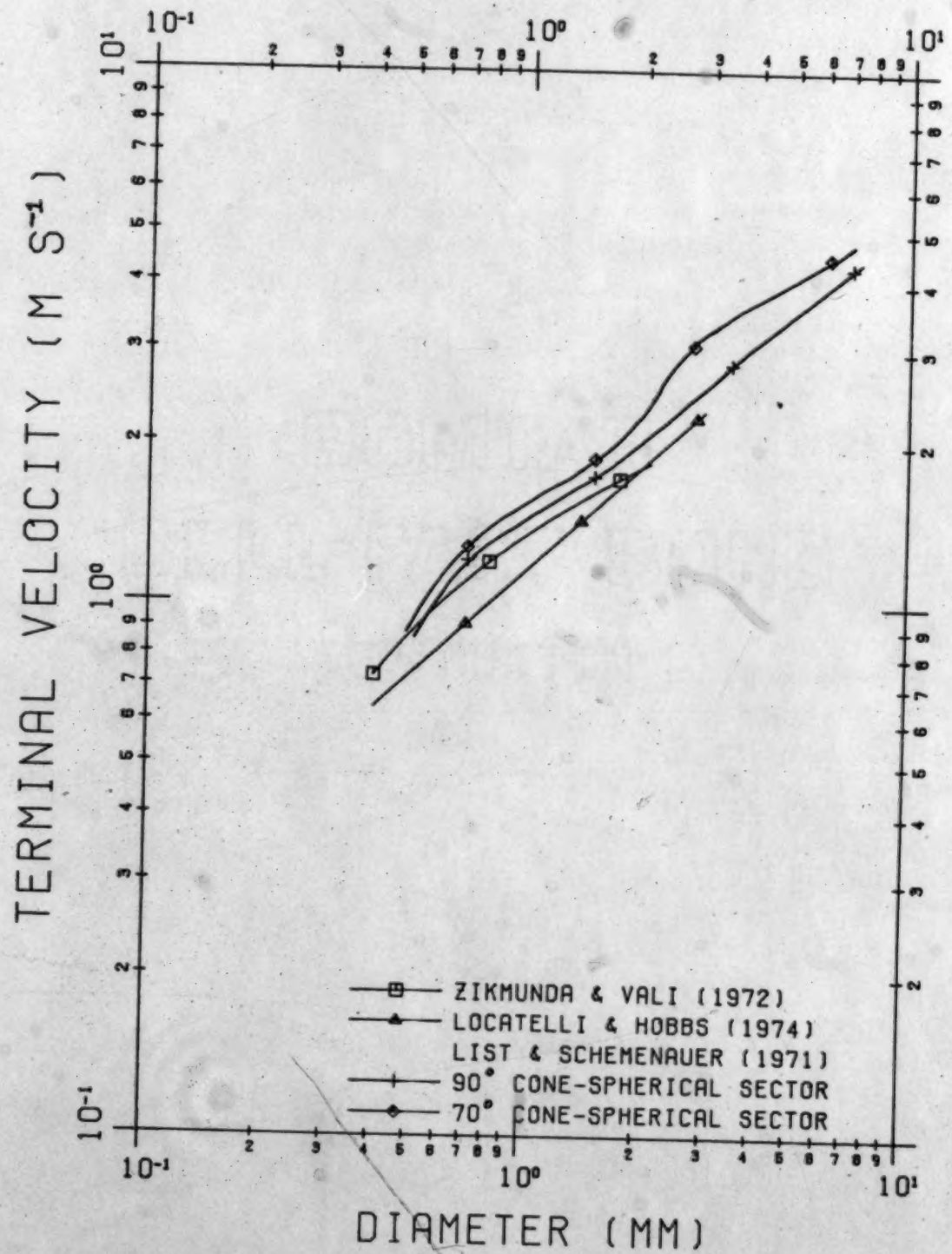

Figure 9. The terminal velocity of conical graupel as a function of graupel base diameter.

Figs. 8 and 9. In Fig. 9, the velocities for the sectors are those obtained with the models falling in a base-down orientation.

Locatelli and Hobbs (1974) have used an instrument which measures the time interval required for a falling particle to pass two light beams to obtain the terminal velocities of various types of rimed ice crystals as well as aggregates of crystals and graupel. Their values are also given in Fig. 9.

Because the measurements of terminal velocity of the various investigators have been obtained at differing altitudes, an attempt has been made to adjust the values to a common altitude. For this purpose, the altitude of Edmonton (640 m) has been chosen. This corresponds to a standard pressure of 940 mb at -10°C (U.S. Standard Atmosphere). In reducing the values, the assumption has been made that the terminal velocities vary as the reciprocal of the square root of the atmospheric density. This assumption is strictly valid only when the drag coefficient does not vary with Reynolds number. While this condition is closely approximated for hailstones, some variation does occur for graupel and ice crystals. However, the error in terminal velocity resulting from the application of this assumption is likely to be no more than 10% for any given curve.

2.8 A Summary of the Simulation Conditions.

Because no thorough and complete microphysical investigation of the conditions occurring in a graupel producing cloud has been completed to the present time, our knowledge of these conditions is incomplete. As a result, in order to provide as accurate a simulation as possible, the observations and measurements of various investigators have been combined, even though this does not provide as accurate a set of conditions as one or more complete sets would have.

Judging from the data presented above, the most probable temperature range for the most active growth of conical graupel is from −5 to −20°C. While some graupel has been collected between 0 and −5°C, it is not certain that it was not produced higher in the cloud. On the other hand, very few graupel are found above the −20°C isotherm. Cloud droplet water contents most commonly tend to fall within the range of 0.2 to 1.5 g m^{-3} in the regions of clouds which are expected to be suitable for graupel production. The cloud droplet distributions will commonly be bounded on the lower end by something similar to McLeod's 2743 m distribution (Fig. 5), and on the higher end by a distribution like the July 9 distribution of Christensen et al. (Fig. 6). This means that the mass median diameter will most probably lie between about 11 and 23 μm, with the shape of the distribution being similar to McLeod's 2743 m one (Fig. 5).

Based upon Pitter and Pruppacher's work, a

hexagonal plate of 500 μm to 1 mm in diameter should rime efficiently, and provide a suitable graupel growth substrate. The frequency of collection of such crystals by various authors tends to support this. The data of Figs. 8 and 9 lead to the conclusion that a 500 μm hexagonal plate ice crystal should sweep out cloud droplets while falling at a rate of about 25 cm s^{-1}. A 1 mm plate would begin falling at near 50 cm s^{-1} and as riming progressed, and the particle grew into a conical graupel 4 mm in diameter, the terminal velocity would rise to about 3 m s^{-1}.

The application of these conditions for the simulation of conical graupel growth is detailed in the following chapters.

CHAPTER III

THE EXPERIMENTAL APPARATUS

3.1 An Overview of the Equipment.

The conditions deemed to be necessary for the simulation of conical graupel growth, as described in the previous chapter, were achieved through the use of a cloud chamber located within a controlled temperature cold-room.

The free-fall of a hexagonal plate ice crystal was simulated within the cloud chamber through the motion of a hexagonal plate substrate which was attached to the end of a rotating boom. Provision was made for the stroboscopic illumination of the substrate upon each revolution of the boom, as well as the acquisition, at a preset interval, of a photograph of the riming upon the substrate. The substrate, along with its needle support, could be removed from the cloud chamber to facilitate its observation under a stereo microscope.

The cloud-like droplet distribution required for the simulation was produced externally to both the cloud chamber and the cold-room using a recently developed spraying system. It was introduced into the cloud chamber through a hose.

Detailed descriptions of this apparatus will be provided in the following sections of this chapter.

3.2 The Spraying System.

At the outset of this study it was discovered that none of the conventional, commercially available spray nozzles which the author investigated, would be suitable for the production of the droplet distribution required. Such sprayers produce enough large droplets to raise the mass median diameter beyond the desired range. While commercial ultrasonic nebulizers producing very fine mists are available, they suffer from two disadvantages. First, because of the principle of their operation, the mist produced is warmer than the air and water which is put into them. This is a distinct problem for the application intended in this study, since the temperature difference between the mist and the air already in the cloud chamber, should be minimized. The second disadvantage of these nebulizers is the relatively low cloud droplet water concentration which they produce. Spinning disk nebulizers have the attribute of producing a droplet size distribution with small dispersion, but this is at the expense of a fairly low cloud droplet water concentration.

A unique sprayer developed by R.S. Babington, and based upon a new engineering concept, has been described by Dresner (1973), and by Litt and Swift (1972). Conventional pneumatic spray nozzles forcefully break up the liquid by

using the total pressure of the driving gas to force a gas-liquid mixture through an orifice. Ultrasonic nebulizers rely upon rapidly vibrating transducers to break up the water. The Babington nebulizer utilizes the surface tension of the liquid to control the uniformity of a thin film of liquid formed on a ball. This film is broken up by the pressure of the gas to form a droplet distribution which has smaller dispersion than the spray produced by the techniques mentioned above.

The principle of operation of the Babington nebulizer is illustrated schematically in Fig. 10. The

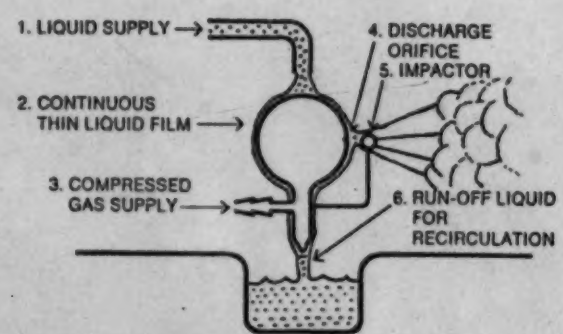

Figure 10. A schematic diagram outlining the principle of operation of the Babington nebulizer. (after Owens-Illinois, 1974)

liquid supply, in this case water, is directed (with a pressure head of at least 10 cm) at the top of a glass ball.

Because of surface tension, the water forms a thin film over the surface of the ball and runs off at the bottom, where it is collected for recirculation. A compressed gas supply, in this case air, is introduced into the glass sphere and exits at near sonic speeds via a small slit cut along the 'equator' of the sphere. This rush of compressed gas breaks up the thin liquid film flowing over the slot and results in a spray with small droplet size dispersion. The spray characteristics are determined by the gas pressure, the size and shape of the slot, and the thickness of the film flowing over the ball. This last characteristic is in turn influenced by the surface tension of the liquid, the size of the ball, and the flow rate of the fluid. The advantage of this method of fluid breakup over that used in conventional nozzles, is the direct breakup of the fluid into droplets without the conventional formation of a tulip or film-like cone. The tulip normally breaks into ligaments in turn shaking apart into droplets with a large size dispersion (Photos p. 102, Dresner, 1973). The result of the more direct breakup in the Babington system is a narrower droplet distribution.

Consultation with Mr. Babington led to the conclusion that a commercial nebulizer based upon this concept and intended for medical applications (Owens-Illinois, 1974), produced a mist with a mass median diameter of about 5 μm, which was too small for the requirements of this study. As a result, it was decided to construct a pair

of sprayers based upon this concept, whose characteristics were adjusted to achieve the desired cloud droplet mass median diameter.

The glass sphere was blown to a diameter of 1.5 cm using a section of 6 mm glass tubing. The most difficult portion of the construction was the cutting of a slot along the 'equator' of the sphere. Litt and Swift (1972) suggested using a 0.2 mm by 1.5 mm slot with an impactor located in front of the discharge orifice to produce a droplet distribution with a mass median diameter of about 4 μm. Using this as a guide, it was discovered that a slot could be cut in the glass of the sphere by employing a cutting tool constructed specifically for this purpose. Using a small machine lathe, a stock 9/16 inch diameter round bar of aluminum was machined into a 300 μm thick, 9 mm diameter disk on a 4 mm diameter shaft. This tool was then mounted in a chuck on the lathe, and rotated at the slowest attainable speed of 650 rpm. The glass sphere was mounted in a vise and was fed into the rim of the disk which was coated with a mixture of 400 grit industrial diamond dust and petroleum jelly. The rim of the aluminum disk became impregnated with the diamond dust, and it was able to cut a 0.45 mm wide, and 3.2 mm long slot within about five minutes. Plate 2 illustrates the operation of cutting the slot. The glass sphere and cutting disk are near the center of the picture.

The two sprayers, one of which is shown in

Plate 2. Cutting the slot in the glass sphere for the sprayer.

Plate 3, were basically similar to the schematic diagram of Fig. 10. Water entered from the top, generally at a pressure head of 30 to 40 cm, collected at the bottom of the box, and drained out at the lower left. Air at a pressure of 200 to 275 kPa (40 to 50 psi) entered from the left side and was directed into the glass sphere. The spray exited through a corrugated hose of 6.5 cm diameter at the right. The box itself was constructed from 1/4 inch (6.3 mm) Plexiglas, with the components being fastened together by a glue made up of Plexiglas shavings dissolved in chloroform. The illustrated sprayer did not make use of an impactor ball, although the other sprayer did utilize that component. The impactor ball was 4 mm in diameter, and was attached 1 mm away from, and directly in front of the slot, in a

Plate 3. The cloud droplet sprayer.

manner similar to that shown in Fig. 10.

The spraying system, most of which is displayed in Plate 4, consisted of two sprayers, along with water and air supply systems. The distilled water was supplied from a 23 l (5 gallon) container shown at the top of the picture. This water was routed through a Barnstead mixed-bed deionizing cartridge (shown at the lower center of the picture), capable of increasing the resistivity of the water to over 8 Megohm cm. It was then directed into the sprayers (located at the center of the picture). A simple water head measuring manometer was placed just to the left of the sprayers. The water was drained from the sprayer box to a 23 l container below the sprayers (at the lower right of the picture). The air supply was chilled prior to entry into

Plate 4. The spray production system.

the sprayers by routing it through a 16 cm diameter coil made of a 3 m length of standard 1/4 inch (6.3 mm) outside diameter copper tubing immersed in a 2 l container filled with an antifreeze and water solution. This container was located within the cold-room, and its contents were thus maintained at approximately the same temperature as the air within the cloud chamber. To minimize the heating of the air during its passage outside the cold-room, the air supply hose and sprayer exit hoses were insulated.

Because of the lack of insulation on the sprayer

box, it became necessary to determine the temperature difference between the air (and water droplets) entering the cloud chamber through the sprayer hoses, and the prechilled air already in the chamber. Using the heat transfer calculations outlined in Appendix A, it was found that if the water temperature was 21°C, and the temperature of the air in the sprayer box was 14°C (both being measured values), then a 10 μm diameter droplet produced by the sprayer would reach ambient air temperature before leaving the sprayer box. Further, assuming the cold-room to be at −10°C, then by the time the air had passed through the sprayer hoses and entered the cloud chamber, it was predicted that it would have cooled to a temperature of about −2°C. A measurement of the air entering at that point showed the numerical estimate to be quite accurate. The temperature differential thus created between the top and bottom of the cloud chamber was helpful in promoting mixing of the air as it entered the top of the chamber. This mixing in turn encouraged the formation of a horizontally homogeneous droplet distribution lower in the box. Because of the resulting stable air stratification, and the cooling effect of the cold chamber walls, the temperature of the air near the path of the substrate rose by at most 1.5°C during the period required to carry out any given experiment. Again using the techniques of Appendix A, and assuming a linear rate of change of temperature from the top of the chamber (−2°C) to its bottom (−10°C), it was found that even

the largest droplets (40 μm diameter) were reaching temperature equilibrium with the air as they descended at a velocity equal to their terminal velocity plus the 0.19 cm s^{-1} at which the air was flowing through the chamber.

A method which superficially might seem to be a better solution to this heat exchange problem involves placing the sprayers within the cold-room itself. However, problems of preventing the water from freezing in the supply lines and in the collection region at the bottom of the sprayer box, expecially at times when the sprayers are not operating, make this method less desirable than the one which was adopted.

3.3 The Hexagonal Plate Substrate and its Suspension.

As mentioned in the previous chapter, the hexagonal plate substrate used to simulate an ice crystal of the same shape, should ideally be between 500 μm and 1 mm diameter, and 33 to 45 μm thick. The difficulty of producing such a plate from metal using common machining techniques soon became apparent. As a result, a completely different technique was adopted utilizing a softer material.

Stock round rods of 1/4 inch diameter nylon and teflon were cut to lengths of about 1.5 cm and mounted in the jaws of a lathe chuck. The ends of these rods were then machined down to a cylinder of about 2 mm diameter and 3 mm length. The chuck was removed from the miniature machine

lathe and attached to the lathe's indexing attachment. This device allowed the rod to be rotated in up to 48 precise fractions of a full turn. The indexing attachment was mounted in the vise of a Leitz 1400 Base Sledge Microtome in the manner displayed in Plate 5. The microtome, utilizing a

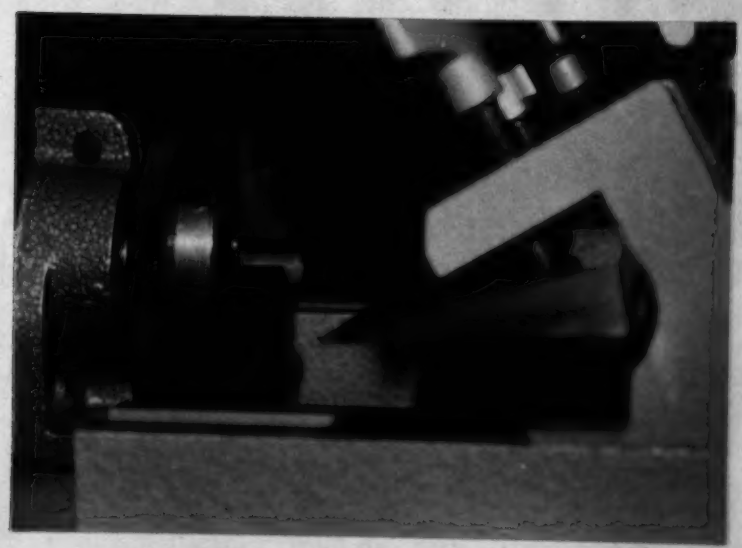

Plate 5. A view of the manner in which the microtome was used to produce the nylon hexagonal plates.

wedge-shaped blade, was then used to form a hexagonal column by slicing, at intervals of 60° of rotation, thin portions off the side of the cylinder which had been machined earlier. When the correct diameter column had been achieved, the indexing attachment was removed from the vise, and the hexagonal column was placed in the microtome vise in a position which would permit thin slices to be cut from the

column's end. After the nylon column's length had been reduced to about 1 mm by repeated slices, the column attained sufficient rigidity to allow the production of uniform hexagonal plates of 50 to 60 μm thickness. The teflon column remained too flexible, and resulted in plates with either non-uniform thickness, or a pronounced curl.

Two methods of plate suspension were attempted. The first involved the attachment (using epoxy glue) of the substrate in a coplanar fashion to the intersection of three 80 μm diameter wires which had been strung (at 120° to each other) from a metallic ring of 5 cm inside diameter. When this ring was propelled through a supercooled cloud of droplets, it soon became evident that the most pronounced riming occurred upon the thin supporting wires, followed by the corners of the plate, and the plate's edges. The least amount of rime accumulated at the center of the plate. Since the riming on the supports was very likely disturbing the rime which should have formed on the plate alone, this method of substrate suspension was discontinued. In its place, a sting type of support was devised. It involved the attachment (again using epoxy glue) of the substrate perpendicularly to the end of a needle, which was 5 cm long and 0.5 mm in diameter at its widest point, tapering to less than 0.2 mm at the point of attachment. Since the motion through the cloud of the substrate and the needle was such that the needle was trailing the substrate, and furthermore since the needle's diameter at the point of suspension was

less than one-fifth that of the plate, the influence of the needle upon the riming properties of the plate was minimal.

3.4 The Rotating Boom.

At the outset of this study, the intention was to carry out the graupel growth simulation within a wind tunnel into which the appropriate cloud droplet distribution and concentration was being sprayed. This technique has the advantages of a relative ease of velocity control and variation, and continuous observation of the growth of rime upon the substrate. The disadvantages of this technique include the difficulty in maintaining a turbulent-free flow field past the substrate, and in measuring the cloud droplet water content and size distribution. This latter problem is due to the need to determine the collection efficiency of the devices used to make such measurements. Unfortunately, a wind tunnel suitable, without modification, for the purposes of this study was not available. When the costs of producing a suitable tunnel were compared with the advantages which such a facility would have over the much simpler simulation system described below, the latter system was determined to be more appropriate.

Rather than have the substrate stationary and the air flowing past it as in a wind tunnel, the experiment was carried out in a cloud chamber where the air was essentially stationary, and the substrate was moved. This was accomplished by attaching the substrate suspension to the

end of a rotating boom. The scheme is illustrated in Plate 6. One of the first questions to be answered was the

Plate 6. The boom as seen near the bottom of the cloud chamber. The needle and substrate at the end of the boom are difficult to see.

degree of realism afforded by this technique. That is, what are the effects of the rotational motion upon the airflow about the substrate, and upon the substrate's riming properties?

Brownscombe and Hallett (1967) have carried out an experimental investigation of the process of riming. They determined that for small deformations of the impacting droplets, ie. where the resulting frozen cap has a height approximately equal to its radius, the time of deformation is

$$O(r_1/U_0) = 1.2\times10^{-6}\ s \qquad (3.1)$$

for a droplet radius r_1 equal to about 6 μm, and a plate velocity U_0 of 50 cm s^{-1}. If one assumes constant deceleration during this period, then the deceleration is $U_0^2/2r_1$. Now the centripetal acceleration due to the rotation of the boom is equal to U_0^2/r_b where r_b is the radius of the boom. Since the ratio of accelerations is

$$O(2r_1/r_b) = 4.0\times10^{-5} \qquad (3.2)$$

the rotational acceleration of the boom should not cause a significant additional deformation of the droplet during the riming. To minimize the effects of the boom upon riming on the plate, the needle support was positioned so that the substrate led the boom by about 3 cm. In addition, the angle between the needle and the boom was adjusted to position the substrate perpendicular to the flow.

The difference in flow velocity around the substrate is proportional to the difference in the distance from the boom's center of rotation to the opposite edges of the substrate. These two distances are 23.9 and 24.0 cm. The difference is thus approximately 0.4% of the average distance. The resulting change in the flow field should have only a very small effect upon the riming characteristics of the substrate. Therefore it is concluded that this system will provide a sufficiently accurate

dynamical simulation for the purposes of this study, although some problems still arise with this arrangement and are discussed in Chapter 5.

In order to minimize any variation in the rotation rate of the boom, a 36 cm (14 inch) diameter balance wheel with a moment of inertia equal to $3X10^{-2}$ kg m^2 was attached to the shaft joining the motor to the boom. The motor and this flywheel are shown at the center of Plate 7. A pair of

Plate 7. The equipment partition of the cloud chamber showing the motor, the balance wheel, and the camera trigger sensor and associated light source.

partitions were placed between the boom and the motor area to prevent the cloud-like atmosphere within the cloud chamber from producing riming in the motor area. The speed of the Dayton AC-DC motor was controlled through the use of

a Powerstat variable transformer. This provided motor speed variation over the range of 20 to 200 rpm, thereby allowing a variation in the velocity of the substrate from 50 cm s^{-1} to 5 m s^{-1}.

Since the substrate velocity during the experiments was always greater than or equal to 50 cm s^{-1}, and the terminal velocity of the largest droplets was less than 10% of that, the effect on the riming process of the droplets falling perpendicular to the direction of motion of the substrate was negligible. This conclusion is substantiated by the lack of evidence of the asymmetrical deposits that would have formed had this effect been significant.

No technique was found to measure the electrostatic charge build-up, if any, on the substrate due to the riming process. However, a build-up on the boom, which would have been even larger, was avoided by grounding this device. Two other effects which could have affected the experiments were oscillation of the substrate due to eddy shedding, and vibration of the boom during rotation. However, no special means were employed to counter these problems, since it did not appear that they were significant.

3.5 The Cloud Chamber.

The cloud chamber, shown in Plate 8, was designed

Plate 8. The cloud chamber and associated equipment.

so as to provide an enclosed volume capable of holding a cloud-like atmosphere through which a boom could rotate, resulting in riming on a substrate near the end of the boom. The side and back walls, as well as the ceiling, floor, and interior partitions of the chamber were constructed from plywood. The outside dimensions of the chamber were 183 cm (72 inches) high, and 76 cm (30 inches) square, excluding

the front shelf area. The lower 43 cm (17 inches) of the chamber was partitioned into two sections for housing equipment and providing an air exit. Plexiglas was used for the front wall to allow a clear view of the interior. Two accessory shelves were provided at the front to facilitate the placement of the photographic and other equipment described below. Ports with sliding Plexiglas doors were provided near the top and bottom of the right side wall, and near the bottom of the front wall. The lower ports were positioned to allow rapid access to the boom in order to adjust the substrate and needle, or to remove them for microscopic inspection. The spray reached the cloud chamber by passing through two 6.5 cm diameter corrugated hoses which led from the sprayers through a port in the cold-room wall, and up to two holes in the top of the cloud chamber. The cloud droplets settled downward in the chamber past the rotating boom, and through a partition located 14.5 cm below the boom. In this partition were drilled 22 equally spaced 3.2 cm (1.25 inch) diameter holes directly below the path of the substrate (see Plate 5). These holes provided an exit from the chamber for the air introduced through the sprayer hoses. Thirteen centimeters (5 inches) below this partition was another solid partition which prevented the remaining cloud droplets from reaching the bottom section of the chamber containing the motor and other equipment. The final exit of the spent air from the chamber was through two 10.8 cm (4.25 inch) diameter corrugated hoses at the lower

sides of the chamber. The interior of the cloud chamber was painted flat black in order to minimize glare and to improve the photographic contrast. The paint also protected the wood from the water content of the cloud-like atmosphere.

3.6 The Cold-room.

Two cold-rooms were used during the course of this study. The first, provided by the Mechanical Engineering Department, allowed for the commencement of the experiments during delays in the construction of a cold-room facility within the Meteorology Division. Both cold-rooms were used to provide a controlled temperature atmosphere within the range of 0 to -20°C.

3.7 The Photographic System.

At the outset of this study it was determined that the rotating boom method of providing the relative motion of the substrate past the cloud-like atmosphere would be suitable only if some means were found to illuminate the substrate for an instant at precisely the same point during each revolution of the boom. In addition, a facility for photographing, at preset intervals, the substrate and the growth of rime upon it was required. These objectives were met through the use of the following equipment.

The first requirement was the provision of a triggering signal to indicate that the boom had just passed a certain point during its rotation. This signal was

provided by a photo-electric sensor which responded to a light beam being reflected to it from a mirror placed on the underside of the balance wheel. This equipment is illustrated at the left center of Plate 7. The sensor and light source were mounted on a movable platform which is located near the left edge of that picture.

The photographs were taken with a Canon F-1 35 mm camera, driven by a Canon Motor Drive MF, and attached to a Pentax bellows unit and 100 mm f/4 macro lens. The bellows and lens system were extended to provide a two-to-one magnification of the subject, and the camera was positioned to photograph the substrate at an angle of 5° forward from the perpendicular to the substrate's trajectory. The lens extended through a hole in the Plexiglas front of the cloud chamber in order to prevent distortion of the image by the Plexiglas. The timer used to trigger the camera at preset intervals was the Canon Interval Timer L.

There was an approximate 80 ms delay between the reception of a signal by the camera, and the actual triggering of the shutter. While this time was constant, the distance travelled by the substrate during this period varied as the rate of rotation was varied. Thus the triggering source mentioned earlier had to be movable along a path directly below that of the mirror on the rim of the balance wheel so as to compensate for the various rates of rotation used, and to insure that the shutter was triggered and the flash fired just as the substrate came into the

field of view of the camera.

An electronic circuit was designed and constructed by the University of Alberta Department of Technical Services to provide the synchronization required between the triggering device, the strobe, the camera, and the interval timer. The design and operation of this device is described in Appendix B.

The flash employed to illuminate the subject was a General Radio Strobolume. It was used with its narrow beam and high power settings. The strobe was pointed directly at the substrate, and was located as shown in Plate 8. A housing was built to surround the front of the flash to prevent stray light from bouncing off the Plexiglas front wall and thus annoying the observer. The operation of the strobe created a small quantity of ozone which was ducted to the outside of the cold-room in order to prevent an accumulation of this gas within the cold-room. This ducting arrangement can also be seen in Plate 8.

3.8 Temperature Measurement.

The temperature of the air within the cloud chamber was measured using a Weather Measure Corporation thermistor thermometer. The instrument was placed on the lower front shelf of the cloud chamber, with the sensing device located at one of the holes in the upper partition, about 14.5 cm below the path of the substrate.

3.9 The Measurement of the Cloud Droplet Size Distribution.

A distinct advantage of the technique of moving the substrate through the relatively stationary cloud-like atmosphere (rather than the converse technique used in a wind tunnel) was the relative ease with which the cloud droplet water content and size distribution could be determined. When sensors used to measure these quantities are moving relative to the air, as would be the case in a wind tunnel, the collision efficiency of the sensor must be determined in order to make corrections to the observed concentrations and size distribution. In this study such corrections were unnecessary.

Various techniques for the measurement of the cloud droplet size distribution were attempted. The first involved the coating of microscope slides with a thin layer of Formvar plastic (Schaefer, 1964; Strong, 1972) and proved to be difficult to use. A liability of this technique was the rapid rate of evaporation of the chloroform or 1,2-dichloroethane solvents which were used to liquify the Formvar prior to sampling. This evaporation, together with the slightly cooler temperature of the cold-room relative to the cloud chamber, promoted the condensation of water vapor on the Formvar surface when the slide was placed in the supersaturated environment of the cloud chamber. The resulting 'blushing' of the Formvar surface made observation of the cloud droplet impact craters difficult.

A second technique, making use of a thin coating

of magnesium oxide powder on the slides, also proved to be unsatisfactory. There arose a difficulty in applying a sufficiently uniform coating on the slides to ensure a consistent calibration between the crater diameter and the diameter of the droplet which produced it.

A third method, which was used as the standard against which the other techniques were calibrated, involved the coating of microscope slides with a thin layer of Omala 85 oil. This technique had the advantage of maintaining the droplets which had become immersed in the oil in their spherical shape, so that the diameter of the droplets did not change as they impacted. The technique's disadvantages included the relatively rapid evaporation of the droplets (complete disappearance, in some cases, after as little as one minute under a microscope for droplets of about 7 μm diameter), the resulting lack of permanence of the measurement, and the possibility of droplet coalescence within the oil. The droplet distributions as seen on the slides were obtained through analysis of prints obtained by photographing the slides using transmitted light through a standard microscope.

The technique finally adopted for the droplet distribution measurement was the coating of the microscope slide with a thin film of household gelatin. The method, as outlined by Jiusto (personal communication), involves mixing a 15% solution (by weight) of gelatin in water, applying this to the slides using a glass rod, and then waiting at

least a few minutes for the coating to dry before using the slides. However, a variation of this technique was adopted in order to increase the efficiency of the rate of slide production, and to virtually eliminate the air bubbles introduced during application of the coating by Jiusto's technique. The gelatin solution and the slides were kept at a temperature of about 75°C in order to slow the rate of solidification of the solution. The solution was applied using a 1 cc capacity hypodermic syringe. It was determined that after solidification of the gelatin, the slides could be stored at least one or two months provided that they were kept in an environment free of liquid water. Upon use, the coating in the immediate vicinity of the impact of a cloud droplet was temporarily liquified by the water, resulting in the creation of a crater with a diameter related to the diameter of the impacting droplet. The relationship between these diameters will be discussed in the next chapter. Following the exposure of these slides to the cloud-like atmosphere in the cloud chamber (the exposure technique is described in Chapter 4), they were photographed using the Department of Botany's Zeiss Photomicroscope II with facility for Nomarski interference contrast (reflected light) illumination. The merits of this technique for illuminating the craters in the gelatin coating were stated by Garland (1971).

Examples of the photographs obtained using an oil-coated slide with transmitted light, and a gelatin-coated

slide with the Nomarski lighting technique are given in Plates 9 and 10.

The cloud droplet water content of the cloud chamber atmosphere was determined in two ways. First, the slides employed for determining the droplet size distribution were used directly to estimate the concentration of droplets in the air directly above the slide, through the use of the sum of the terminal velocities of the droplets plus the velocity of the air passing through the cloud chamber. Secondly, assuming the droplet distribution to be constant, a measurement of the mass of water which had impacted upon a known area of the non-coated slides in a given time was employed in determining the water content. These techniques will be elaborated upon in the next chapter.

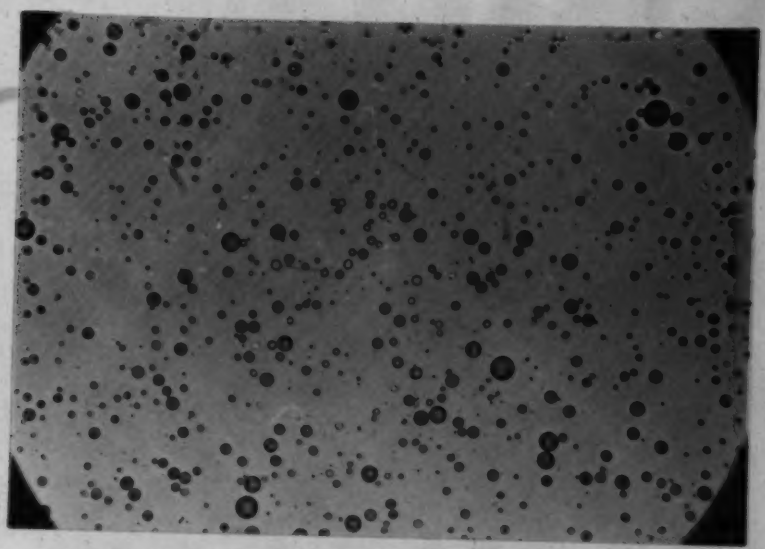

Plate 9. Microscopic photograph of an oil-coated slide obtained with transmitted light showing the droplet diameters. The enlargement is 225X.

Plate 10. Microscopic photograph of a gelatin-coated slide obtained with Normarski interference reflected lighting showing the droplet crater diameters. The enlargement is 130X.

CHAPTER IV

THE TECHNIQUES EMPLOYED IN DATA ANALYSIS

4.1 The Calibration of Gelatin-Coated Slides.

In order to determine a calibration factor for converting the cloud droplet crater diameters on the gelatin-coated slides to the diameters of the droplets themselves, the oil-coated and gelatin-coated slides were exposed side by side, for the same period of time, to the cloud in the chamber. The method of exposure consisted of placing the slides in a horizontal position on a wire holder which held them 5 cm above the upper partition of the cloud chamber (about 10 cm directly below the path of the substrate). In all cases, the sprayers were started at least five minutes before the slides were exposed, to allow a steady state in the droplet characteristics to be reached within the cloud chamber. The oil-coated slides were removed from the cloud chamber and photographed through the microscope as quickly as possible to minimize the droplet evaporation within the oil coating.

The crater and droplet size distributions for the gelatin and oil-coated slides respectively, were determined by tabulating the size distribution of the images measured on a 16 by 24 cm photographic enlargement, and then

correcting for the magnification factor. The diameters of the droplet or crater images were measured visually using a ruler.

The slide exposures for two calibration test series (denoted Cal. I and Cal. II) were carried out within a few minutes of each other at a temperature of -6°C. In both series the oil and gelatin-coated slides were exposed for 120 s. For Cal. IA, the oiled slide was enlarged to 450 diameters in the photograph. For Cal. IB, the gelatin slide was photographed using transmitted light and enlarged to 265X. For Cal. IC, the same slide was photographed using the Nomarski interference contrast technique and enlarged to 450X. In the second series, Cal. IIA′ was prepared for analysis in the same way as Cal. IA. Cal. IIA used the same sampling slide as IIA′, but was enlarged only 265X. Cal. IIB and Cal. IIC were treated in the same manner as Cal. IB and Cal. IC, respectively. Tables 6 through 13 of Appendix C summarize the results of these analyses. Graphs of the percentage of the droplets smaller than or equal to a particular size interval as a function of the maximum diameter for that interval, are given in Figs. 11 and 12. Fig. 11 shows that the magnification-corrected median diameter of th is greater for the direct transmitted light technique (IB) than for the Nomarski technique (IC) (14.3 μm as opposed to 11.1 μm), but that both are greater than that for the oil-coated slide (IA) (6.9 μm). Fig. 12 shows the same result to be true for the second series. It is

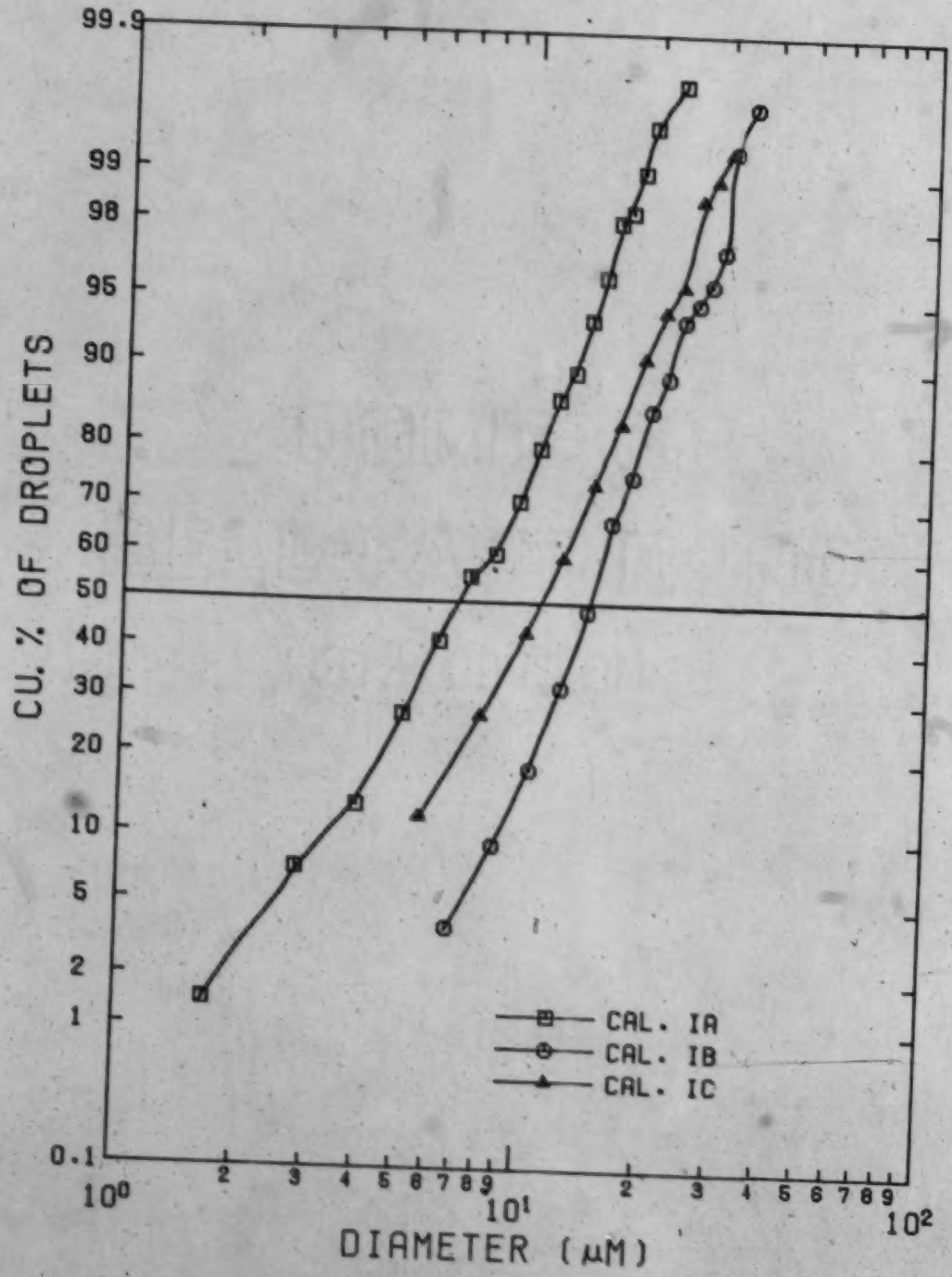

Figure 11. The cumulative percentage of droplet number as a function of droplet diameter for the calibration runs of Case I. The median diameters of the distribution are 6.9, 14.3, and 11.1 μm for IA, IB, and IC respectively.

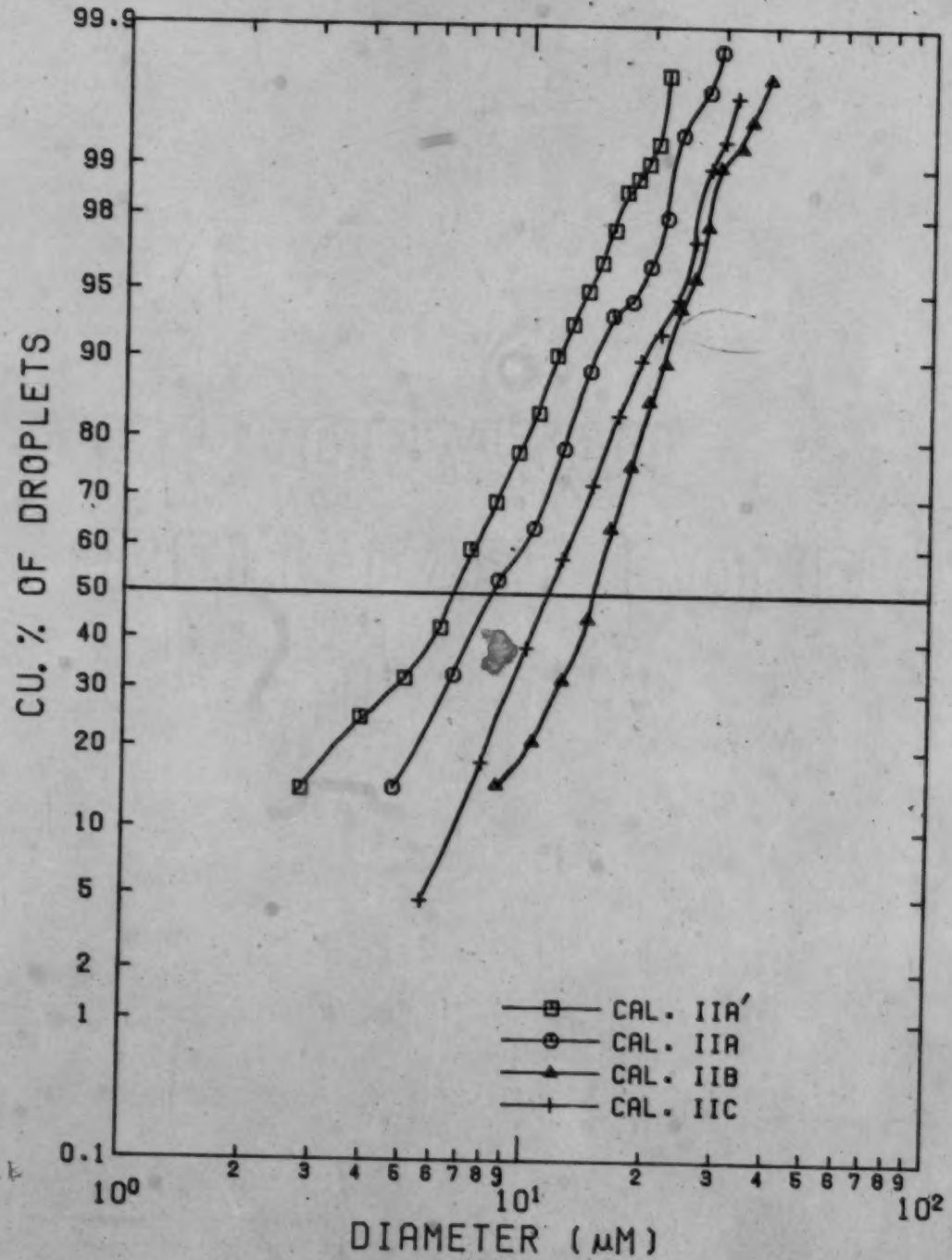

Figure 12. As in Fig. 11 except for the calibration runs of Case II. The median diameters of the distributions are 6.6, 8.3, 14.8, and 11.5 μm for IIA′, IIA, IIB, IIC respectively.

believed that the differences in the crater distributions for the two lighting techniques (series B and C) are due primarily to the different enlargement factor used for the photographic prints. The importance of choosing a magnification sufficiently large to allow accurate measurement of the crater or droplet images on the photographs is emphasized by the difference in median diameter between cases IIA′ and IIA (6.6 and 8.3 μm median diameter for 450X and 265X enlargement, respectively). Assuming that the droplets within the oil coating did not diminish in size significantly before being photographed, Fig. 11 implies the calibration factor for the gelatin slide craters is given by the median diameter for Cal. IC divided by that for Cal. IA, which equals 1.61. The corresponding calibration factor for Cal. IIC and Cal. IIA′ is 1.74. Taking the mean of these gives 1.68±0.07, an uncertainty of 4%. Since the size distribution curves are essentially parallel, this calibration factor has been assumed to be independent of size. This is the factor used on subsequent measurements of crater distributions to obtain the corresponding droplet distributions.

Upon completion of the experiments, one further calibration test was run. In this case oil and gelatin-coated slides were again exposed side by side within the cloud chamber for the same period. This time the oil-coated slide was photographed repeatedly through the microscope to determine the rate of droplet evaporation. Analysis of this

series of photographs showed the rate of evaporation to be much slower than for previous occasions, perhaps because of the pre-exposure of the oil-coated slide to cloud droplets (previously collected droplets were allowed to evaporate completely before re-exposure of the slide). Furthermore, the droplet distributions, given in Tables 13 and 14 of Appendix C, and shown in Fig. 13, have mass median diameters of 7.1 and 14.1 μm respectively, resulting in a calibration factor of 1.99. This value is considerably greater than the one used in this study, and thus throws doubt upon the assumed accuracy of the value employed. Further comparison between these techniques is given in the next section, and lends support to the recommendation of replacement of the gelatin-coated slides by oil-coated ones for the purpose of determining both the cloud droplet distribution and water content.

4.2 The Determination of Cloud Droplet Water Concentration.

The cloud droplet water concentration of the cloud chamber atmosphere was determined in two ways. The first technique began by calculating the droplet diameters corresponding to crater image diameters on a photographic print as described in the previous section. Next, the terminal velocity of these drops was calculated using Stokes' Law, which is accurate to within about 2% for water droplets with a diameter less than 40 μm. Using the area A of the slide corresponding to the area of analysis on the

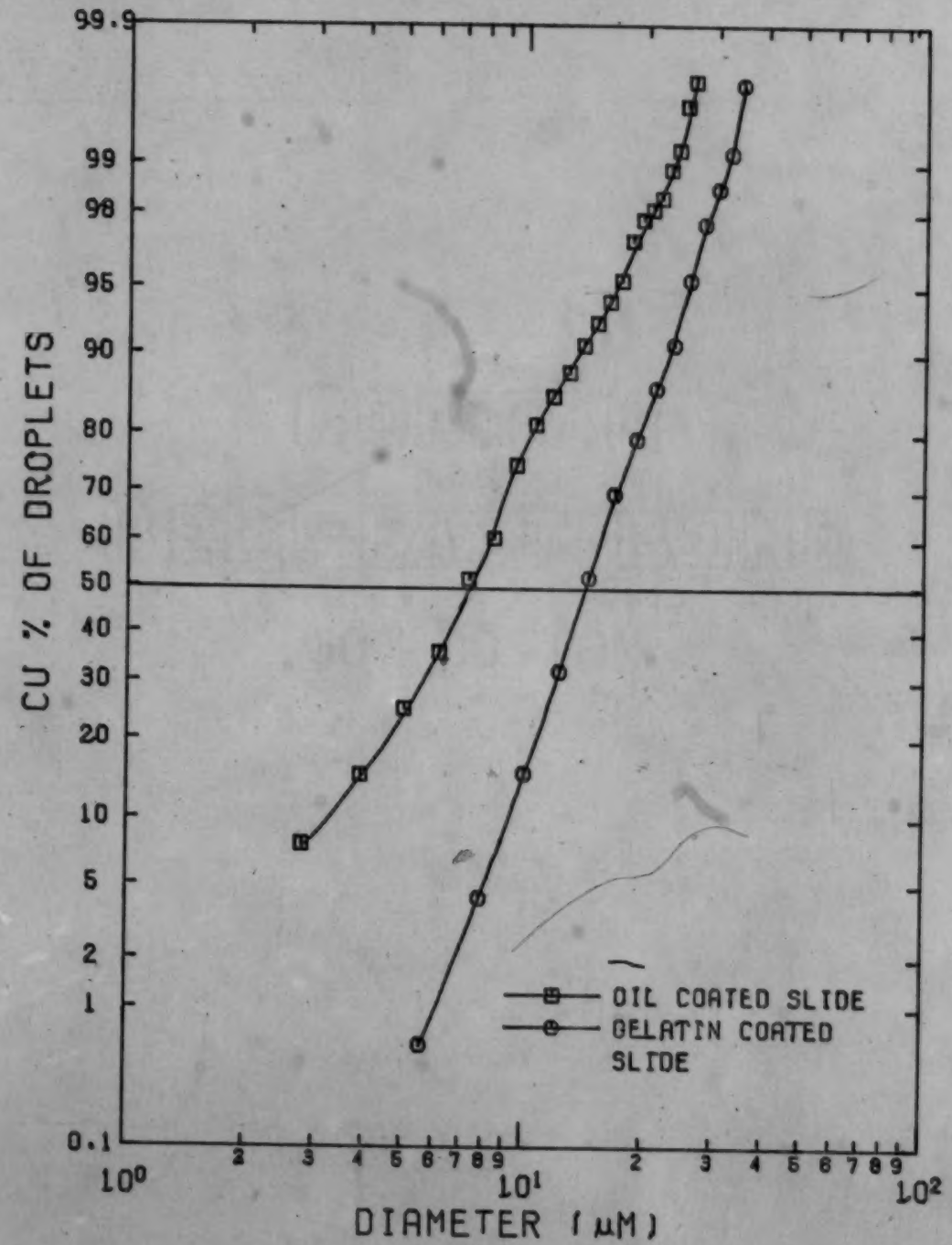

Figure 13. As in Fig. 11, except for the calibration run of Case III. The median diameters of the distributions are 7.1 and 14.1 μm for IIIA and IIIB respectively.

associated photographic print, the slide exposure time t_e, the water density ρ_w, and the number of droplets N_o in a given size category with mean diameter D, the droplet water concentration in the air above the slide was determined to be

$$L_c = \frac{\pi}{6} \frac{\rho_w N_o}{AVt_e} D^3 \qquad (4.1)$$

where V is the sum of the droplet terminal velocity and the mean air velocity within the cloud chamber. This latter velocity was estimated at 0.19 cm s^{-1} by measurement of the rate of flow of air through the sprayer hoses. A basic assumption involved in this calculation is that the cloud is homogeneous. Multiplying the droplet number concentration in that interval by the corresponding mean droplet mass gave the droplet mass concentration for the interval. This in turn was used to determine the mass median diameter of the distribution.

There exists a potential inaccuracy in both the size distribution and cloud droplet concentration determined in this way. Stochastic fluctuations in the number of droplets impacting upon the slide may be important for those size intervals in which only a few droplets are observed. Such fluctuations in the observed numbers of the largest droplets could under some circumstances lead to an erroneous estimate of the droplet mass concentrations. However, because the present droplet mass distribution appears to taper off at the largest droplet diameters, it is expected

that these stochastic fluctuations would not drastically alter the the distributions displayed in Chapter 5.

The second technique used in determining the cloud droplet water concentration was based upon a measurement of the mass M_m of the droplets which were collected in a time t_m on an uncoated slide which was exposed in the same manner as the slides for the first technique. Assuming that the cloud droplet size distribution was constant between the time that it was measured by the first technique, and the time at which the mass of the impacting droplets was measured, then the cloud droplet water concentration could be estimated as

$$L_m = \frac{M_m t_c}{M_c t_m} L_c \qquad (4.2)$$

where M_c is the mass of the droplets impacting on the coated slides in a time t_c, as estimated from the distribution obtained from the first technique. These values are given in Tables 15 through 21 of Appendix C.

Both methods are employed in determining cloud droplet concentrations in Chapter 5.

The calibration test performed on the oil-coated and gelatin-coated slides, mentioned in the last section, also allowed for an independent determination of the accuracy of the two methods for determining the cloud droplet water content. As mentioned earlier, the oil and gelatin-coated slides were exposed simultaneously, and photographed in much the same manner as for earlier

calibrations. In this case, however, the mass of the deposit on the gelatin slide was also determined. Tables 15 and 16 of Appendix C show that the mass on the slides was predicted by the droplet distribution technique to be 3.2 mg for the oil-coated slide, and 0.91 mg for the gelatin-coated one. Since the actual deposit was 3.1 mg, the gelatin-coated estimate is seen to be greatly in error, while the other one is quite accurate. As a result, the droplet distribution water contents derived from gelatin-coated slides in Chapter 5 are of dubious value. Since the size distribution does not appear to be greatly in error (after adjustment by the calibration factor), at least not enough to explain the discrepancy noted in Chapter 5, it is believed that the error must lie in the inability of the gelatin coating to faithfully produce craters for each impacting droplet. This inability might be due to the low velocity with which the droplets impact in this case, since it has not been noted by other authors using this method of determing droplet distributions at higher impact velocities (Jiusto, personal communication; Garland, 1971; McLeod, 1976).

4.3 The Determination of the Cloud Droplet Size Distribution

The droplet mass concentration (for each of the droplet size intervals) obtained using the technique described in the previous section, was employed to determine the percentage of the total mass of the droplets in sizes

smaller than or equal to a given size interval, as a function of the maximum diameter of that interval. The results of this analysis are described in Chapter 5.

4.4 The Effects of Sublimation Upon the Determination of the Cloud Droplet Water Concentration.

The accuracy of the second technique described in Section 4.2 for obtaining the cloud droplet water concentration (that is by measuring the total mass of the droplets accreting upon a slide exposed to the cloud chamber atmosphere), is influenced by the effect of sublimation upon the slide. In order to estimate the magnitude of this influence, the following analysis was carried out.

Pletcher (1969, p.267) and Mason (1971, p.274) give the rate of change of the mass of sublimated ice upon a surface as

$$\frac{dM}{dt} = 4\pi C G' S \qquad (4.3)$$

where S is the supersaturation relative to a plane ice surface, C is the 'electrostatic capacity' for the shape of the surface upon which the sublimation occurs, and

$$G' = \left[\frac{L_s}{KT}\left(\frac{L_s M_w}{RT} - 1\right) + \frac{RT}{DMP_s(T)}\right]^{-1}. \qquad (4.4)$$

In this expresion, L_s is the latent heat of sublimation, K is the thermal conductivity of air, T is the Kelvin temperature, R the universal gas constant, $P_s(T)$ is the saturation vapor pressure over a plane ice surface, D is

the coefficient of diffusivity of water vapor in air, M_w is the molecular weight of water, and $P_w(T)$ is the vapor pressure of the air with respect to water. The value of G'_s as a function of temperature, is given by Fletcher (1969, p.268). It is assumed that the air in the chamber is saturated with respect to a plane surface of water. Also if the slide (which is 25 by 75 by 1 mm in size) is approximated by a circular disk of equivalent area, then the 'electrostatic capacity' is given by

$$C = \frac{D_s}{\pi} \tag{4.5}$$

where D_s is the diameter of the disk. Thus the mass, ΔM, of the sublimating ice on the slide after a slide exposure of t seconds, will be

$$\Delta M = 4 D_s G'_s t \tag{4.6}$$

Using this result, calculations show that the mass of the sublimation on a typical slide will be no greater than 5% of the mass accumulated through the accretion of droplets.

4.5 The Effects of Sublimation Upon the Hexagonal Plate Substrate.

Using the method of analysis outlined in the preceding section, it was determined that the mass of the sublimation on the substrate would account for no more than about 5% of the mass of the accreted droplets. This holds true even if the boom is not rotating, and the substrate is

accreting only because of the terminal velocity of the droplets themselves and the low speed movement of the air about the stationary substrate.

4.6 Determination of the Rate of Accretion on the Substrate.

Two parameters would normally be involved in determining the rate of accretion on the substrate: the time, and the volume or mass. Since the sequential photographic record of the substrate during accretion provided only one view of the growth, the volume of this growth could not be determined accurately from these photographs. As a result, the two parameters used to indicate the growth rate were the maximum length of the accreted material in the direction of motion, and the time at which the photographs were taken.

The maximum length was determined through the analysis of the negatives obtained with the motor driven camera, by projecting them onto the glass screen of a Recordak C-1 35 mm Film Reader. This viewer's magnification of about 12X (together with a 2X magnification from the object to the negative), resulted in an image which was sufficiently large to enable the measurement of the length of the accreted material to an accuracy of ±0.1 mm.

The times at which photographs were taken were determined by noting the times of selected frames, and then by interpolating for the remaining frames. Because the intervalometer regulated the camera shutter release, these

times are estimated to be no more than 5 s in error for the longer intervals, and 2 s for the shorter ones.

4.7 Determination of the Density of the Growths.

The volume of the growths (upon reaching their maximum size) was estimated by photographing them first in the normal manner, and then again following a rotation through 90° about the needle axis. It was assumed that the shape of the growth could be approximated by a series of disks of elliptical cross-section arranged along the growth direction. Using an overlay for the Recordak's glass screen, the major and minor axes of these 0.1 mm thick disks were determined, and their volume calculated. The mass of the growths was obtained by detaching them from the substrate, and placing them in the sample pan of a Mettler H20 balance. This device was calibrated to provide an accuracy of ±0.1 mg.

CHAPTER V

THE RESULTS OF THE SIMULATIONS

5.1 The Onset and Early Stages of Accretion.

In order to determine the characteristics of the initial stages of accretion [1], the boom and substrate were rotated within the cloud chamber at a fixed air temperature and substrate velocity, over a brief period of time. The substrate and its sting support were then removed from the cloud chamber and photographed using a stereo microscope located within the cold-room.

Plates 11 and 12 show the front and side views, respectively, of the substrate-needle combination following a 5 min period of accretion at a mean air temperature of $-3.8^{o}C$. The riming for this and all other runs in the initial stage studies, was carried out with a substrate velocity of 50 cm s^{-1}. In all cases the temperatures are averaged over the period of the run. Plate 11 clearly shows the hexagonal shape of the plate, and Plate 12 illustrates

---

[1] The characteristics of the initial stages of accretion upon a hexagonal plate ice crystal were investigated by Cheng (1975) through the use of a numerical simulation procedure.

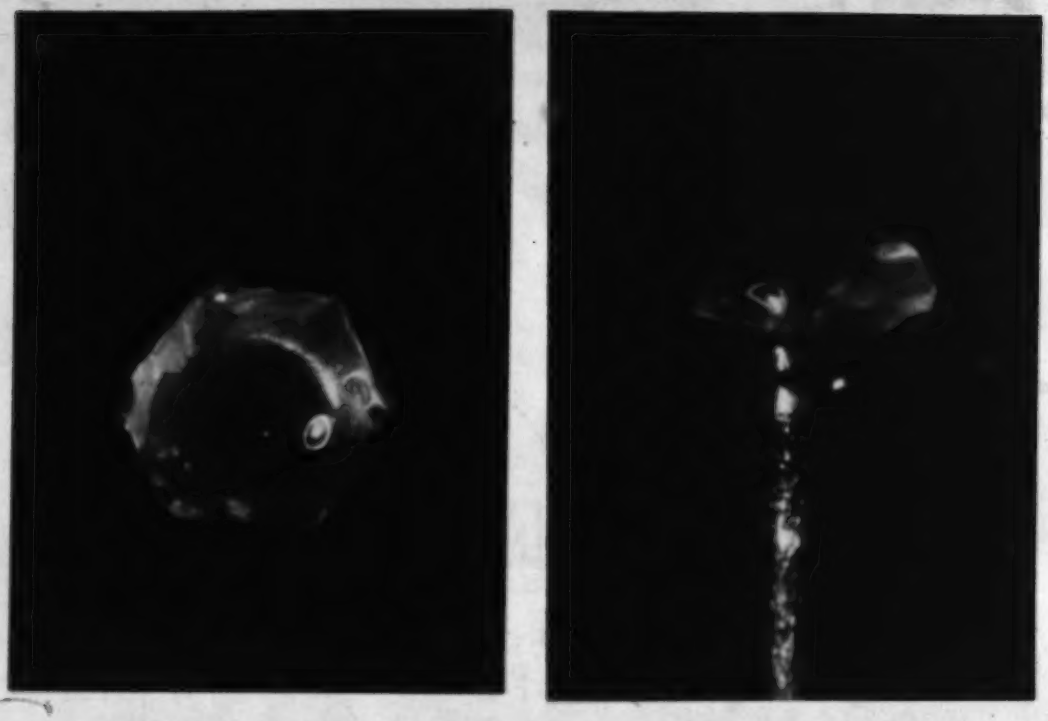

Plates 11 and 12. Two views of the initial stages of riming at a velocity of 50 cm s^{-1}, with an air temperature of -3.8°C, over a period of 5 min. The magnification factor for these and subsequent plates in this section is 40X. The side view is oriented vertically for the convenience of display, but the growth occurred in a horizontal orientation as in all other cases.

the size of the needle in relation to that of the plate, and the bell shape of the glue joining the two. The thickness of the plate can also be seen at the left edge of the growth, and two corners of the plate are visible at the left edge and the center. The smooth surface of the growth is indicated both by its outline, and by the nature of the reflection of the strobe light from the surface of the deposit. The growth shows evidence of being formed of transparent ice, suggesting that it formed at a deposit

temperature near 0°C. The quasi-hemispherical nature of the growth shape suggests that the droplets did not freeze immediately upon impact, and that the prime factor determining the shape of the growth was the water surface tension.

Plates 13 and 14 were taken following about 8 s of

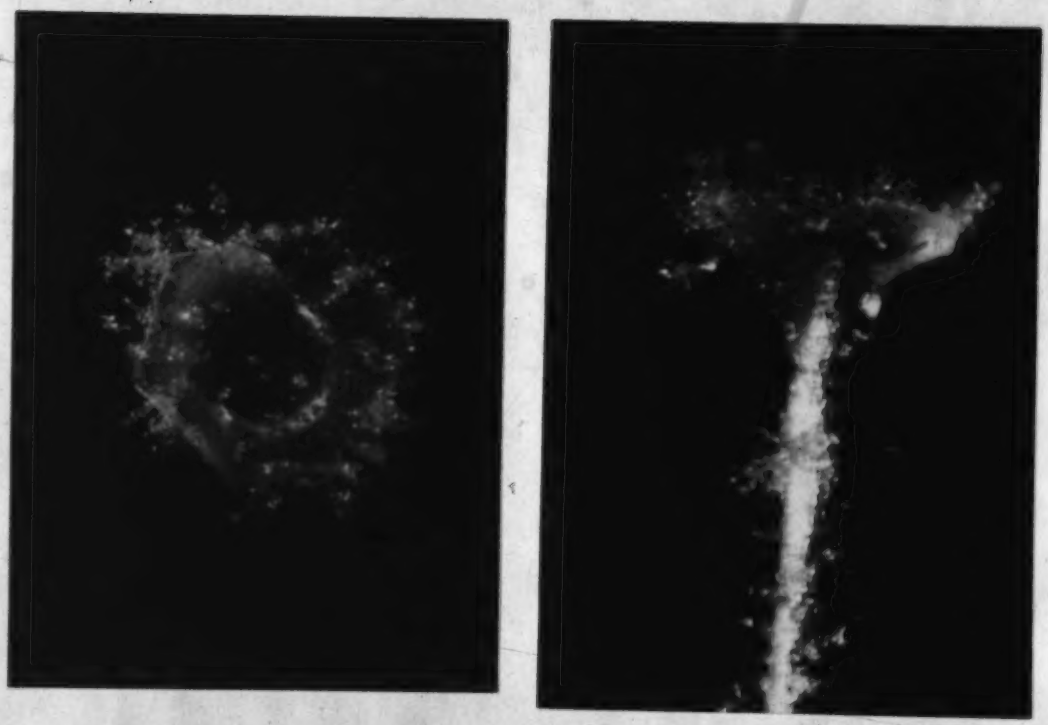

Plates 13 and 14. As in Plates 11 and 12 except with a mean temperature of −19.4°C and over period of 8 s. Because the stereo microscope has a very shallow depth of field at this magnification, parts of the growth are out-of-focus.

riming at a mean temperature of −19.4°C. Plate 13 clearly indicates that the most rapid rate of growth under these

conditions occurs along the edges of the hexagonal plate, with perhaps some evidence of preferential riming at the corners. Reflections from individual rimed droplets show that, within the limits of the accuracy with which the sizes of the droplets can be measured on the photograph, there does not appear to be a size sorting of the droplets as large as 2:1 with distance from the center of the substrate. An estimate of the size of these droplets as determined from the photograph, suggests that few are larger than 20 μm in diameter. Plate 14 shows the fragile nature of the growths at this time. Riming at points along the length of the needle is also evident.

Plates 15 and 16 show the results of 60 s of growth at an air temperature of -15.2°C. Plate 15 demonstrates that at this stage, riming along the edge of the substrate still predominates, but more rapid growth at two of the plate's corners can also be seen. Plate 16 shows that the rime has grown to a length of about 350 μm.

Following 4 min of growth at a mean temperature of -7°C, the substrate has accreted in the manner shown in Plates 17 and 18. This growth shows definite signs of the influence of the corners, with five of six corners appearing to have long slender growths originating near them. The orientation of the hexagonal plate in Plate 17 is visible near the top, where either riming has not occurred, or the growth has broken off. Plate 18, in particular, displays the individual nature of these growths. Some of them do not

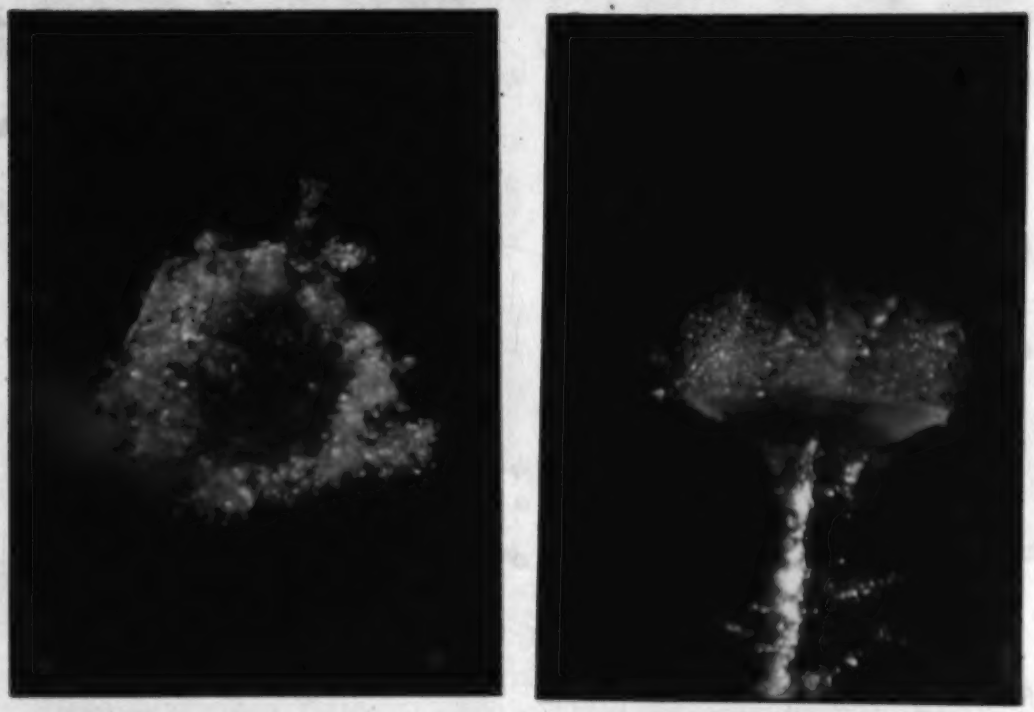

Plates 15 and 16. As in Plates 11 and 12 except with a mean temperature of −15.2°C, and over a period of 60 s.

appear to be attached to each other at any point along their length. A total of six major growths are visible in this photograph. The apparent bending of the substrate in this photograph is due to perspective distortion: one of the corners of the plate is positioned nearly midway between the left and right edges of the substrate.

On the basis of these and other runs made at various combinations of total accretion time and air temperature, Plates 19 through 22 have been chosen for comparison with Plates 15 and 16 as an example of the effects of the air temperature on the nature of riming. In

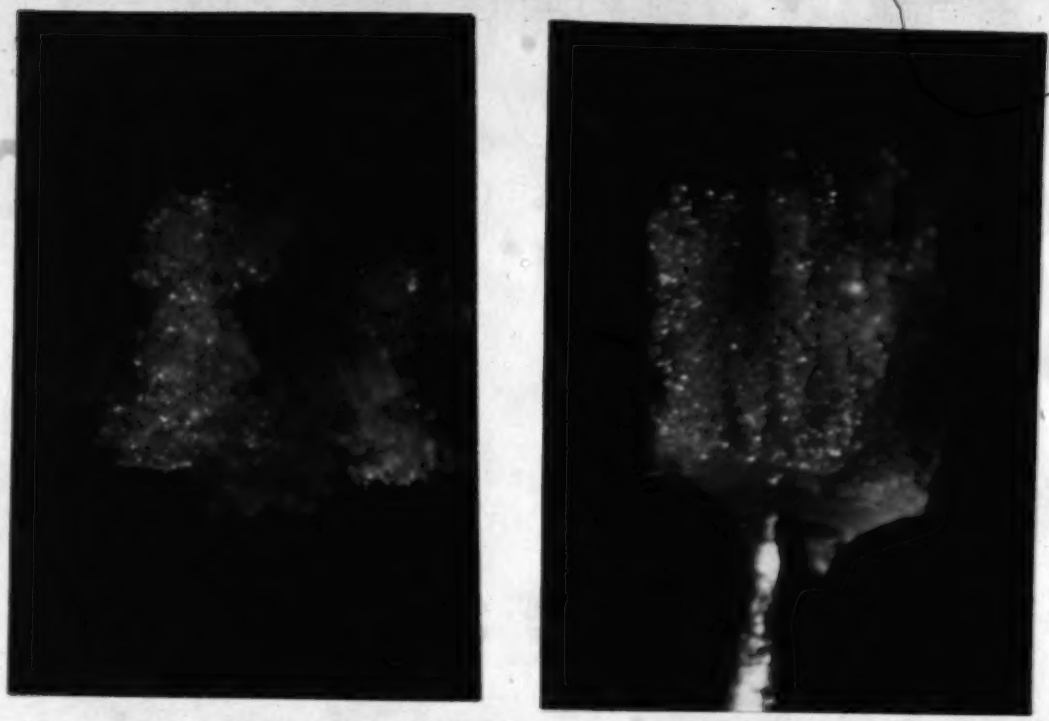

Plates 17 and 18. As in Plates 11 and 12 except with a mean temperature of −7°C, and over a period of 4 min.

all six of these photographs, the growth time was 60 s, but for Plates 19 and 20, and Plates 21 and 22, the temperatures averaged −9.5°C and −21.5°C respectively. This comparison leads to two apparent differences. First, the riming appears to become progressively less dense and more dendritic in nature as the air temperature is lowered. Second, the rate of growth (in length) of the deposit appears to increase as the temperature decreases, even though the cloud droplet water concentration in the chamber remains virtually constant.

An important feature of all of the above sequences

Plates 19 and 20. As in Plates 15 and 16 except with a mean temperature of −9.5°C.

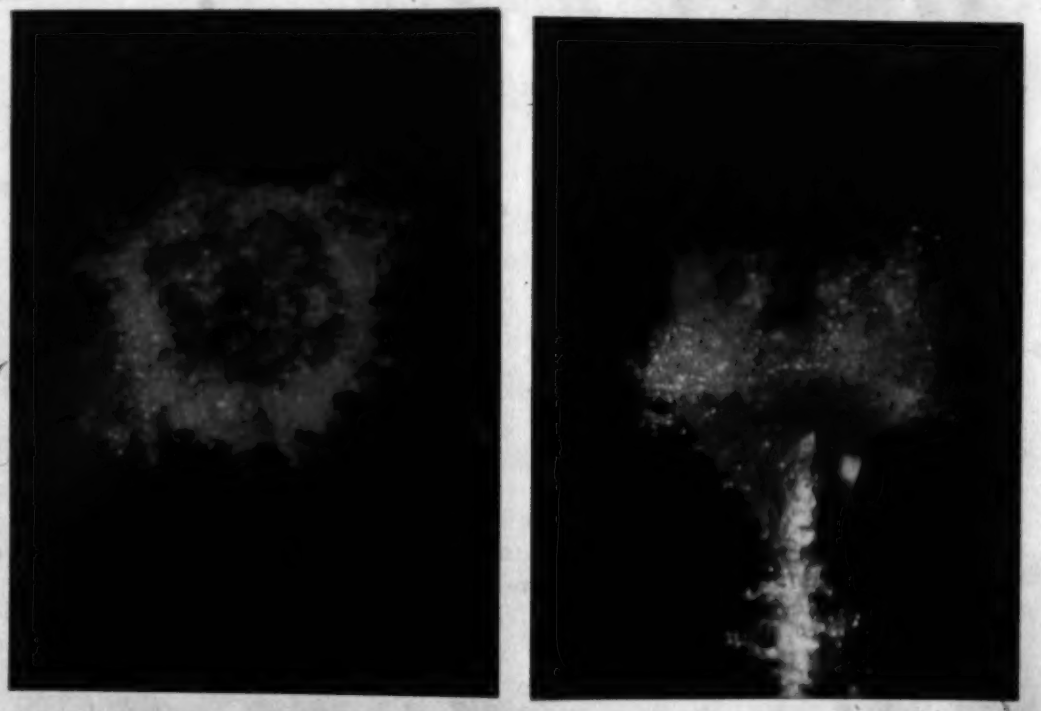

Plates 21 and 22. As in Plates 15 and 16 except with a mean temperature of −21.5°C.

is the tendency toward very little 'fanning out' of the growths. The angle at which they do fan out is certainly smaller than the 70 to 90° that is usually associated with conical graupel.

5.2 The Qualitative Analysis of Accretion for Prolonged Periods.

To study the accretion upon the substrate over longer periods of time, the Canon camera and G.R. Strobolume were used to photograph the riming process while it was taking place. Sequential pictures were thereby obtained which allowed the determination of the rate and nature of growth. The elapsed time for each frame is listed in the tables of Appendix D. [1]

The first of the sequential series of photographs is shown in Plate 23. The randomly distributed, dendritic, white marks prevalent on this sequence of photographs should be ignored. They have been caused by electrostatic discharges within the camera during rewinding of the film. In this sequence, the substrate was not moving, and the experiment was performed in order to determine the nature of riming when the only motion was the free-fall of the cloud droplets in combination with the slow downward motion of the air in the chamber. The mean air temperature was -5.4°C.

---

[1] Individual frames from such sequences will be referred to as Frame 23(1,3), for example, signifying the frame in the first row, and third column of Plate 23.

The photographs show that while the largest quantity of riming occurs on the upper portion of the substrate and the needle, as would be expected if the above assumption was correct, a significant amount of riming also occurs on the lower portions of the substrate and needle. The existence of this riming indicates that some small-scale turbulent motion was present in the air within the cloud chamber. It is believed that a greater amount of riming has occurred on the substrate than on the needle because of the higher collection efficiency at the edge of the plate. Frame 23(3,5) was taken at the same time as the one preceding it (which is displayed in an enlarged form in Plate 24). However in Frame 23(3,5), the needle has been rotated by about 90° to provide a different view of the growth.

Plates 25 and 26 show the accretion of cloud droplets upon the substrate at a mean temperature of -14.6°C and at a velocity of 50 cm s^{-1}. As shown in Chapter 2, this velocity is representative of the terminal velocity of a hexagonal plate ice crystal of comparable size. [1] Frame 25(2,2) taken 5.6 min after the beginning of riming, shows that there are several distinct growths on the substrate. By Frame 26(1,1) (taken at 15 min), this feature

[1] Because the substrate moves between 5 and 25 μm (depending upon its velocity) during the 10 μs period of the strobe flash, some blurring may be evident in some of these photographs.

Plate 23. A sequence of photographs taken at a mean air temperature of -5.4°C with no motion of the substrate. The elapsed time for each frame since the initiation of riming is tabulated in Appendix D, however the interval between frames is approximately one minute.

has been obscured by further growth. However, when the needle is rotated through about 90° to reveal another view of the growth as in Frame 26(2,2) (which is shown in

Plate 24. An enlarged form of Frame 23(3,4).

enlarged form in Plate 27), the existence of separate growths is again evident. The sudden increase in width of the rime between Frames 26(1,2) and 26(1,3) is thought to be due to a sudden weakening of one of the growths near its point of attachment, and a resulting pivoting downward of this growth about its attachment point. The potential causes of this event are discussed near the end of this section. Growth in this case is predominantly in the direction of motion (into the wind), in contrast to the growth in the sequence of Plate 23. It also appears to be

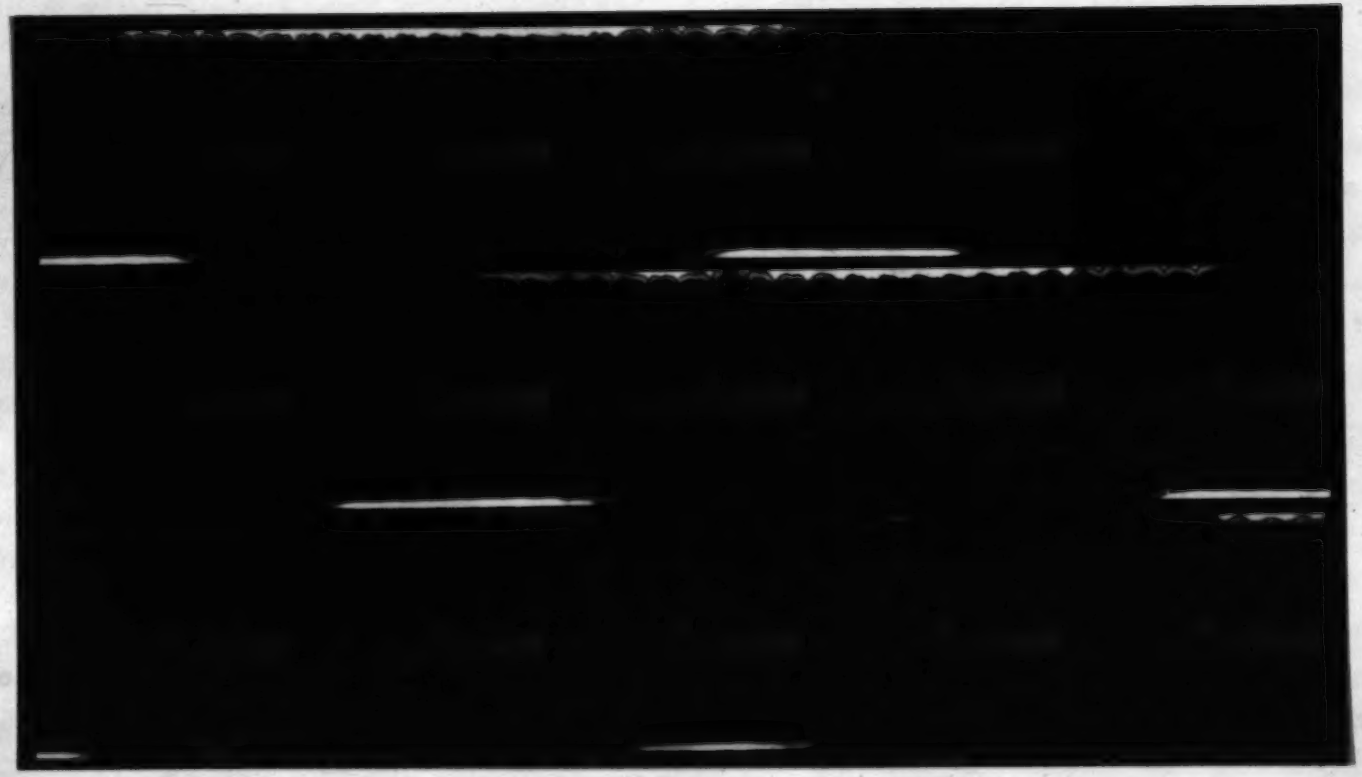

Plate 25. As in Plate 23 but with a mean temperature of -14.6°C and a substrate velocity of 50 cm s^{-1}. The time interval is again one minute.

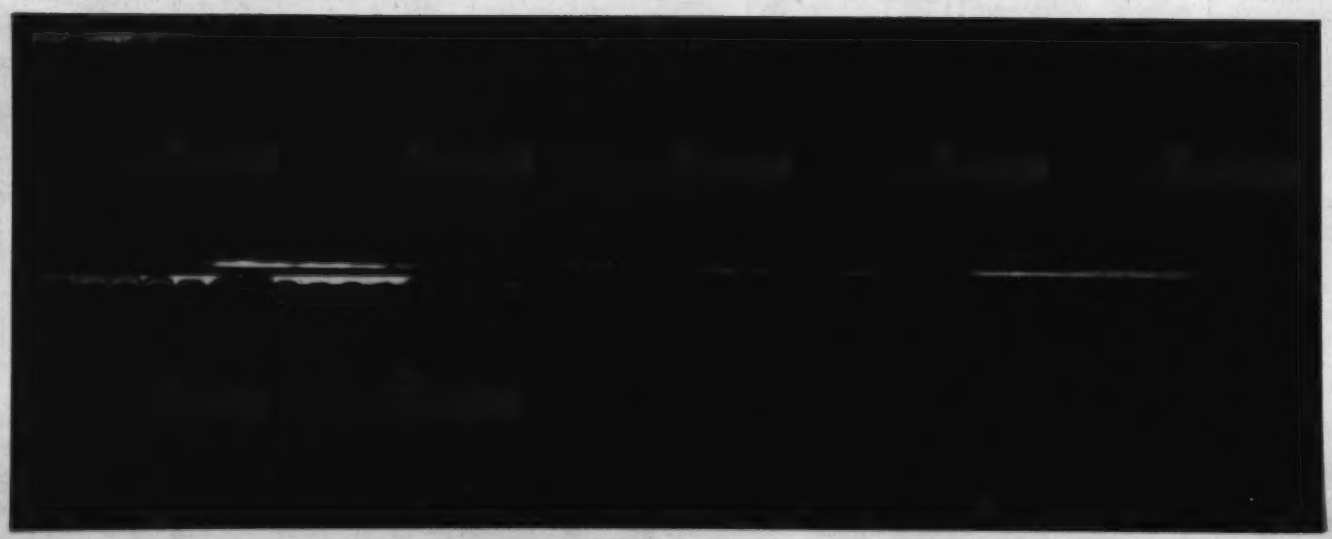

Plate 26. The continuation of Plate 25.

more compact and hence possibly of greater density than that of the previous sequence.

Plate 27. An enlarged version of Frame 26(2,2).

The next sequence, taken at a mean air temperature of −15.4°C and at a substrate velocity of 2.5 m s^{-1}, is displayed in Plate 28, with Frame 28(3,5) enlarged as Plate 29. This speed was chosen because it is typical of the terminal velocity of a conical graupel of about 5 mm base diameter. The most obvious departure of this sequence from previous ones is the much greater rate of growth in this case. Another important feature is the more compact nature of the growth. In fact, this growth is made up of a continuous curtain of rime which has formed around the

Plate 28. As in Plate 23, but with a mean temperature of −15.4°C and a substrate velocity of 2.5 m s^{-1}. The time interval is again one minute.

perimeter of the hexagonal plate. Although it is not evident in these photographs, visual inspection showed that the growth is in the form of a hollow cone with virtually no riming at the center of the hexagonal plate, or along the axis of the growth. A further notable feature most clearly visible in Plate 29, is the hexagonal symmetry of the deposit characterized by quasi-independent growths originating at the corners of the substrate. Although they are joined together to form a solid curtain, in contrast to previous sequences, these growths nevertheless can be distinguished from each other. Growths of considerable size can also be seen along the sides of the needle. The shape of the one nearest the substrate appears to have been influenced by the airflow around the growth on the substrate.

One feature of the deposits that may be noted by studying these sets of photographs is that the angle at which the growths fan out from the direction of motion decreases as the velocity of the substrate increases. This effect is likely due to a change in the flow field about the deposit as the velocity increases, resulting in a different angle of droplet approach and collision.

Plate 30 depicts a growth sequence where the hexagonal plate has been removed and the substrate is the end of the support needle. The mean temperature is $-18.2^{o}C$ and the velocity is 50 cm s^{-1}. This sequence of photographs illustrates that riming on the end of a needle does not

Plate 29. An enlarged form of Frame 28(3,5).

proceed very rapidly under these conditions. The growth that does occur does not appear to be strongly influenced by the direction of air motion. This is demonstrated by the two growths in Frame 30(3,2) which are oriented approximately perpendicular to the direction of motion.

Using the same needle substrate as in the previous sequence, but a mean temperature of −17.7°C and a substrate velocity of 2.5 m s^{-1}, the growth develops as shown in Plate 31 (with Frame 31(3,1) enlarged into Plate 32). The growth in this case appears to be more dense than in the last sequence, and it has a roughly conical shape, best seen in Plate 32. It is significant that in contrast to the previous sequence, the growth at the end of the needle is much larger than any of the growths along the sides of the

Plate 30. As in Plate 23 but with a needle rather than a hexagonal plate substrate. The mean air temperature is -18.2°C and the substrate velocity is 50 cm s^{-1}. The time interval is again one minute.

Plate 31. As in Plate 30 but with a mean temperature of -17.7°C and a velocity of 2.5 m s^{-1}. The time interval is 30 s.

needle. While the velocity in this case is a totally unrealistic simulation of the terminal velocity of a hexagonal plate of the same diameter as the end of the needle, this velocity is only about 25% greater than the terminal velocity of a conical graupel with the same base diameter as the maximum diameter of the deposit in this sequence. Interestingly, the resulting growth approximates the external features of a conical graupel more closely than those of earlier sequences.

An important event in this sequence occurs between Frames 31(3,2) and 31(3,3) when the growth breaks off the end of the needle and riming begins anew. This event is not unique. A growth along the length of the needle also broke off at a time subsequent to that of the last frame shown in Plate 31. The significance of both this event and the pivoting of deposits mentioned earlier, with regard to Knight and Knight's graupel formation theory, is difficult to ascertain. This is so because the forces acting upon the deposit are not identical to those that would act upon an ice crystal-graupel configuration similar to that in Fig. 2. In the latter case, the drag force and gravitational force are equal and act in opposite directions. Other forces potentially capable of breaking the deposits off the plate would occur if the plate wobbled during its fall. In the present simulation, however, while the drag force is acting in the normal fashion, the gravitational force is acting downward, ie. perpendicular to the direction of motion.

Their respective values in the case are about 0.8 and 0.6 dynes. In addition, a centripetal force is also acting perpendicular to the direction of motion with a magnitude of about 2 dynes. Thus the breaking off of the deposit from the substrate could be due more to the gravitational or centripetal forces rather than the aerodynamic drag force.

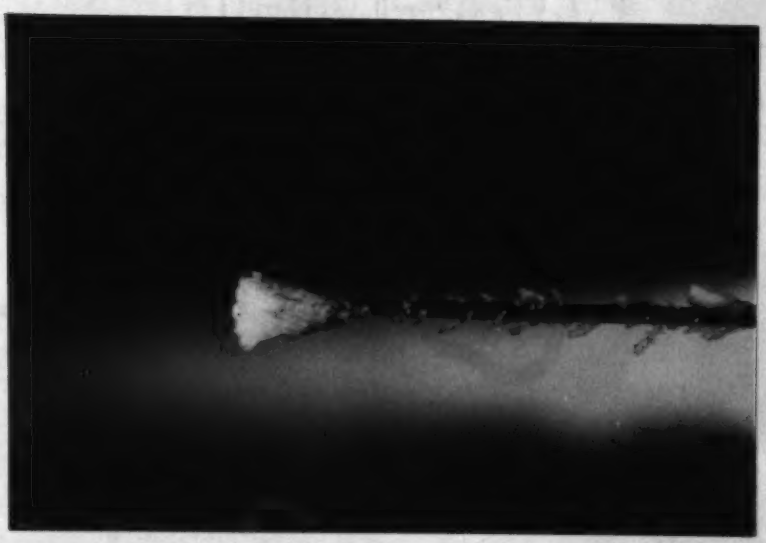

Plate 32. An enlarged form of Frame 31(3,1).

5.3 The Cloud Droplet Water Content and Size Distribution During the Prolonged Accretion Experiments.

In total 12 prolonged accretion experiments (referred to as SEQ. I to SEQ. XII) were performed. In order to make a quantitative analysis of the accretion process, it was necessary to determine the properties of the

atmosphere in the cloud chamber.

The cloud droplet size distribution was determined by the gelatin-coated slide technique described in Chapter 4. Because analysis of the slides to obtain the size distributions was time-consuming, samples were taken only during the experiments SEQ. II, SEQ. II′, SEQ. VI, SEQ. XI, and SEQ. XII. It was hoped that the sprayer output was sufficiently stable that the cloud parameters for the other experiments could be interpolated from these.

In order to test the effects of a variation of thickness of the gelatin slide coating upon the analyzed cloud droplet distribution and water content, two slides were used in the second sequence. These have been labelled as SEQ. II and SEQ. II′. While Slide 21 used in SEQ. II was made in the manner described in Chapter 3, Slide 19 of SEQ. II′ was coated with a 5% solution of gelatin in water. The parameters obtained from these slides are tabulated in Tables 17 and 18 of Appendix C, and the droplet mass distributions are plotted in Fig. 14. The difference in mass median diameter of 2.6 μm between these two distributions points out the need for rigidly controlled conditions while coating these slides.

The analyses of the remaining sampling slides are outlined in Tables 19 through 21 of Appendix C, and the size distributions are also plotted in Fig. 14. The mass median diameters for these last three slides are 8.2, 7.6 and 7.9 μm.

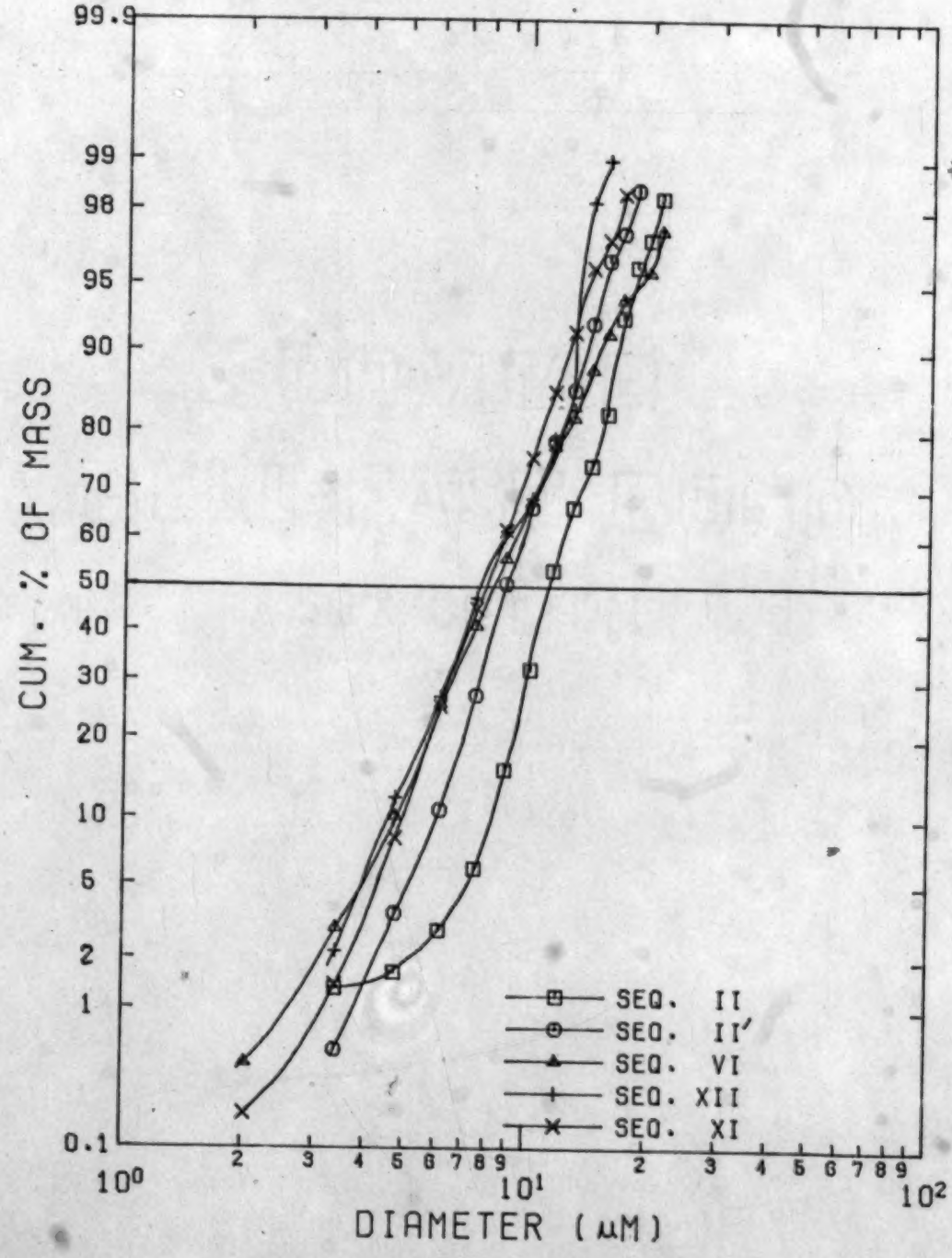

Figure 14. The percentage of mass contained in droplets smaller than or equal to a given diameter as a function of the diameter. The mass median diameters are 11.4, 8.8, 8.2, 7.6, and 7.9 μm for sequences II, II', VI, XII, and XI respectively.

Both of the methods described in Chapter 4 were employed for the determination of the cloud droplet water content of the atmosphere in the cloud chamber. The second technique, which was based upon measurements of the mass of accretion upon the slide during its exposure within the cloud chamber, was used for the same experiments as those mentioned above for the first technique (SEQ. II, SEQ. II′, SEQ. VI, SEQ. XI, and SEQ. XII). The results of these measurements are summarized in Tables 1 and 2. The second column of Table 1 gives the total period of operation of the spraying system during a particular run. The third column is the cumulative operating time of the sprayers to the end of the experiment, a parameter on which a linear interpolation (or extrapolation) was performed in order to obtain the cloud droplet water contents for experiments other than those during which measurements were taken. The actual times (in terms of the cumulative operating time of the sprayers) at which slides were removed following exposure in the cloud chamber, are given in columns 4 and 2 of Tables 1 and 2 respectively. Column 5 of Table 1 gives the exposure time of the gelatin-coated slides within the cloud chamber. The mass of material which accreted (during the collection period given in column 4 of Table 2) upon the uncoated slides is in column 3 of Table 2. The interpolated (or extrapolated) values of the cloud droplet water content for the two methods are given in column 6 of Table 1 and column 5 of Table 2, respectively. The interpolation/extra-

Table 1. The sprayer operating characteristics, and the parameters derived from the gelatin coated slides.

SEQ. NUMBER	SPRAYER OPERATING TIME (min.)	CUMULATIVE OPERATING TIME (min.)	GELATIN SLIDE SAMPLING TIME (min.)	COLL. PERIOD (s)	DIST'N. DETERMINED WATER CONTENT (g kg^{-1})
I	17.0	17.0			0.55
II	27.5	44.5	24.0	90.	0.57
II	27.5	44.5	24.0	90.	0.51
III	16.5	61.0			0.49
IV	15.0	76.0			0.47
V	16.5	92.5			0.45
VI	32.5	125.	118.5	120.	0.41
VII	18.5	143.5			0.39
VIII	23.0	165.5			0.36
IX	19.0	185.5			0.34
X	21.0	206.5			0.31
XI	15.5	222.0	219.	120.	0.30
XII	18.5	240.5	240.5	90.	0.59

Table 2. The parameters derived from the uncoated slides.

SEQ. NUMBER	ACCRETED MASS SLIDE SAMPLING TIME (min)	ACCRETED MASS (mg)	COLLECTION PERIOD (s)	ACCRETED MASS DERIVED WATER CONTENT (g kg^{-1})
I				1.05
II	44.5	13.0	600.	1.1
III				1.1
IV				1.15
V				1.15
VI	125.0	12.1	720.	1.2
VII				1.1
VIII				0.95
IX				0.8
X				0.7
XI	216.5	3.2	460.	0.6
XII	228.0	12.0	360.	2.95

polation procedure was adopted because it was believed that the sprayer-produced cloud droplet characteristics should vary approximately linearly with the total operating time of the spraying units. Variations in the sprayer output were due primarily to the following factors, listed in increasing order of probable significance:

(i) The pressure head of the water input to the sprayers decreased slowly during each run, but this variation was never more than 15% of the original value.

(ii) The slot in the sprayer ball did partially clog up with impurities in the air supply on one occasion before these experiments were begun, so that although the slots were checked after each run, some decrease of sprayer output could have resulted if a partial clogging went undetected.

(iii) The sprayer hoses had a tendency to fill with ice as a result of large droplets being trapped by the corrugated walls of the hoses during sprayer operation. This resulted in reduced spray output in the cloud chamber, but the hoses were defrosted after most experimental runs, so this should not have led to a gradual reduction in the spray output over the period of a number of runs.

(iv) The air pressure input to the sprayers slowly decreased from SEQ. I until SEQ. XI, when the reduced pressure was discovered. The cause was a sublimation of water vapor within the air chilling coil, producing an increasing constriction to airflow through the tube. The problem went undetected for a substantial period because the

air pressure gauge was located upstream of the chilling coil. The problem was solved before SEQ. XII, and resulted in the much higher water contents measured for that run.

Since the last factor likely produced the greatest portion of variation from run to run, and since it was dependent upon the total sprayer operating time, this latter parameter has been used for the interpolation/extrapolation procedure.

5.4 The Quantitative Analysis of Prolonged Accretion.

Tables 22 through 33 of Appendix D give the maximum length of the substrate growths as a function of the growth time for each of the 12 prolonged accretion sequences. These data are plotted in Figs. 15 through 18, from which the mean rate of accretion for each of the 12 sequences has been determined. The mean rates have been obtained by hand-fitting curves to the plotted points. This procedure was adopted because it enables the mean rate of linear growth to be determined for situations like those in Fig. 18 where the growth length is not increasing monotonically.

The rate of growth in each of the sequences in Figs. 15, 16, and 17 is nearly constant. While the rates of growth vary considerably with the velocity of the substrate, there is less variation with changes in air temperature.

Fig. 18 displays the growth characteristics for a needle substrate at velocities of 50 and 250 cm s^{-1}. The

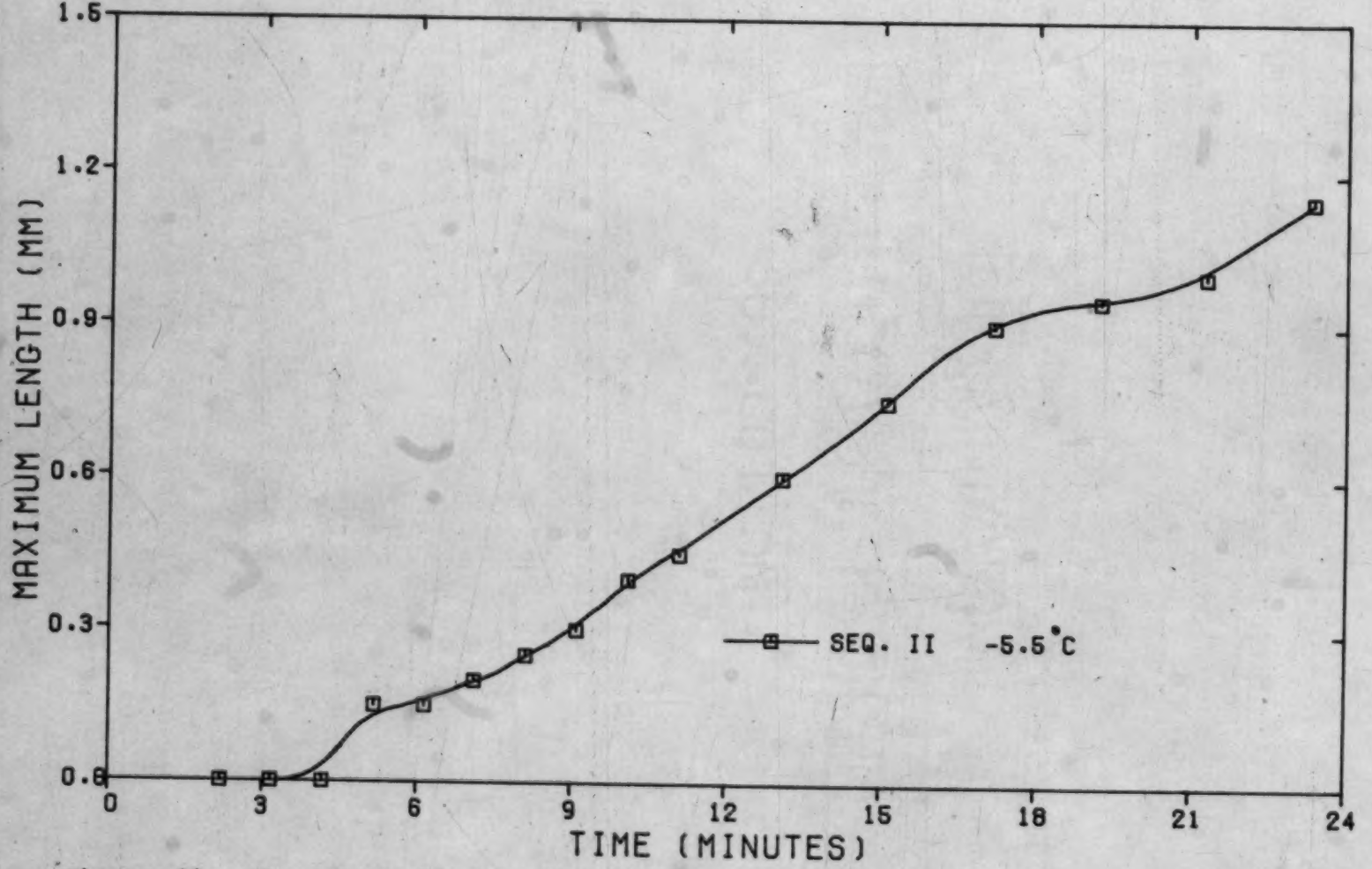

Figure 15. The maximum length of the accreted deposit as a function of its time of growth.

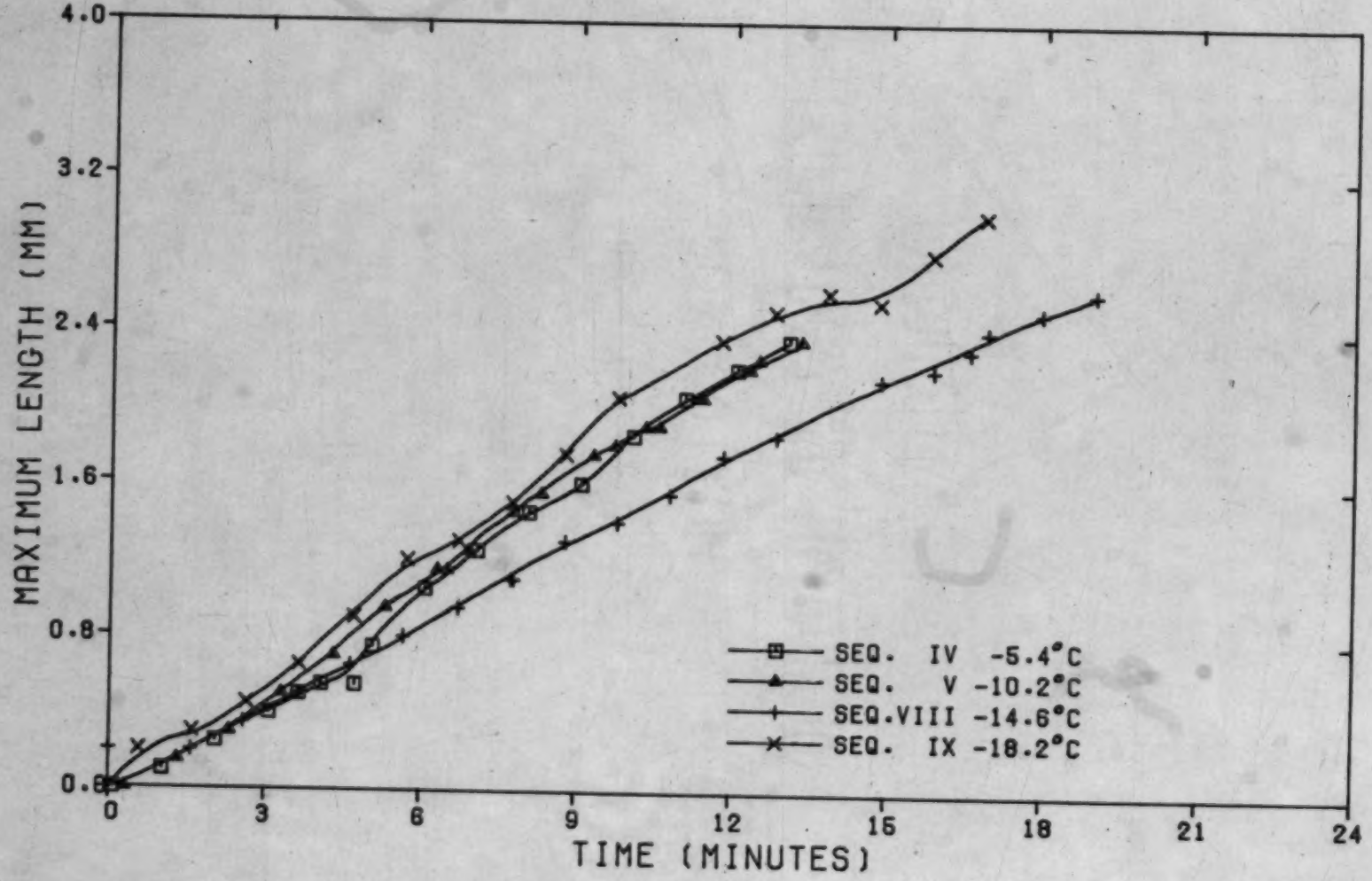

Figure 16. As in Fig. 15.

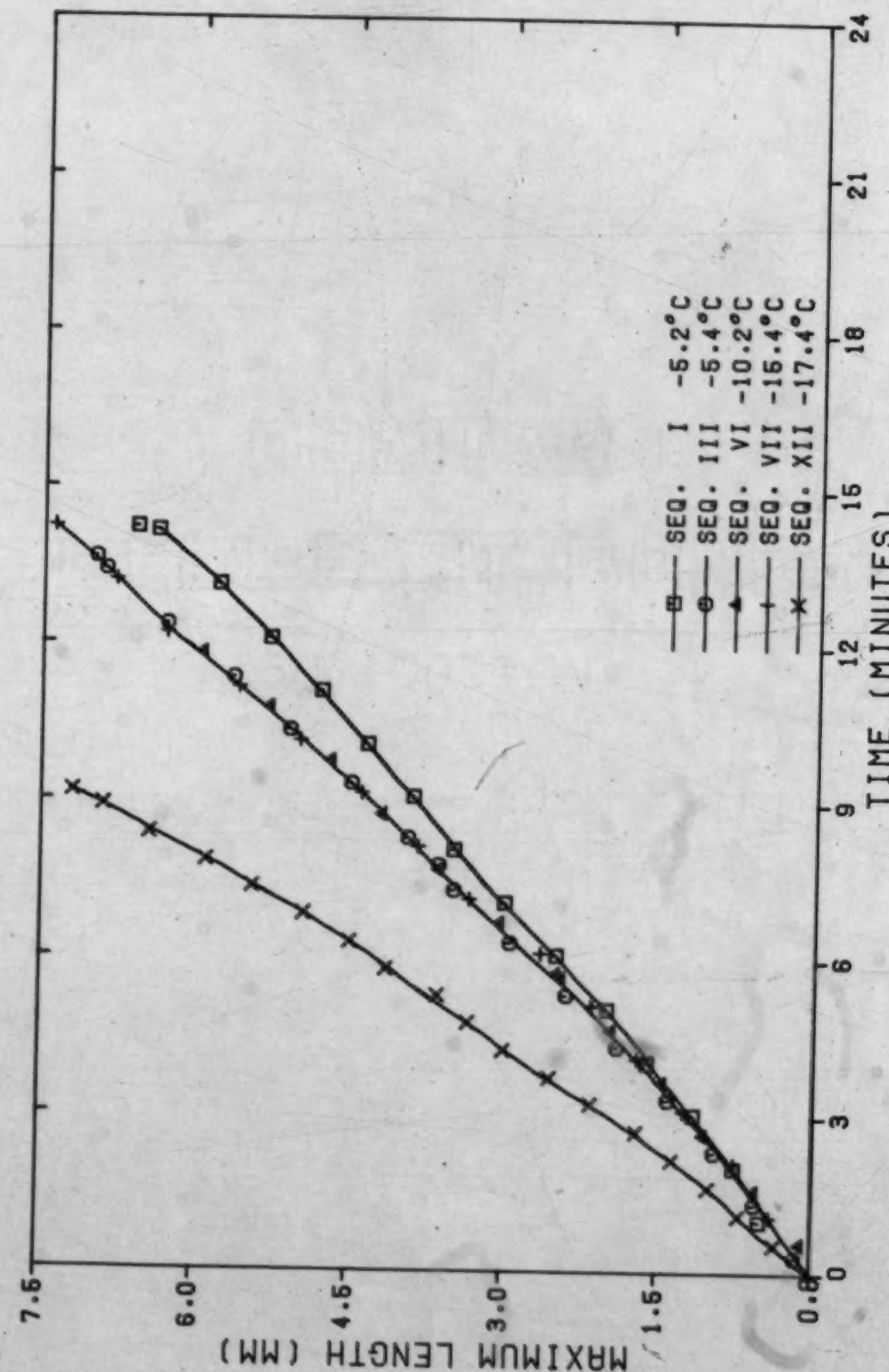

Figure 17. As in Fig. 15.

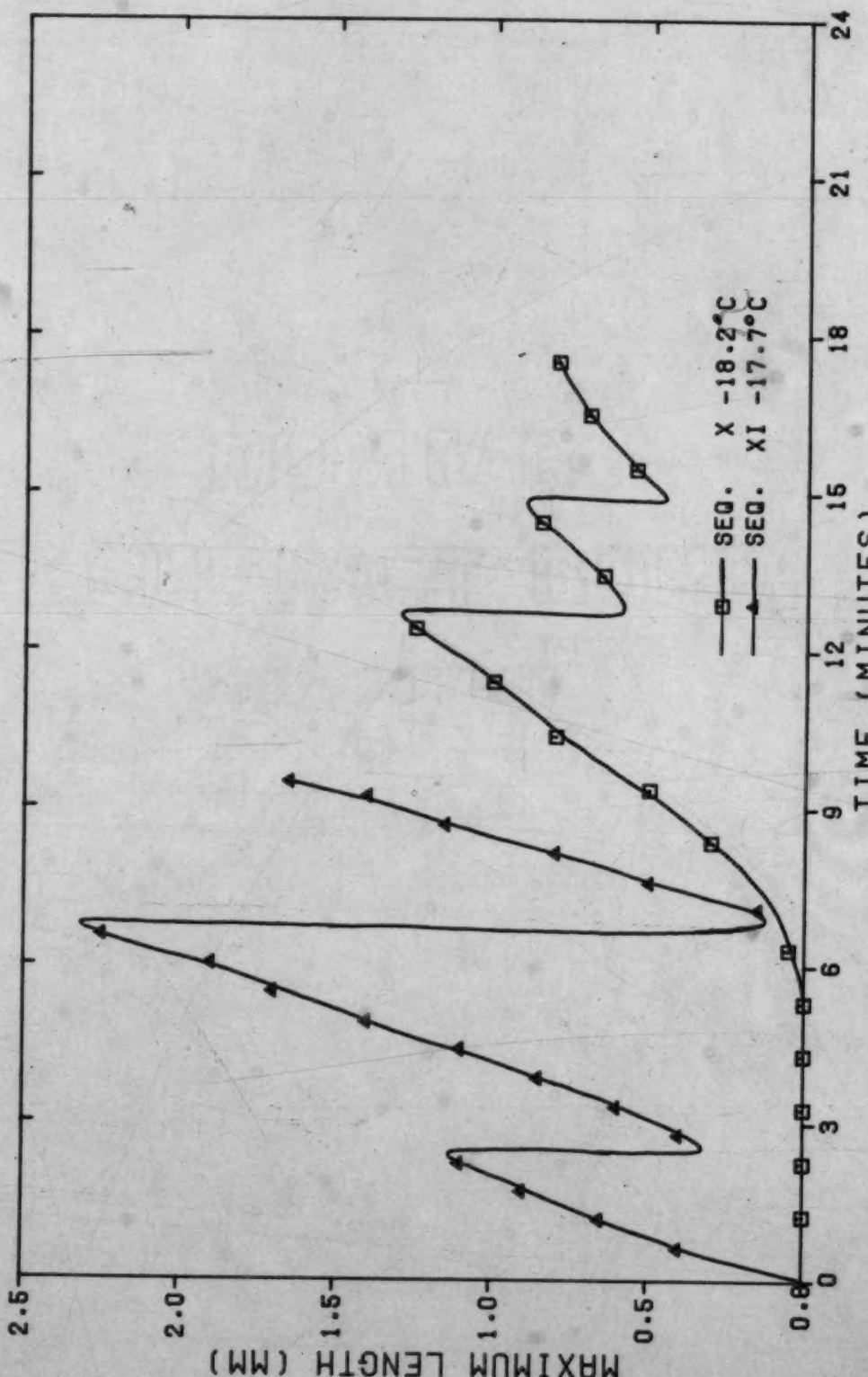

Figure 18. As in Fig. 15.

breakage of the growth near its point of attachment to the substrate is also evident in this figure. The growth rate of the material accreting on the needle appears to be nearly constant following each growth detachment for both of the sequences of Fig. 18. When the needle velocity is 2.5 m s^{-1}, as in SEQ. XI, the growth begins almost immediately, and the rate of growth remains approximately constant thereafter. However, at a needle velocity of 50 cm s^{-1} (SEQ. X), virtually no accretion takes place during the first 6 minutes. Careful scrutiny of the negatives of this sequence confirms the very slow rate of growth in the direction of motion until sufficient riming occurs to increase the width of the material at the end of the needle to about 100 or 200 μm. The subsequent breakage of the growth leaves behind a section of accreted material of at least 400 μm diameter, so that growth upon this material can begin once again at approximately the same rate as that before the breakage.

In Tables 3, 4, and 5, the sequence order has been rearranged from that of the previous tables so that it corresponds to the order in Figs. 15 through 18 (that is the ordering is first with increasing substrate velocity, and second with decreasing air temperature). The two sequences involving riming upon the needle substrate have been placed at the ends of the tables.

In Table 3, column 4 gives the mass of the material which accreted upon the substrate; column 5

Table 3. Properties of the substrate accreted deposit.

SUBSTRATE VELOCITY (cm s^{-1})	MEAN AIR TEMP. (°C)	SEQ. NUMBER	SUBSTRATE ACCRETED MASS (mg)	GROWTH VOLUME (10^{-3} cm^3)	GROWTH MEAN DENSITY (g cm^{-3})	GROWTH TIME (mm:ss)
0.	-5.4	II		0.55		25:25
50.	-5.4	IV	0.35	0.75	0.05	13:05
50.	-10.2	V		0.69		13:20
50.	-14.6	VIII	1.0	1.6	0.06	19.01
50.	-18.2	IX		1.6		16:52
250.	-5.2	I	6.1	3.0	0.20	14:15
250.	-5.4	III	6.0	4.0	0.15	13:40
250.	-10.2	VI	3.6	3.3	0.11	11:50
250.	-15.4	VII	5.2	5.2	0.10	15:15
250.	-17.4	XII	3.8	4.4	0.09	9:10
50.	-18.2	X	0.3	0.18	0.17	12:42
250.	-17.7	XI		0.16		4:12

Table 4. The mean linear growth rates and mass growth rates for the deposits.

SEQ. NUMBER	MEAN LINEAR GROWTH RATE (10^{-4} cm s^{-1})	TYPE 1 NORM. LINEAR GROWTH RATE (10^{-4} cm s^{-1})	TYPE 2 NORM. LINEAR GROWTH RATE (10^{-4} cm s^{-1})	MEAN MASS GROWTH RATE (10^{-7} g s^{-1})	TYPE 1 NORM. MASS GROWTH RATE (10^{-7} g s^{-1})	TYPE 2 NORM. MASS GROWTH RATE (10^{-7} g s^{-1})
II	0.98	1.7	0.9			
IV	3.3	7.0	2.9	4.5	9.6	3.9
V	3.3	7.3	2.8			
VIII	2.4	6.7	2.6	8.8	24.4	9.4
IX	3.3	9.7	4.0			
I	7.4	13.5	7.0	71.	129.	67.
III	8.8	18.0	7.9	73.	149.	65.
VI	9.1	22.2	7.6	51.	124.	43.
VII	9.1	23.3	8.4	57.	146.	53.
XII	13.0	22.0	4.4	69.	117.	24.
X	3.7	11.9	5.4	3.9	12.6	5.7
XI	8.5	28.3	13.7			

summarizes the values of growth volume given in Tables 34 through 45 of Appendix D; and column 6 presents the resulting mean density of the accreted material as a whole. Some values of the accreted mass are missing because either the mass was too small to be measured accurately using the Mettler balance, or in the case of SEQ. II, because the growth was accidentally destroyed before its mass could be determined. Since the calculated volume, in many cases, includes a hollow region near the center of the growth, the gross density as given should not be interpreted as the density of the rimed material itself. This is substantiated by experiments SEQ. I and SEQ. III which were run under almost identical conditions in order to check upon the reproducibility of the results. The difference in mean density between them is likely due primarily to a variation in configuration of the individual growths making up the deposit leading to a considerably different enclosed volume. The period over which the growth occurred is given in column 7.

The mean rate of increase in the maximum length of the accreted material is given in column 2 of Table 4. Columns 3 and 4 contain the values of column 2 to be expected for a unit cloud droplet water content. The water contents used for the normalization were those measured by the two techniques described in Chapter 4, and are referred to here as Types 1 and 2 respectively. After normalization, the Type 2 linear growth rates vary from $9X10^{-5}$ to

Table 5. The mean frontal area of the growth along with Type 1 and 2 collection efficiencies.

SEQ. NUMBER	GROWTH MEAN FRONTAL AREA (10^{-2} cm^2)	TYPE 1 POTENTIAL MASS ACCRETED (mg)	TYPE 1 COLLECTION EFFICIENCY	TYPE 2 POTENTIAL MASS ACCRETED (mg)	TYPE 2 COLLECTION EFFICIENCY
II					
IV	1.8	0.41	0.85	1.0	0.35
V					
VIII	3.3	0.83	1.20	2.1	0.48
IX					
I	3.0	4.4	1.39	8.3	0.73
III	3.9	4.8	1.25	10.7	0.56
VI	3.4	3.1	1.16	8.8	0.41
VII	4.3	4.8	1.08	13.2	0.39
XII	4.0	4.0	0.95	19.9	0.19
X	1.1	0.16	1.88	0.35	0.86
XI					

$1.37X10^{-3}$ cm s^{-1}. The lowest value occurs when the substrate is not moving, as would be expected. The values corresponding to the substrate moving at 50 cm s^{-1} have a mean of $3.1X10^{-4}$ cm s^{-1}, about 3.4 times greater than the previous case. There does not appear to be any systematic variation of these rates with temperature however. At the higher speed of 2.5 m s^{-1}, the average linear growth rate is $7.1X10^{-4}$ cm s^{-1}, again with no apparent variation with temperature. Interestingly, the growth rates with the needle substrate are much higher than with the hexagonal plate, for the same velocities. This is particularly puzzling since the growth rates of the deposits on the needles are constant with time (at least during the length of these experiments) and the rate of growth does not

correspond to that for the hexagonal plate cases even when the diameter of the deposit is the same. This effect merits further study.

The mean mass growth rates of column 5, Table 4, have been determined by dividing the accreted mass by the period of accretion. The Type 1 and Type 2 normalized mass growth rates are in columns 6 and 7. These growth rates display a much greater variation among experiments with the same velocity than do the normalized linear growth values, although the SEQ. I and SEQ. III values are almost identical, as would be expected. It is believed that this variation is not real, but that it results from an inaccuracy in the measurement of the masses of the growths. This error could be partially due to the operation of the balance under difficult operating conditions. Low temperatures and vibration produced by the compressors associated with the first cold-room may have affected the accuracy of these measurements. However, a more likely cause was the inability to ensure that the correct amount of rime was scraped off the substrate and onto the balance pan. The mass of material was very small, and even the slightest error in determining the extent of rime to remove could have led to a considerable error in the mass measurement.

Column 2 of Table 5 gives the time mean frontal area of the accreted mass which was calculated using the formula

$$\bar{A}_f = \frac{\pi}{12}\left(D_i^2 + D_i D_f + D_f^2\right) \qquad (5.1)$$

where D_i is the diameter of the substrate, and D_f is the average diameter of the growth at its widest point (near the end). This relation is based upon the assumption that the diameter of the end of the growth increases linearly with time. Using these values, the total mass of the cloud droplets in the volume swept out by the substrate and accreted material was determined by

$$M = v \rho_a \bar{A}_f t L \qquad (5.2)$$

where v is the velocity of the substrate, ρ_a is the air density, $\bar{A}_f$ is the time mean frontal area of the substrate, t is the growth period, and L refers to the cloud droplet water content of the air in the cloud chamber. The collection efficiencies of the growths were obtained by using the Type 1 and 2 cloud droplet water contents. These efficiencies are presented in columns 4 and 6 of Table 5. The Type 1 efficiencies vary from 0.85 to 1.88, a result that is not particularly surprising because of the significant underestimate of the cloud droplet water content by this technique as mentioned earlier. The Type 2 efficiencies lie between 0.19 and 0.86. There does not appear to be a strong dependence upon either the air temperature or the substrate velocity, although by excluding SEQ. XII, the higher velocity experiments have a slightly

higher mean efficiency associated with them. The lack of a significant difference between these groups may again have been due to an inaccuracy in the determination of the mass of the deposits.

CHAPTER VI

CONCLUSIONS AND RECOMMENDATIONS

6.1 A Summary of the Results.

During the very earliest stages (first 15 s) of accretion upon a hexagonal plate, the most rapid riming occurs along the perimeter of the plate. This effect has been previously noted to occur on natural hexagonal plate ice crystals (Knight and Knight, 1973). As the accretion period lengthens to 1 or 2 minutes, the riming becomes most pronounced near the corners of the plate. Even after as long as 4 min, the deposits which have formed near the corners may continue to grow with few, if any, common points of attachment.

The deposit formed on the hexagonal plate substrate 'fans out' into the wind at an angle which is smaller than that commonly associated with conical graupel. The angle appears to increase as the velocity of the substrate decreases, however at the same time, the deposit takes on a more dendritic appearance, making the determination of a growth angle more difficult. This dendritic structure leads to a decrease in the gross density of the deposit as the temperature of formation is lowered

and/or the velocity is decreased.

The growths formed on the hexagonal plates at temperatures below −10°C are very fragile and appear to be susceptible to breakage, especially near their point of attachment to the plate. This is also true of the growths formed upon the needle substrates, where almost all of the deposit may break off. The rate of growth of the maximum length of the deposit following each loss of material is approximately the same, and is much greater than that during the initial stages of accretion upon the needle.

The rates of increase of the maximum length of the growths are approximately constant (for given temperature and velocity) throughout the first 15 min of formation. When these rates are normalized to a unit cloud droplet water content, they provide a means of comparing the rate of growth for varying temperatures and substrate velocities. If the Type 2 normalized linear growth rates are set into groups according to the velocity of the substrate, then the between-group variation for the 50 cm s^{-1} and 2.5 m s^{-1} groups is numerically over 3 times as large as the within-group variation (excepting the SEQ. XII value) associated with temperature changes in either group.

When the droplet depositional mass (Type 2) method of determining the water content of the cloud chamber atmosphere is employed, the collection efficiencies of the prolonged growths vary between about 0.19 and 0.86. The mean gross density of the deposits has a range of 0.05 to

0.20 g cm^{-3}. The average density for the growths at 50 cm s^{-1} is less than half the average for the growths at 2.5 m s^{-1}, however, a large variation exists in the latter group. There is no consistent dependence of the collection efficiency upon the air temperature or the substrate velocity; however this effect may be due to the fact that a relatively large inaccuracy in the measurement of the mass of the deposits on the substrate has obscured any small consistent variation that may be occurring.

6.2 Conclusions.

This study has demonstrated that during the early stages of riming upon a hexagonal plate, the most rapid accretion occurs first along the perimeter of the plate, followed slightly later by preferential riming at the corners. In many cases the growths at the corners had few points of attachment between them and were joined to the substrate over an area that was small compared to the total area of the plate. As a result, the growths displayed a potential for breaking near their point of attachment, and then either pivoting outward about this point, or breaking completely away from the substrate. Since this is essentially the method of graupel formation postulated by Knight and Knight (1973), this study lends support to that theory as a mechanism for the generation of conical graupel.

The rate of growth (in terms of both the mass and the length) of the deposit was found to be directly related

to the velocity of the substrate, but showed little correlation with the temperature of formation. The type of substrate (hexagonal plate or needle) also affected the rate of growth. The length of the deposit at the end of the needle increased very slowly until an apparent 'threshold diameter' was reached, at which time the rate increased substantially, surpassing the rate of length increase observed for accretion on a hexagonal plate-initiated deposit of the same diameter. The reason for this behavior is not understood and merits further study.

The use of estimates of the gross volume and gross frontal area of the deposits as a basis for the calculation of the density and collection efficiency of the growths is thought to be the primary reason for the lack of an apparent correlation between the substrate velocity and growth temperature on the one hand, and the density and collection efficiency on the other. In addition, because of the relatively small mass median diameter and dispersion of the droplet distribution in the cloud chamber, only the larger droplets may have been involved in the riming process, thus further lowering the collection efficiency. This effect is predicted by Fig. 7.

6.3 Recommendations for Future Studies of Graupel Formation.

A number of recommendations may be made with regard to the apparatus and techniques employed in this study:

(i) Since many of the qualitative and quantitative aspects of a study of this nature depend upon the cloud droplet water content (or concentration), an effort should be made to improve the quality of these measurements. Specifically, if gelatin-coated slides are to be used, the thicker gelatin coating (15% solution of gelatin in water) used in conjunction with the Nomarski interference technique of illumination provides the most consistent results. It is important that care be taken to maintain a constant thickness of the gelatin coating. Also, an effort should be made to determine, with greater accuracy, the calibration factor between the crater diameter and the diameter of the droplet which generated it. An improvement in the accuracy and particularly of the efficiency of the analysis of these slides could be achieved through the measurement of the diameter of the craters by employing either a calibrated wedge overlay, or a digitizing table and computer. Along with this increase in efficiency, an effort should be made to sample the cloud chamber atmosphere during each run in order to minimize or remove interpolation errors.

(ii) As discovered following the completion of these experiments, the oil-coated slides provide a much better estimate of the cloud droplet size distribution and water content than do the gelatin-coated slides at the impact velocities encountered in this study. If the oil is pre-exposed to water droplets, and then allowed to stand sufficiently long for the droplets to disappear (about

10 min), the rate of evaporation of the droplets within the oil on subsequent exposures will be minimized. The above comments on improving the analysis of the gelatin-coated slides apply equally well for the oil-coated ones.

(iii) If possible, two cameras positioned at 90° to each other should be used simultaneously to obtain photographs of the accretion of material upon the substrate. In this way the volumetric rate of growth can be determined.

(iv) In order to increase the efficiency of the data collection process, the maintenance of a constant boom rotation rate should be carried out automatically, using an electronic motor speed controller. This will free the observer from prolonged exposure within the cold-room.

(v) The length of the boom should be maximized so as to minimize the centripetal forces acting upon the deposit, thus producing a more realistic simulation of the accretion process.

(vi) The sprayers should be better insulated to maintain an operating temperature closer to that within the cold-room, and to reduce the temperature variation both in space and time within the cloud chamber.

(vii) Great care should be taken in determining the mass of the accreted material since the quantity of material is very small, and variations of substantial fractions of the mass can occur because of the difficult conditions under which this measurement must be made. Should the technique employed in this study prove to be insufficiently accurate

(as appears to be the case from these results), then another method should be attempted. One possibility would be to measure the dimensions of the 'hemisphere' of water formed by a melting of the deposit.

(viii) Better means should be found for determining the volume of the accreted material itself, as opposed to the gross volume which was measured in this study. This might be accomplished by immersing the deposit in a liquid such as hexane (after filling the pores with phthalic acid), and determining the resulting displacement. The change in technique should provide for better estimates of the deposit volume and collection efficiency.

(ix) The droplet size distribution should be varied to permit a study of the variation of the accretion characteristics with a change in the mass median diameter of the droplet distribution.

(x) A further study should be made of the variations in the rate of growth of deposits with changes in the diameter and shape of the substrate.

REFERENCES

Abraham, F.F., 1970: Functional dependence of drag coefficient of a sphere on Reynolds Number. Phys. Fluids, 13, 2194–2195

Arenberg, D.L., 1941: The formation of small hail and snow pellets. Bull. Am. Meteor. Soc., 22(3), 113–116.

Auer, A.H., and D.L. Veal, 1970: The dimension of ice crystals in natural clouds. J. Atmos. Sci., 27(6), 919–926.

Bashkirova, G.M., and T.A. Pershina, 1964: On the mass of snow crystals and their fall velocity. Trudy G. G. O., 165, 90–100.

Browning, K.A., 1975: The structure and mechanism of hailstorms. Preprints, NHRE Symposium-Workshop on Hail, Estes Park, 1, VII.a.1–VII.a.106.

____, and G.B. Foote, 1975: Airflow and hail growth in supercell storms and some implications for hail suppression. Submitted to Mon. Wea. Rev.

____, F.H. Ludlam, and W.C. Macklin, 1963: The density and structure of hailstones. Quart. J. Roy. Meteor. Soc., 89, 75–84.

Brownscombe, J.L., and J. Hallett, 1967: Experimental and field studies of precipitation particles formed by the freezing of supercooled water. Quart. J. Roy. Meteor. Soc., 93(398), 455–473.

Cannon, T.W., and J.D. Sartor, 1974: Ice phase propagation and modification in developing continental cumuli. Preprints, 4th Conf. On Weather Modification, Ft. Lauderdale, 125–132.

Charlton, R.B., and R. List, 1972: Hail size distributions and accumulation zones. J. Atmos. Sci., 29(6), 1182–1193.

Cheng, L.H., 1975: A numerical simulation of the initiation of graupel growth. M.SC. THESIS, DEPT. OF GEOGRAPHY, UNIV. OF ALBERTA, 115 PP.

Christensen, L., V. Keller, and J. Hallett, 1974: Ice particle concentration in prehail convective clouds in Colorado. Preprints, Conf. On Cloud Physics, Tuscon, 191–194.

Davis, C.I., and A.H. Auer Jr., 1974: Use of isolated orographic clouds to establish the accuracy of diffusional ice crystal growth equations. Preprints, Conf. On Cloud Physics, Tuscon, 141–147.

Dennis, A.S., 1974: Numerical analysis of proposed hail suppression concepts. Report 74–13, Inst. Atmos. Sci., South Dakota School of Mines and Technology, 18 pp.

____, 1975: Hail suppression concepts and seeding methods. Preprints, NHRE Symposium-Workshop on Hail, Estes Park, 1, IX.a.1–IX.a.25.

____, and D.J. Musil, 1973: Calculations of hailstone growth and trajectories in a simple cloud model. J. Atmos. Sci., 30, 278–288.

Dresner, S., 1973: It's superspray. Popular Science, 202(5), 102–164.

Dye, J.E., 1974: Observations of precipitation development in cumulus congestus clouds on July 9, 1973. Preprints, Conf. On Cloud Physics, Tuscon, 148–151.

____, C.A. Knight, and T.W. Cannon, 1974a: The potential for rainfall modification in some Great Plains cumuli. Preprints, 4th Conf. On Weather Modification, Ft. Lauderdale, 13–15.

----, ----, V. Toutenhoofd, and T.W. Cannon, 1974b: The mechanism of precipitation formation in North-Eastern Colorado cumulus. III. Coordinated microphysical and radar observations and summary. J. Atmos. Sci., 31(8), 2152-2159.

Fletcher, N.H., 1969: The Physics of Rainclouds, Cambridge, Cambridge Univ. Press, 389 pp.

Fowler, M.G., H.H. Blau, and E.W. Fasci Jr., 1974: Cloud droplet measurements in cumuliform and stratiform clouds. Preprints, Conf. On Cloud Physics, Tuscon, 296-299.

Fukuta, N., 1969: Experimental studies on the growth of small ice crystals. J. Atmos. Sci., 27(7), 1068-1073.

Gagin, A., 1975: The ice phase in winter continental cumulus clouds. J. Atmos. Sci., 32(8), 1604-1614.

Garland, J.A., 1971: Some fog droplet size distributions obtained by an impaction method. Quart. J. Roy. Meteor. Soc., 97(414), 483-494.

Heymsfield, A., 1972: Ice crystal terminal velocities. J. Atmos. Sci., 29(7), 1348-1357.

Hobbs, P.V., 1975: The nature of winter clouds and precipitation in the Cascade Mountains and their modification by artificial seeding. Part I: Natural conditions. J. Atmos. Sci., 14(5), 783-804.

Holroyd, E.W. III, 1964: A suggested origin of conical graupel. J. Atmos. Sci., 3(5), 633-636.

Iribarne, J.V., and R.G. dePena, 1960: The influence of particle concentration on the evolution of hailstones. Nubila, 5, 7-30.

Jayaweera, K.O., and R.E. Cottis, 1969: Fall velocities of plate-like and columnar ice crystals. Quart. J. Roy. Meteor. Soc., 95(406), 703-709.

____, and B.F. Ryan, 1972: Terminal velocities of ice crystals. Quart. J. Roy. Meteor. Soc., 98(415), 193-197.

Kajikawa, M., 1972: Measurement of falling velocity of individual snow crystals. J. Meteor. Soc. Japan, 50(6), 577-584.

Kartsivadze, A.I., 1969: Modification of hail processes. Proc., Int'l. Conf. Cloud Physics, Toronto, 778-788.

Knight, C.A., and N.C. Knight, 1971: Hailstones. Sci. Am., 224(4), 97-103.

____, and ____, 1973: Conical graupel. J. Atmos. Sci., 30(1), 118-124.

____, ____, J.E. Dye, and V. Toutenhoofd, 1974: The mechanism of precipitation formation in North-Eastern Colorado cumulus. I. Observations of the precipitation itself. J. Atmos. Sci., 31(8), 2142-2147.

LaChapelle, E.R., 1969: Field Guide to Snow Crystals, Seattle, Univ. Of Washington Press, 101 pp.

List, R., 1960: Growth and structure of graupel and hailstones. Geophys. Monogram., 5, 317-324.

____, 1965: The mechanism of hailstone formation. Proc. Int'l. Conf. Cloud Physics, Tokyo, 481-491.

____, and R.S. Schemenauer, 1971: Free fall behavior of planar snow crystals, conical graupel and small hail. J. Atmos. Sci., 28, 110-115.

Litt, M., and D.E. Swift, 1972: The Babington nebulizer: A new principle for generation of therapeutic aerosols. Am. Rev. Respiratory Disease, 105(2), 308-310.

Locatelli, J.D., and P.V. Hobbs, 1974: Fall speeds and masses of solid precipitation particles. J. Geophys. Res., 79(15), 2185-2197.

Macklin, W.C., and G.S. Payne, 1969: The spreading of accreted drops. Quart. J. Roy. Meteor. Soc., 95(406), 724-730.

Magono, C., and C.W. Lee, 1966: Meteorological classification of natural snow crystals. J. Faculty Sci., Horraido Univ., VII(2), 321-335.

Mason, B.J., 1971: The Physics of Clouds, 2nd Edition, Oxford, Clarendon Press, 671 pp.

McLeod, C., 1976: Microphysical measurements in Alberta thunderstorms. M.Sc. Thesis, Dept. of Meteor., McGill Univ.

Nakaya, U., 1951: The formation of ice crystals. Compendium of Meteorology, T.F. Malone, Ed., Boston, Am. Meteor. Soc., 207-220.

Owens-Illinois, 1974: The Hydro-Sphere nebulizer. Sales Brochure, Owens-Illinois Inc.

Pitter, R.L., and H.R. Pruppacher, 1974: A numerical investigation of collision efficiencies of simple ice plates colliding with supercooled water drops. J. Atmos. Sci., 31(2), 551-559.

Ranz, W.E., and W.R. Marshall, 1952: Evaporation from drops. Chem. Eng. Progress, Pt. I, 48(3), 141, Pt. II, 48(4), 173.

Reinking, R.F., 1975: Formation of graupel. J. Appl. Meteor., 14(5), 745–754.

Reynolds, O., 1876: Formation of raindrops and hailstones. Nature, 15, 163–165.

Ryan, R.T., H.H. Blau Jr., P.C. Von Thuna, M.L. Cohen, and G.D. Roberts, 1972: Cloud microstructure as determined by an optical cloud particle spectrometer. J. Appl. Meteor., 11(1), 149–156.

Sasyo, Y., 1971: Study of the formation of precipitation by the aggregation of snow particles and the accretion of cloud droplets on snowflakes. Papers in Meteor. & Geophys., 22(2), 69–142.

Schaefer, V.J., 1951: Snow and its relationship to experimental meteorology. Compendium of Meteorology, T.F. Malone, Ed., Boston, Am. Meteor. Soc., 221–234.

____, 1964: Preparation of permanent replicas of snow, frost and ice. Weatherwise, XVII(6), 278–287.

Strong, C.L., 1966: The amateur scientist – On preserving the shapes of snow crystals by catching snowflakes in dissolved plastic. Sci. Am., 214(3), 120–126.

Sulakvelidze, G.K., S.H. Bibilashvili, and V.F. Lapcheva, 1967: Formation of precipitation and modification of hail processes. Israel Prog. Sci. Translations, Jerusalem, 208 pp.

____, B.I. Kiziriya, and V.V. Tsykunov, 1974: Progress of hail suppression work in the USSR. Weather and Climate Modification, W. Hess, Ed., New York, J. Wiley & Sons, 410–431.

Weickmann, H., 1953: Observational data on the formation of precipitation in Cb clouds. Thunderstorm Electricity, H.R. Byers, Ed., Chicago, Univ. Of Chicago Press, 66–138.

Wigley, T.M.L., and M.C. Brown, 1971: Geophysical applications of heat and mass transfer in turbulent pipe flow. Bdry. Layer Meteor., 1, 300–320.

Wojtiw, L., and J.H. Renick, 1973: Hailfall and crop damage in Alberta. Preprints, 8th Conf. On Severe Local Storms, Denver, 138–141.

Zikmunda, J., and G. Vali, 1972: Fall patterns and fall velocities of rimed ice crystals. J. Atmos. Sci., 29, 1334–1346.

APPENDIX A

DROPLET HEAT AND MASS TRANSFER CALCULATIONS

Ranz and Marshall (1952) developed a set of equations (later outlined by Macklin and Payne (1969)) which predict the rate of change of the temperature, the radius, and the velocity of a water droplet which is exposed to air with a given relative velocity, humidity, and temperature.

The rate of cooling of the droplets is given by

$$\frac{dq}{dt} = 4\pi r\,(1+0.3\,Pr^{\frac{1}{3}}\,Re^{\frac{1}{2}})\,k\,(T-T_a)$$
$$+\,4\pi r\,(1+0.3\,Sc^{\frac{1}{3}}\,Re^{\frac{1}{2}})\,L_v\,D\,(\rho_s-\rho_e) \qquad \text{(A1)}$$

where dq is the heat transferred in time dt, r is the radius of the droplet, Pr, Sc, and Re are the Prandtl, Schmidt and Reynolds numbers appropriate to the given conditions, k is the thermal conductivity of the air, T is the droplet's surface temperature (assumed to be the same as the internal temperature), T_a is the air temperature, L_v is the latent heat of vaporization, D is the diffusivity of water vapor in air, ρ_s is the saturation water vapor density of the environment for a given temperature, and ρ_e is the actual water vapor density of the environment. The rate of change of the temperature of the droplet can be

obtained from

$$\frac{dq}{dt} = -\frac{4}{3}\pi r^3 \rho_w c_w \frac{dT}{dt} \qquad (A2)$$

where ρ_w is the water density, and c_w is the specific heat of water. The rate of change of the droplet radius due to evaporation from, or condensation onto the surface of the droplet is given by

$$\frac{dr}{dt} = -\frac{D}{r\rho_w}(\rho_s - \rho_e)(1 + 0.3\,Sc^{\frac{1}{3}} Re^{\frac{1}{2}}). \qquad (A3)$$

The rate of change of the relative velocity between the droplet and the air with time is given by

$$\frac{dV_r}{dt} = -\frac{3}{8}\frac{\rho_a}{r\rho_w} V_r^2 C_D \qquad (A4)$$

where ρ_a is the air density, and the drag coefficient used is that given by Abraham (1970)

$$C_D = \frac{24}{(9.06)^2}\left[1 + 9.06\,Re^{-\frac{1}{2}}\right]^2 \qquad (A5)$$

which is valid for $0 \leq Re \leq 5000$. The rate of change of the position of the droplet is

$$\frac{dX}{dt} = V_a \pm V_r \qquad (A6)$$

where V_a is the air velocity, and the sign depends upon the initial values of the two velocities.

After substituting appropriate values for the various constants, a Runge-Kutta 4th order numerical integration technique was applied to the above equations to obtain the variation of a droplet's radius, temperature, and

velocity as functions of time and thus of a droplet's position following its injection into the sprayer hose by the cloud droplet sprayer. A limitation upon the accuracy of this technique was imposed by its inability to account for the sprayer's expulsion of a quantity of air along with the droplets, and thus of its underestimation of the distance required for the droplets to reach the temperature of the air within the sprayer hose.

In order to determine whether or not the droplets entering the cloud chamber reached the air temperature by the time they had fallen to the level of the moving substrate, the above technique was employed, but with Eq. A4 replaced by Eq. A7:

$$\frac{dV_r}{dt} = -\frac{3}{8}\frac{\rho_a}{r\rho_w} V_r^2 C_D + g. \qquad \text{(A7)}$$

The air temperature within the cloud chamber was postulated to decrease linearly with distance from the top of the chamber.

A portion of the problem of determining the droplet temperature change between the sprayer ball and the substrate involved calculating the change in temperature of the air as it passed through the sprayer hose. For this purpose, the equations of Wigley and Brown (1971) were used. They state that for fully developed turbulent flow through a pipe with constant wall temperature, the relaxation distance (defined as the distance at which the air temperature falls by 1/e of the difference between its initial value, and the

wall temperature) for the air is given as

$$X_o = 36.44 a^{\frac{1}{4}} V^{0.2} \qquad \text{(A8)}$$

where a is the pipe radius, and V is the velocity of the airflow. The actual cross-sectional average temperature at a distance x from the start of the tube is thus given by

$$\bar{T} = T_w + (T_i - T_w) e^{-x/x_o} \qquad \text{(A9)}$$

where T_w is the wall temperature, and T_i the initial air temperature.

The results of these calculations are given in Chapter 3.

APPENDIX B

THE PHOTOGRAPHIC SYNCHRONIZER

The photographic synchronizer employed in this study was designed to perform two functions:

(i) It provided a constant time delay between the reception of a signal from the trigger source, and the output of a signal to the stroboscopic flash. This was necessary to allow for the camera's built-in delay between the shutter release signal, and the actual film exposure. The net result was a properly synchronized camera and flash system.

(ii) In conjunction with the first function, the synchronizer controlled the firing of the flash at the same location for every revolution of the boom. Further, it allowed a camera firing only after a given time interval (determined by the Canon Timer L) had elapsed, and then only in synchrony with the flash. In this way the substrate could be seen through the camera's viewfinder at the same location during every rotation of the boom, while the camera took pictures of the substrate at regular intervals of time as the substrate passed the camera lens.

A circuit diagram of the synchronizer is given in

Fig. 19. The first function is accomplished by IC3, with the delay time variable from about 5 to 170 ms. It was normally set at 100 ms, and the camera shutter was set at 0.125 s so as to ensure an ample opportunity for proper synchronization. The second function is performed by IC1 which, using digital logic, 'decides' whether or not to fire the camera for a given trigger signal depending upon whether or not the time interval set on the timer has expired or not. IC2 provides a signal of sufficient length to the camera to ensure consistent camera firing.

While standard grade electronic components were used in constructing this synchronizer, it is recommended that military grade components be used in the future to ensure even more reliable operation under the extreme temperature conditions the synchronizer is exposed to within the cold-room.

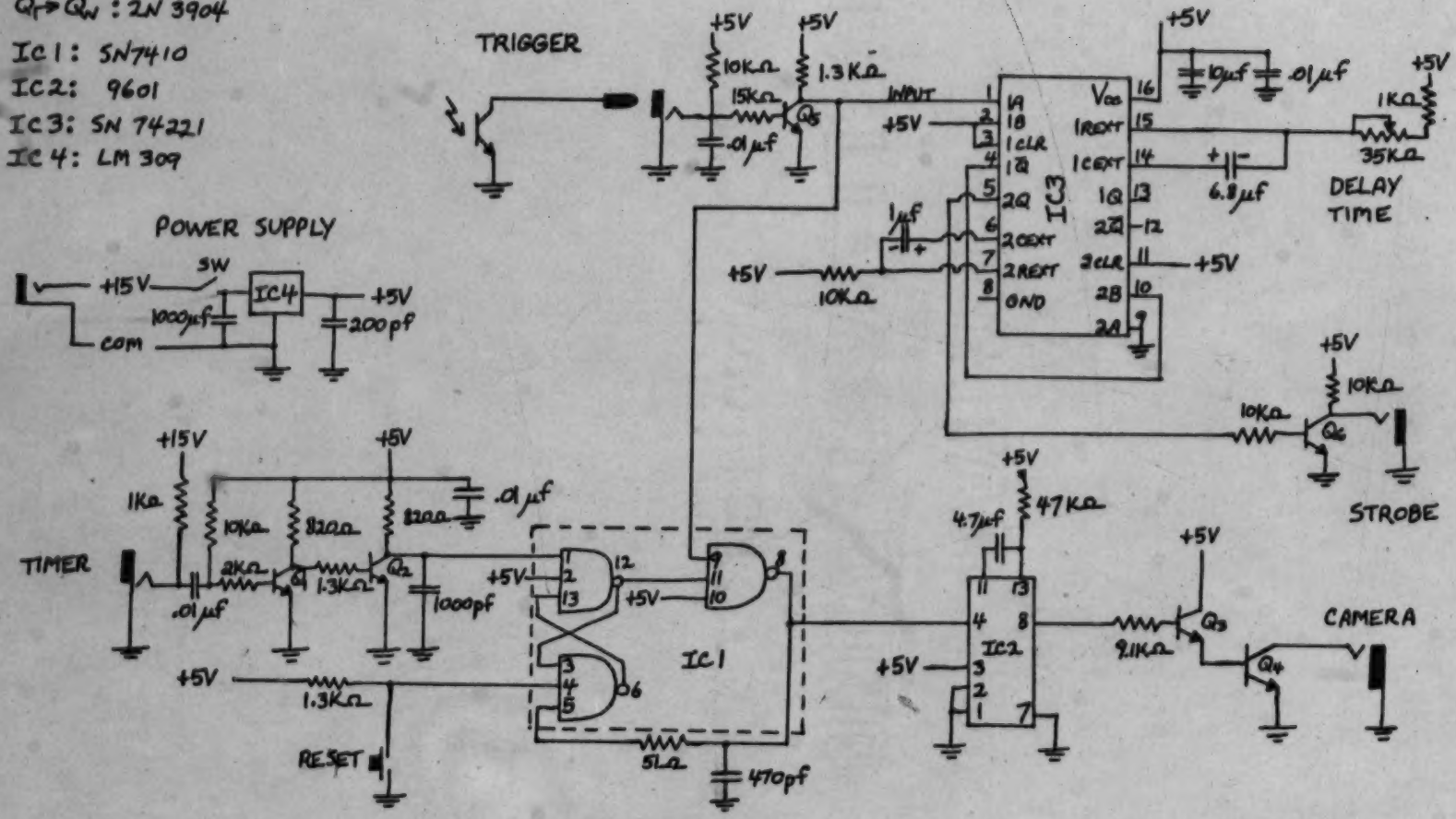

Figure 19. A schematic diagram of the camera synchronizer.

APPENDIX C

DATA OBTAINED FROM

THE CLOUD DROPLET DISTRIBUTION SLIDES

Tables 6 and 7. The data of calibration slides Cal. IA and IB respectively.

PRINT MEASURED DROPLET DIAMETER (MM)	MAGNIFICATION CORRECTED DROPLET DIAMETER (μM)	DROPLET NUMBER	PERCENTAGE OF TOTAL NUMBER	CUMULATIVE PERCENTAGE
0.75	1.7	6	1.4	1.4
1.25	2.8	24	5.8	7.2
1.75	3.9	25	6.0	13.2
2.25	5.0	57	13.7	26.9
2.75	6.1	60	14.4	41.3
3.25	7.2	58	13.9	55.3
3.75	8.3	20	4.8	60.1
4.25	9.4	44	10.6	70.7
4.75	10.6	38	9.1	79.8
5.25	11.7	28	6.7	86.5
5.75	12.8	12	2.9	89.4
6.25	13.9	18	4.3	93.7
6.75	15.0	10	2.4	96.2
7.25	16.1	8	1.9	98.1
7.75	17.2	1	0.2	98.3
8.25	18.3	3	0.7	99.0
8.75	19.4	2	0.5	99.5
10.25	22.8	1	0.2	99.8
11.25	25.0	1	0.2	100.0

PRINT MEASURED DROPLET DIAMETER (MM)	MAGNIFICATION CORRECTED DROPLET DIAMETER (μM)	DROPLET NUMBER	PERCENTAGE OF TOTAL NUMBER	CUMULATIVE PERCENTAGE
1.75	6.6	11	3.8	3.8
2.25	8.5	16	5.5	9.2
2.75	10.4	26	8.9	18.1
3.25	12.3	41	14.0	32.1
3.75	14.2	47	16.0	48.1
4.25	16.0	55	18.8	66.9
4.75	17.9	25	8.5	75.4
5.25	19.8	29	9.9	85.3
5.75	21.7	11	3.8	89.1
6.25	23.6	14	4.8	93.9
6.75	25.5	3	1.0	94.9
7.25	27.4	3	1.0	95.9
7.75	29.2	4	1.4	97.3
8.25	31.1	6	2.0	99.3
9.25	34.9	1	0.3	99.7
12.25	46.2	1	0.3	100.0

Tables 8 and 9. The data of calibration slides Cal. IC and IIA' respectively.

PRINT MEASURED DROPLET DIAMETER (MM)	MAGNIFICATION CORRECTED DROPLET DIAMETER (μM)	DROPLET NUMBER	PERCENTAGE OF TOTAL NUMBER	CUMULATIVE PERCENTAGE
2.50	5.6	34	12.0	12.0
3.50	7.8	42	14.8	26.8
4.50	10.0	47	16.5	43.3
5.50	12.2	46	16.2	59.5
6.50	14.4	41	14.4	73.9
7.50	16.7	27	9.5	83.5
8.50	18.9	21	7.4	90.8
9.50	21.1	10	3.5	94.4
10.50	23.3	4	1.4	95.8
11.50	25.6	8	2.8	98.6
12.50	27.8	1	0.4	98.9
13.50	30.0	1	0.4	99.3
15.50	34.4	2	0.7	100.0

PRINT MEASURED DROPLET DIAMETER (MM)	MAGNIFICATION CORRECTED DROPLET DIAMETER (μM)	DROPLET NUMBER	PERCENTAGE OF TOTAL NUMBER	CUMULATIVE PERCENTAGE
1.25	2.8	60	14.2	14.2
1.75	3.9	45	10.6	24.8
2.25	5.0	31	7.3	32.1
2.75	6.1	44	10.4	42.5
3.25	7.2	72	17.0	59.4
3.75	8.3	41	9.7	69.1
4.25	9.4	37	8.7	77.8
4.75	10.6	25	5.9	83.7
5.25	11.7	28	6.6	90.3
5.75	12.8	11	2.6	92.9
6.25	13.9	9	2.1	95.0
6.75	15.0	6	1.4	96.5
7.25	16.1	5	1.2	97.6
7.75	17.2	4	0.9	98.6
8.25	18.3	1	0.2	98.8
8.75	19.4	1	0.2	99.1
9.25	20.6	1	0.2	99.3
9.75	21.7	2	0.5	99.8
12.25	27.2	1	0.2	100.0

Tables 10 and 11. The data of calibration slides Cal. IIA and IIB respectively.

PRINT MEASURED DROPLET DIAMETER (MM)	MAGNIFICATION CORRECTED DROPLET DIAMETER (μM)	DROPLET NUMBER	PERCENTAGE OF TOTAL NUMBER	CUMULATIVE PERCENTAGE
1.25	4.7	94	14.4	14.4
1.75	6.6	120	18.4	32.8
2.25	8.5	131	20.1	52.9
2.75	10.4	72	11.0	64.0
3.25	12.3	95	14.6	78.5
3.75	14.2	67	10.3	88.8
4.25	16.0	31	4.8	93.6
4.75	17.9	6	0.9	94.5
5.25	19.8	12	1.8	96.3
5.75	21.7	11	1.7	98.0
6.25	23.6	9	1.4	99.4
7.25	27.4	2	0.3	99.7
7.75	29.2	1	0.2	99.8
8.25	31.1	1	0.2	100.0

PRINT MEASURED DROPLET DIAMETER (MM)	MAGNIFICATION CORRECTED DROPLET DIAMETER (μM)	DROPLET NUMBER	PERCENTAGE OF TOTAL NUMBER	CUMULATIVE PERCENTAGE
2.25	8.5	60	14.9	14.9
2.75	10.4	25	6.2	21.0
3.25	12.3	44	10.9	31.9
3.75	14.2	51	12.6	44.6
4.25	16.0	79	19.6	64.1
4.75	17.9	47	11.6	75.7
5.25	19.8	39	9.7	85.4
5.75	21.7	17	4.2	89.6
6.25	23.6	18	4.5	94.1
6.75	25.5	7	1.7	95.8
7.25	27.4	8	2.0	97.8
7.75	29.2	5	1.2	99.0
8.75	33.0	1	0.2	99.3
9.25	34.9	1	0.2	99.5
10.25	38.7	1	0.2	99.8
11.25	42.5	1	0.2	100.0

Tables 12 and 13. The data of calibration slides Cal. IIC and IIIA respectively.

PRINT MEASURED DROPLET DIAMETER (MM)	MAGNIFICATION CORRECTED DROPLET DIAMETER (μM)	DROPLET NUMBER	PERCENTAGE OF TOTAL NUMBER	CUMULATIVE PERCENTAGE
2.50	5.6	14	4.7	4.7
3.50	7.8	39	13.1	17.8
4.50	10.0	61	20.5	38.4
5.50	12.2	57	19.2	57.6
6.50	14.4	44	14.8	72.4
7.50	16.7	33	11.1	83.5
8.50	18.9	19	6.4	89.9
9.50	21.1	7	2.4	92.3
10.50	23.3	7	2.4	94.6
11.50	25.6	8	2.7	97.3
12.50	27.8	5	1.7	99.0
13.50	30.0	1	0.3	99.3
14.50	32.2	1	0.3	99.7
18.50	41.1	1	0.3	100.0

PRINT MEASURED DROPLET DIAMETER (MM)	MAGNIFICATION CORRECTED DROPLET DIAMETER (μM)	DROPLET NUMBER	PERCENTAGE OF TOTAL NUMBER	CUMULATIVE PERCENTAGE
1.25	2.8	57	7.7	7.7
1.75	3.9	53	7.2	14.8
2.25	5.0	75	10.1	25.0
2.75	6.1	80	10.8	35.8
3.25	7.2	117	15.8	51.6
3.75	8.3	66	8.9	60.5
4.25	9.4	106	14.3	74.8
4.75	10.6	49	6.6	81.4
5.25	11.7	29	3.9	85.3
5.75	12.8	21	2.8	88.1
6.25	13.9	20	2.7	90.8
6.75	15.0	14	1.9	92.7
7.25	16.1	11	1.5	94.2
7.75	17.2	9	1.2	95.4
8.25	18.3	13	1.8	97.2
8.75	19.4	5	0.7	97.8
9.25	20.6	2	0.3	98.1
9.75	21.7	2	0.3	98.4
10.25	22.8	4	0.5	98.9
10.75	23.9	2	0.3	99.2
11.25	25.0	3	0.4	99.6
11.75	26.1	1	0.1	99.7
12.75	28.3	1	0.1	99.9
14.25	31.7	1	0.1	100.0

Table 14. The data of calibration slide Cal. IIIB.

PRINT MEASURED DROPLET DIAMETER (MM)	MAGNIFICATION CORRECTED DROPLET DIAMETER (μM)	DROPLET NUMBER	PERCENTAGE OF TOTAL NUMBER	CUMULATIVE PERCENTAGE
2.50	5.6	2	0.6	0.6
3.50	7.8	13	3.7	4.3
4.50	10.0	38	10.8	15.1
5.50	12.2	59	16.8	31.9
6.50	14.4	70	19.9	51.9
7.50	16.7	62	17.7	69.5
8.50	18.9	34	9.7	79.2
9.50	21.1	25	7.1	86.3
10.50	23.3	16	4.6	90.9
11.50	25.6	16	4.6	95.4
12.50	27.8	8	2.3	97.7
13.50	30.0	3	0.9	98.6
14.50	32.2	2	0.6	99.1
15.50	34.4	2	0.6	99.7
16.50	36.7	1	0.3	100.0

Table 15. A further analysis of calibration slide CAL. IIIA. Column 5 gives the sum of the droplets' terminal velocity and the air velocity within the cloud chamber.

PRINT MEASURED DROPLET DIAMETER (MM)	MAGNIFICATION CORRECTED DROPLET DIAMETER (μM)	TRUE DROPLET DIAMETER (μM)	DROPLET NUMBER ON ANALYZED SLIDE AREA	DROPLET TERMINAL PLUS AIR VELOCITY (CM S^{-1})	DROPLET NUMBER CONCENTRATION (NUMBER CM^{-3} (SIZE CATEGORY)$^{-1}$)	PERCENTAGE OF TOTAL DROPLETS	CUMULATIVE PERCENTAGE OF TOTAL DROPLETS	DROPLET MASS CONCENTRATION (10^{-7} G CM^{-3} (SIZE CATEGORY)$^{-1}$)	PERCENTAGE OF TOTAL DROPLET MASS	CUMULATIVE PERCENTAGE OF DROPLET MASS
1.00	2.2	2.2	57	0.21	958.2	13.1	13.1	6.	0.3	0.3
1.50	3.3	3.3	53	0.23	813.3	11.1	24.2	16.	0.8	1.1
2.00	4.4	4.4	75	0.25	1025.8	14.0	38.2	47.	2.5	3.6
2.50	5.6	5.6	80	0.29	960.0	13.1	51.3	86.	4.5	8.1
3.00	6.7	6.7	117	0.33	1221.0	16.7	68.0	189.	10.0	18.1
3.50	7.8	7.8	66	0.38	596.8	8.2	76.2	147.	7.7	25.8
4.00	8.9	8.9	106	0.44	830.6	11.4	87.5	305.	16.1	41.9
4.50	10.0	10.0	49	0.51	333.5	4.6	92.1	175.	9.2	51.1
5.00	11.1	11.1	29	0.58	172.1	2.4	94.5	124.	6.5	57.6
5.50	12.2	12.2	21	0.67	109.2	1.5	95.9	104.	5.5	63.1
6.00	13.3	13.3	20	0.76	91.6	1.3	97.2	114.	6.0	69.1
6.50	14.4	14.4	14	0.85	56.7	0.8	98.0	90.	4.7	73.8
7.00	15.6	15.6	11	0.96	39.6	0.5	98.5	78.	4.1	77.9
7.50	16.7	16.7	9	1.07	29.0	0.4	98.9	70.	3.7	81.6
8.00	17.8	17.8	13	1.20	37.6	0.5	99.4	111.	5.8	87.4
8.50	18.9	18.9	5	1.32	13.1	0.2	99.6	46.	2.4	89.9
9.00	20.0	20.0	2	1.46	4.7	0.1	99.7	20.	1.0	90.9
9.50	21.1	21.1	2	1.61	4.3	0.1	99.7	21.	1.1	92.0
10.00	22.2	22.2	4	1.76	7.9	0.1	99.8	45.	2.4	94.4
10.50	23.3	23.3	2	1.92	3.6	0.0	99.9	24.	1.3	95.7
11.00	24.4	24.4	3	2.09	5.0	0.1	99.9	38.	2.0	97.6
11.50	25.6	25.6	1	2.27	1.5	0.0	100.0	13.	0.7	98.3
12.50	27.8	27.8	1	2.64	1.3	0.0	100.0	15.	0.8	99.1
14.00	31.1	31.1	1	3.27	1.1	0.0	100.0	17.	0.9	100.0

COLLECTION PERIOD= 120. S
CLOUD DROPLET WATER CONTENT= 1.53 G KG^{-1}
MASS OF DROPLETS ON SLIDE= 3.20×10^{-5} G
AREA OF SLIDE ANALYZED= 2.41×10^{-3} CM^{2}

Tables 16 and 17. A further analysis of calibration slide CAL. IIB, and the analyzed data from Slide 21 for SEQ. II, respectively.

PRINT MEASURED DROPLET DIAMETER (MM)	MAGNIFICATION CORRECTED DROPLET DIAMETER (μM)	TRUE DROPLET DIAMETER (μM)	DROPLET NUMBER ON ANALYZED SLIDE AREA	DROPLET TERMINAL PLUS AIR VELOCITY (CM S^{-1})	DROPLET NUMBER CONCENTRATION (NUMBER CM^{-3} (SIZE CATEGORY)$^{-1}$)	PERCENTAGE OF TOTAL DROPLETS	CUMULATIVE PERCENTAGE OF TOTAL DROPLETS	DROPLET MASS CONCENTRATION (10^{-9} G CM^{-3} (SIZE CATEGORY)$^{-1}$)	PERCENTAGE OF TOTAL DROPLET MASS	CUMULATIVE PERCENTAGE OF DROPLET MASS
2.50	5.6	3.4	2	0.23	18.5	1.2	1.2	0.	0.0	0.0
3.50	7.8	4.7	13	0.26	104.3	6.5	7.7	6.	0.8	0.8
4.50	10.0	6.1	36	0.31	258.8	16.2	23.9	31.	4.0	4.9
5.50	12.2	7.5	59	0.37	337.8	21.1	45.0	73.	9.6	14.5
6.50	14.4	8.8	70	0.44	336.5	21.0	66.0	120.	15.8	30.3
7.50	16.7	10.2	62	0.52	251.0	15.7	81.7	138.	18.2	48.5
8.50	18.9	11.5	34	0.61	116.6	7.3	89.0	93.	12.3	60.8
9.50	21.1	12.9	25	0.72	73.2	4.6	93.6	82.	10.8	71.5
10.50	23.3	14.2	16	0.83	40.3	2.5	96.1	61.	8.0	79.5
11.50	25.6	15.6	16	0.96	34.9	2.2	98.3	69.	9.1	88.6
12.50	27.8	16.9	8	1.10	15.2	1.0	99.3	39.	5.1	93.7
13.50	30.0	18.3	3	1.25	5.0	0.3	99.6	16.	2.1	95.9
14.50	32.2	19.6	2	1.42	3.0	0.2	99.8	12.	1.5	97.4
15.50	34.4	21.0	2	1.59	2.6	0.2	99.9	13.	1.7	99.1
16.50	36.7	22.4	1	1.78	1.2	0.1	100.0	7.	0.9	100.0

COLLECTION PERIOD= 120. S
CLOUD DROPLET WATER CONTENT= 0.61 G KG^{-1}
MASS OF DROPLETS ON SLIDE= 1.14×10^{-5} G
AREA OF SLIDE ANALYZED= 3.97×10^{-2} CM^2

PRINT MEASURED DROPLET DIAMETER (MM)	MAGNIFICATION CORRECTED DROPLET DIAMETER (μM)	TRUE DROPLET DIAMETER (μM)	DROPLET NUMBER ON ANALYZED SLIDE AREA	DROPLET TERMINAL PLUS AIR VELOCITY (CM S^{-1})	DROPLET NUMBER CONCENTRATION (NUMBER CM^{-3} (SIZE CATEGORY)$^{-1}$)	PERCENTAGE OF TOTAL DROPLETS	CUMULATIVE PERCENTAGE OF TOTAL DROPLETS	DROPLET MASS CONCENTRATION (10^{-9} G CM^{-3} (SIZE CATEGORY)$^{-1}$)	PERCENTAGE OF TOTAL DROPLET MASS	CUMULATIVE PERCENTAGE OF DROPLET MASS
2.50	5.6	3.4	37	0.23	471.5	31.8	31.8	10.	1.3	1.3
3.50	7.8	4.7	4	0.26	44.1	3.0	34.8	2.	0.3	1.7
4.50	10.0	6.1	8	0.31	74.9	5.0	39.8	9.	1.2	2.9
5.50	12.2	7.5	13	0.37	102.3	6.9	46.7	22.	3.1	6.0
6.50	14.4	8.8	29	0.44	191.7	12.9	59.6	69.	9.6	15.6
7.50	16.7	10.2	39	0.52	217.1	14.6	74.3	119.	16.6	32.2
8.50	18.9	11.5	40	0.61	188.7	12.7	87.0	151.	21.0	53.2
9.50	21.1	12.9	21	0.72	84.5	5.7	92.7	94.	13.2	66.4
10.50	23.3	14.2	11	0.83	38.1	2.6	95.2	57.	8.0	74.4
11.50	25.6	15.6	10	0.96	30.0	2.0	97.3	59.	8.3	82.7
12.50	27.8	16.9	11	1.10	28.8	1.9	99.2	73.	10.2	92.9
13.50	30.0	18.3	3	1.25	6.9	0.5	99.7	22.	3.1	95.9
14.50	32.2	19.6	1	1.42	2.0	0.1	99.8	8.	1.1	97.1
15.50	34.4	21.0	1	1.59	1.8	0.1	99.9	9.	1.2	98.3
20.50	45.6	27.8	1	2.64	1.1	0.1	100.0	12.	1.7	100.0

COLLECTION PERIOD= 90. S
CLOUD DROPLET WATER CONTENT= 0.58 G KG^{-1}
MASS OF DROPLETS ON SLIDE= 0.91×10^{-5} G
AREA OF SLIDE ANALYZED= 3.85×10^{-2} CM^2

Tables 18 and 19. The analyzed data from Slide 19, SEQ. II ; and Slide 23, SEQ. VI, respectively.

PRINT MEASURED DROPLET DIAMETER (MM)	MAGNIFICATION CORRECTED DROPLET DIAMETER (μM)	TRUE DROPLET DIAMETER (μM)	DROPLET NUMBER ON ANALYZED SLIDE AREA	DROPLET TERMINAL PLUS AIR VELOCITY (CM S^{-1})	DROPLET NUMBER CONCENTRATION (NUMBER CM^{-3} (SIZE CATEGORY)$^{-1}$)	PERCENTAGE OF TOTAL DROPLETS	CUMULATIVE PERCENTAGE OF TOTAL DROPLETS	DROPLET MASS CONCENTRATION (10^{-9} G CM^{-3} (SIZE CATEGORY)$^{-1}$)	PERCENTAGE OF TOTAL DROPLET MASS	CUMULATIVE PERCENTAGE OF DROPLET MASS
2.50	5.6	3.4	13	0.23	166.9	7.8	7.8	3.	0.5	0.5
3.50	7.8	4.7	31	0.26	344.8	16.0	23.8	19.	3.1	3.6
4.50	10.0	6.1	41	0.31	386.9	18.0	41.8	46.	7.3	10.9
5.50	12.2	7.5	60	0.37	476.0	22.2	64.0	103.	16.4	27.3
6.50	14.4	8.8	61	0.44	406.3	18.9	82.9	145.	23.1	50.3
7.50	16.7	10.2	33	0.52	185.1	8.6	91.5	102.	16.2	66.5
8.50	18.9	11.5	20	0.61	95.1	4.4	95.9	76.	12.1	78.6
9.50	21.1	12.9	10	0.72	40.6	1.9	97.8	45.	7.2	85.8
10.50	23.3	14.2	8	0.83	27.9	1.3	99.1	42.	6.7	92.4
11.50	25.6	15.6	4	0.96	12.1	0.6	99.7	24.	3.8	96.2
12.50	27.8	16.9	1	1.10	2.6	0.1	99.8	7.	1.1	97.3
13.50	30.0	18.3	1	1.25	2.3	0.1	99.9	7.	1.2	98.5
16.50	36.7	22.4	1	1.78	1.6	0.1	100.0	10.	1.5	100.0

COLLECTION PERIOD= 90. S
CLOUD DROPLET WATER CONTENT= 0.51 G KG^{-1}
MASS OF DROPLETS ON SLIDE= 0.18×10^{-3} G
AREA OF SLIDE ANALYZED= 3.82×10^{-5} CM^{2}

PRINT MEASURED DROPLET DIAMETER (MM)	MAGNIFICATION CORRECTED DROPLET DIAMETER (μM)	TRUE DROPLET DIAMETER (μM)	DROPLET NUMBER ON ANALYZED SLIDE AREA	DROPLET TERMINAL PLUS AIR VELOCITY (CM S^{-1})	DROPLET NUMBER CONCENTRATION (NUMBER CM^{-3} (SIZE CATEGORY)$^{-1}$)	PERCENTAGE OF TOTAL DROPLETS	CUMULATIVE PERCENTAGE OF TOTAL DROPLETS	DROPLET MASS CONCENTRATION (10^{-9} G CM^{-3} (SIZE CATEGORY)$^{-1}$)	PERCENTAGE OF TOTAL DROPLET MASS	CUMULATIVE PERCENTAGE OF DROPLET MASS
1.50	3.3	2.0	36	0.20	511.0	15.4	15.4	2.	0.4	0.4
2.50	5.6	3.4	51	0.23	649.3	19.5	34.9	13.	2.6	3.0
3.50	7.8	4.7	61	0.26	672.6	20.2	55.1	38.	7.3	10.2
4.50	10.0	6.1	72	0.31	673.6	20.3	75.4	80.	15.4	25.7
5.50	12.2	7.5	47	0.37	369.7	11.1	86.5	80.	15.5	41.1
6.50	14.4	8.8	32	0.44	211.3	6.4	92.9	76.	14.6	55.7
7.50	16.7	10.2	20	0.52	111.2	3.3	96.2	61.	11.8	67.5
8.50	18.9	11.5	14	0.61	66.0	2.0	98.2	53.	10.2	77.7
9.50	21.1	12.9	5	0.72	20.1	0.6	98.8	22.	4.3	82.1
10.50	23.3	14.2	6	0.83	20.8	0.6	99.4	31.	6.0	88.1
11.50	25.6	15.6	3	0.96	9.0	0.3	99.7	18.	3.4	91.5
12.50	27.8	16.9	2	1.10	5.2	0.2	99.9	13.	2.6	94.1
14.50	32.2	19.6	1	1.42	2.0	0.1	99.9	8.	1.6	95.7
15.50	34.4	21.0	1	1.59	1.8	0.1	100.0	9.	1.7	97.4
22.50	50.0	30.5	1	3.15	0.9	0.0	100.0	14.	2.6	100.0

COLLECTION PERIOD= 120. S
CLOUD DROPLET WATER CONTENT= 0.42 G KG^{-1}
MASS OF DROPLETS ON SLIDE= 0.69×10^{-3} G
AREA OF SLIDE ANALYZED= 2.89×10^{-5} M^{2}

Tables 20 and 21. The analyzed data from Slide 27, SEQ. XII; and Slide 25, SEQ. XI, respectively.

PRINT MEASURED DROPLET DIAMETER (MM)	MAGNIFICATION CORRECTED DROPLET DIAMETER (μM)	TRUE DROPLET DIAMETER (μM)	DROPLET NUMBER ON ANALYZED SLIDE AREA	DROPLET TERMINAL PLUS AIR VELOCITY (CM S^{-1})	DROPLET NUMBER CONCENTRATION (NUMBER CM^{-3} (SIZE CATEGORY)$^{-1}$)	PERCENTAGE OF TOTAL DROPLETS	CUMULATIVE PERCENTAGE OF TOTAL DROPLETS	DROPLET MASS CONCENTRATION (10^{-9} G CM^{-3} (SIZE CATEGORY)$^{-1}$)	PERCENTAGE OF TOTAL DROPLET MASS	CUMULATIVE PERCENTAGE OF DROPLET MASS
2.50	5.6	3.4	63	0.23	796.6	18.6	18.6	16.	2.2	2.2
3.50	7.8	4.7	119	0.26	1303.1	30.5	49.1	73.	10.0	12.2
4.50	10.0	6.1	98	0.31	910.5	21.3	70.4	108.	14.8	27.0
5.50	12.2	7.5	87	0.37	679.6	15.9	86.3	147.	20.2	47.1
6.50	14.4	8.8	45	0.44	295.1	6.9	93.2	106.	14.5	61.6
7.50	16.7	10.2	16	0.52	88.4	2.1	95.2	49.	6.7	68.3
8.50	18.9	11.5	21	0.61	98.3	2.3	97.5	79.	10.8	79.0
9.50	21.1	12.9	7	0.72	28.0	0.7	98.2	31.	4.3	83.3
10.50	23.3	14.2	21	0.83	72.1	1.7	99.9	109.	14.9	98.2
11.50	25.6	15.6	1	0.96	3.0	0.1	99.9	6.	0.8	99.0
13.50	30.0	18.3	1	1.25	2.3	0.1	100.0	7.	1.0	100.0

COLLECTION PERIOD= 90. S
CLOUD DROPLET WATER CONTENT= 0.59 G KG^{-1}
MASS OF DROPLETS ON SLIDE= 0.60×10^{-3} G
AREA OF SLIDE ANALYZED= 3.88×10^{-2} CM^2

PRINT MEASURED DROPLET DIAMETER (MM)	MAGNIFICATION CORRECTED DROPLET DIAMETER (μM)	TRUE DROPLET DIAMETER (μM)	DROPLET NUMBER ON ANALYZED SLIDE AREA	DROPLET TERMINAL PLUS AIR VELOCITY (CM S^{-1})	DROPLET NUMBER CONCENTRATION (NUMBER CM^{-3} (SIZE CATEGORY)$^{-1}$)	PERCENTAGE OF TOTAL DROPLETS	CUMULATIVE PERCENTAGE OF TOTAL DROPLETS	DROPLET MASS CONCENTRATION (10^{-9} G CM^{-3} (SIZE CATEGORY)$^{-1}$)	PERCENTAGE OF TOTAL DROPLET MASS	CUMULATIVE PERCENTAGE OF DROPLET MASS
1.50	3.3	2.0	15	0.20	156.6	7.6	7.6	1.	0.2	0.2
2.50	5.6	3.4	24	0.23	224.7	11.0	18.6	5.	1.2	1.4
3.50	7.8	4.7	56	0.26	454.0	22.1	40.7	25.	6.9	8.3
4.50	10.0	6.1	77	0.31	529.7	25.8	66.6	63.	17.0	25.3
5.50	12.2	7.5	58	0.37	335.5	16.4	82.9	73.	19.6	44.9
6.50	14.4	8.8	36	0.44	174.8	8.5	91.4	63.	16.9	61.8
7.50	16.7	10.2	23	0.52	94.1	4.6	96.0	52.	14.0	75.8
8.50	18.9	11.5	13	0.61	45.1	2.2	98.2	36.	9.7	85.5
9.50	21.1	12.9	7	0.72	20.7	1.0	99.2	23.	6.2	91.7
10.50	23.3	14.2	4	0.83	10.2	0.5	99.7	15.	4.1	95.9
11.50	25.6	15.6	1	0.96	2.2	0.1	99.8	4.	1.2	97.1
12.50	27.8	16.9	1	1.10	1.9	0.1	99.9	5.	1.3	98.4
14.50	32.2	19.6	1	1.42	1.5	0.1	100.0	6.	1.6	100.0

COLLECTION PERIOD= 120. S
CLOUD DROPLET WATER CONTENT= 0.30 G KG^{-1}
MASS OF DROPLETS ON SLIDE= 0.40×10^{-3} G
AREA OF SLIDE ANALYZED= 3.93×10^{-3} CM^2

APPENDIX D

DATA ON THE CHARACTERISTICS OF THE PROLONGED GROWTH DEPOSITS

Tables 22 and 23. The rate of growth of the maximum length of the deposit during prolonged growth periods.

SEQUENCE NUMBER I

FILM 10 FILMSTRIP NUMBER	FRAME NUMBER	TIME (MM:SS)	MAXIMUM LENGTH (MM)	MAXIMUM WIDTH (MM)
0A		1:00	0.5	1.4
1A		2:01	0.8	1.6
2A		3:02	1.1	1.7
3A		4:02	1.6	1.7
4A		5:03	2.0	1.8
5A		6:05	2.5	1.8
6A		7:05	3.0	1.9
7A		8:06	3.5	2.0
8A		9:06	3.9	2.0
9A		10:06	4.4	2.1
10A		11:07	4.8	2.1
11A		12:07	5.3	2.3
12A		13:09	5.8	2.4
13A		14:10	6.4	2.5
14A		14:14	6.6	2.5
15A		14:14	6.6	2.9

SEQUENCE NUMBER II

FILM 10 FILMSTRIP NUMBER	FRAME NUMBER	TIME (MM:SS)	MAXIMUM LENGTH (MM)	MAXIMUM WIDTH (MM)
17A		2:11	0.0	0.0
18A		3:10	0.0	0.0
19A		4:10	0.0	0.0
20A	23(1,1)	5:10	0.1	0.0
21A	23(1,2)	6:09	0.1	1.0
22A	23(1,3)	7:07	0.2	1.2
23A	23(1,4)	8:07	0.3	1.2
24A	23(1,5)	9:06	0.3	1.5
25A	23(2,1)	10:06	0.4	1.6
26A	23(2,2)	11:06	0.4	1.7
27A	23(2,3)	13:05	0.6	2.0
28A	23(2,4)	15:07	0.8	2.2
29A	23(2,5)	17:11	0.9	2.4
30A	23(3,1)	19:14	0.9	2.7
31A	23(3,2)	21:17	1.0	2.9
32A	23(3,3)	23:21	1.1	3.1
33A	23(3,4)	25:25	1.2	3.4
34A	23(3,5)	25:25	1.2	3.4

Tables 24 and 25. As in Tables 22 and 23.

SEQUENCE NUMBER III

FILM 11 FILMSTRIP NUMBER	FRAME NUMBER	TIME (MM:SS)	MAXIMUM LENGTH (MM)	MAXIMUM WIDTH (MM)
1A		0:19	0.1	1.2
2A		1:19	0.6	0.9
3A		2:19	0.9	1.5
4A		3:19	1.4	1.7
5A		4:19	1.9	1.9
6A		5:19	2.4	1.9
7A		6:19	2.9	1.9
8A		7:19	3.5	2.1
9A		7:48	3.6	2.1
10A		8:19	3.9	2.2
11A		9:21	4.5	2.4
12A		10:22	5.1	2.6
13A		11:22	5.6	2.7
14A		12:23	6.3	2.9
15A		13:25	6.9	3.0
16A		13:39	7.0	3.0
18A		13:39	7.1	3.3

SEQUENCE NUMBER IV

FILM 11 FILMSTRIP NUMBER	FRAME NUMBER	TIME (MM:SS)	MAXIMUM LENGTH (MM)	MAXIMUM WIDTH (MM)
19A		0:05	0.0	0.0
20A		1:02	0.1	0.1
21A		2:03	0.3	0.1
22A		3:05	0.4	0.0
23A		3:39	0.5	0.0
24A		4:05	0.6	0.0
25A		4:44	0.6	0.0
26A		5:05	0.8	1.4
27A		6:05	1.1	1.4
28A		7:05	1.3	1.4
29A		8:05	1.4	1.5
30A		9:05	1.6	1.6
31A		10:05	1.9	1.7
32A		11:05	2.1	1.9
33A		12:05	2.2	2.0
35A		13:05	2.4	2.1
36A		13:05	2.8	2.8

Tables 26 and 27. As in Tables 22 and 23.

SEQUENCE NUMBER V

FILM 12 FILMSTRIP NUMBER	FRAME NUMBER	TIME (MM:SS)	MAXIMUM LENGTH (MM)	MAXIMUM WIDTH (MM)
0A		0:19	0.0	0.0
1A		1:19	0.1	0.1
2A		2:19	0.3	0.7
3A		3:19	0.5	1.2
4A		4:19	0.7	1.3
5A		5:19	0.9	1.4
6A		6:19	1.1	1.5
7A		6:30	1.1	1.5
8A		6:55	1.3	1.6
10A		7:47	1.4	1.7
11A		8:19	1.6	1.7
12A		9:19	1.8	1.9
13A		9:44	1.8	1.9
14A		10:19	1.9	1.9
15A		10:35	1.9	2.0
16A		11:19	2.1	2.2
17A		11:25	2.1	2.2
18A		12:19	2.2	2.3
19A		12:30	2.3	2.3
20A		13:19	2.4	2.5

SEQUENCE NUMBER VI

FILM 12 FILMSTRIP NUMBER	FRAME NUMBER	TIME (MM:SS)	MAXIMUM LENGTH (MM)	MAXIMUM WIDTH (MM)
22A		0:35	0.1	1.3
24A		1:35	0.6	1.5
25A		2:39	1.1	1.8
26A		3:39	1.4	2.1
27A		4:39	1.9	2.3
28A		5:39	2.4	2.4
29A		5:44	2.5	2.4
30A		6:42	3.1	2.5
31A		7:43	3.6	2.7
32A		8:46	4.2	2.8
33A		9:47	4.7	2.8
34A		10:48	5.3	2.9
35A		11:50	5.9	3.0

Tables 28 and 29. As in Tables 22 and 23.

SEQUENCE NUMBER VII

FILM 13 FILMSTRIP NUMBER	FRAME NUMBER	TIME (MM:SS)	MAXIMUM LENGTH (MM)	MAXIMUM WIDTH (MM)
1	28(1,1)	1:05	0.4	1.4
2	28(1,2)	2:06	0.8	1.5
3	28(1,3)	3:06	1.3	1.7
4	28(1,4)	4:06	1.7	1.9
5	28(1,5)	5:07	2.1	2.0
6	28(2,1)	6:07	2.6	2.1
7	28(2,2)	7:09	3.4	2.2
8	28(2,3)	8:09	3.9	2.3
9	28(2,4)	9:10	4.4	2.4
10	28(2,5)	10:10	5.0	2.5
11	28(3,1)	11:11	5.6	2.6
12	28(3,2)	12:13	6.3	2.7
13	28(3,3)	13:13	6.8	2.9
14	28(3,4)	14:14	7.4	3.1
15	28(3,5)	15:14	8.1	3.2
16	28(4,5)	15:14	0.0	0.0

SEQUENCE NUMBERVIII

FILM 13 FILMSTRIP NUMBER	FRAME NUMBER	TIME (MM:SS)	MAXIMUM LENGTH (MM)	MAXIMUM WIDTH (MM)
17	25(1,1)	1:35	0.2	0.3
18	25(1,2)	0:00	0.2	0.3
19	25(1,3)	2:35	0.4	1.2
20	25(1,4)	3:38	0.5	1.4
21	25(2,1)	4:39	0.6	1.4
22	25(2,2)	5:40	0.8	1.5
23	25(2,3)	6:43	0.9	1.6
24	25(2,4)	7:44	1.1	1.7
25	25(2,5)	7:47	1.1	1.7
26	25(3,1)	8:47	1.3	1.7
27	25(3,2)	9:47	1.4	1.8
28	25(3,3)	10:48	1.6	1.9
29	25(3,4)	11:50	1.8	1.9
30	25(3,5)	12:51	1.9	2.0
31	26(1,1)	14:52	2.1	2.2
32	26(1,2)	15:53	2.2	2.5
33	26(1,3)	16:35	2.3	3.3
34	26(1,4)	16:55	2.4	3.4
35	26(1,5)	17:58	2.5	3.4
36	26(2,1)	19:00	2.6	3.6
36A	26(2,2)	19:05	2.8	3.0

Tables 30 and 31. As in Tables 22 and 23.

SEQUENCE NUMBER IX

FILM 14 FILMSTRIP NUMBER	FRAME NUMBER	TIME (MM:SS)	MAXIMUM LENGTH (MM)	MAXIMUM WIDTH (MM)
1A		0:35	0.2	0.3
2A		1:36	0.3	0.7
3A		2:39	0.4	1.2
4A		3:40	0.6	1.3
5A		4:43	0.9	1.4
6A		5:44	1.2	1.5
7A		6:44	1.3	1.6
8A		7:46	1.5	1.8
9A		8:47	1.8	1.9
10A		9:47	2.1	1.9
12A		11:47	2.4	2.4
13A		12:48	2.5	3.0
14A		13:50	2.6	3.3
15A		14:50	2.6	3.8
16A		15:51	2.8	4.3
17A		16:52	3.0	4.6
18A		17:00	3.2	2.6

SEQUENCE NUMBER X

FILM 14 FILMSTRIP NUMBER	FRAME NUMBER	TIME (MM:SS)	MAXIMUM LENGTH (MM)	MAXIMUM WIDTH (MM)
19A		1:14	0.0	0.0
20A		2:15	0.0	0.0
21A		3:17	0.0	0.0
22A		4:18	0.0	0.0
23A		5:18	0.0	0.0
24A		6:19	0.1	0.0
26A	29(1,1)	8:22	0.3	0.0
27A	29(1,2)	9:22	0.5	0.4
28A		10:23	0.8	0.5
29A	29(1,3)	11:25	1.0	0.5
30A	30(1,4)	12:26	1.3	0.7
31A	30(1,5)	13:27	0.6	1.1
32A	30(2,1)	14:27	0.9	1.3
33A	30(2,2)	15:28	0.6	1.2
34A	30(2,3)	16:30	0.7	1.1
35A	30(2,4)	17:30	0.8	1.2
36A	30(3,1)	17:44	0.8	1.4

Tables 32 and 33. As in Tables 22 and 23.

SEQUENCE NUMBER XI

FILM 15 FILMSTRIP NUMBER	FRAME NUMBER	TIME (MM:SS)	MAXIMUM LENGTH (MM)	MAXIMUM WIDTH (MM)
1	31(1,1)	0:37	0.4	0.5
2	31(1,2)	1:10	0.6	0.6
3	31(1,3)	1:42	0.9	0.8
4	31(1,4)	2:14	1.1	1.0
5	31(1,5)	2:47	0.4	0.8
6	31(2,1)	3:19	0.6	0.9
7	31(2,2)	3:52	0.9	1.0
8	31(2,3)	4:25	1.1	1.1
9	31(2,4)	4:56	1.4	1.3
10	31(2,5)	5:30	1.7	1.4
11	31(3,1)	6:02	1.9	1.6
12	31(3,2)	6:34	2.3	1.5
13	31(3,3)	7:05	0.1	0.2
14	31(3,4)	7:36	0.5	0.7
15	31(3,5)	8:10	0.8	1.0
16		8:42	1.1	1.2
17		9:14	1.4	1.3
18		9:30	1.6	1.4

SEQUENCE NUMBER XII

FILM 15 FILMSTRIP NUMBER	FRAME NUMBER	TIME (MM:SS)	MAXIMUM LENGTH (MM)	MAXIMUM WIDTH (MM)
19		0:33	0.4	1.3
20		1:06	0.7	1.5
21		1:38	1.0	1.7
22		2:10	1.4	1.9
23		2:42	1.7	2.0
24		3:14	2.1	2.1
25		3:44	2.6	2.2
26		4:15	3.0	2.4
27		4:47	3.4	2.4
28		5:18	3.6	2.5
29		5:48	4.1	2.5
30		6:19	4.5	2.5
31		6:51	4.9	2.6
32		7:22	5.4	2.7
33		7:52	5.9	2.9
34		8:23	6.4	3.0
35		8:55	6.9	3.0
36		9:10	7.2	3.7

Tables 34 and 35. The dimensions of the deposit as used for estimating its volume.

SEQUENCE NUMBER I

FILM 10

DISTANCE FROM SUBSTRATE (MM)	MEAN SIDE WIDTH (MM)	MEAN TOP/ BOTTOM WIDTH (MM)
0.1	1.5	1.6
0.2	1.6	1.6
0.3	1.5	1.7
0.4	1.4	1.7
0.5	1.5	1.8
0.6	1.6	1.8
0.7	1.7	1.9
0.8	1.9	1.8
0.9	1.9	1.9
1.0	1.8	1.9
1.1	1.9	1.9
1.2	1.9	2.0
1.3	1.7	2.0
1.4	1.8	2.0
1.5	1.9	2.0
1.6	1.9	2.1
1.7	1.9	2.1
1.8	1.9	2.2
1.9	1.9	2.2
2.0	1.9	2.4
2.2	1.9	2.3
2.4	1.9	2.3
2.6	2.0	2.3
2.8	2.2	2.2
3.0	2.0	2.4
3.2	2.1	2.4
3.4	2.0	2.3
3.6	1.9	2.3
3.8	2.0	2.4
4.0	2.1	2.5
4.2	2.0	2.4
4.4	2.1	2.6
4.6	2.2	2.7
4.8	2.2	2.7
5.0	2.4	2.6
5.2	2.4	2.6
5.4	2.4	2.7
5.6	2.4	2.8
5.8	2.4	2.8
6.0	2.4	2.6
6.2	2.3	2.3
6.4	0.7	1.2
6.6	0.2	0.3

TOTAL GROWTH VOLUME 0.30E-01 CM^3

SEQUENCE NUMBER II

FILM 10

DISTANCE FROM SUBSTRATE (MM)	MEAN SIDE WIDTH (MM)	MEAN TOP/ BOTTOM WIDTH (MM)
0.1	2.6	3.2
0.2	2.8	3.3
0.3	2.8	3.1
0.4	2.3	3.1
0.5	2.5	2.7
0.6	2.8	1.4
0.7	2.8	1.4
0.8	2.6	1.0
0.9	1.7	1.0
1.0	1.5	1.1
1.1	0.9	0.8
1.2	0.5	0.4
1.3	0.3	0.1

TOTAL GROWTH VOLUME 0.55E-02 CM^3

Tables 36 and 37. As in Tables 34 and 35.

SEQUENCE NUMBER III

FILM 11

DISTANCE FROM SUBSTRATE (MM)	MEAN SIDE WIDTH (MM)	MEAN TOP/ BOTTOM WIDTH (MM)
0.1	1.2	1.3
0.2	1.2	1.3
0.3	1.3	1.4
0.4	1.3	1.4
0.5	1.4	1.5
0.6	1.4	1.6
0.7	1.5	1.7
0.8	1.5	1.7
0.9	1.6	1.8
1.0	1.7	1.8
1.1	1.7	1.9
1.2	1.8	1.9
1.3	1.8	2.0
1.4	1.8	2.0
1.5	1.8	2.0
1.6	1.9	2.1
1.7	1.9	2.1
1.8	1.9	2.1
1.9	1.9	2.1
2.0	2.0	2.2
2.2	1.9	2.2
2.4	2.0	2.3
2.6	2.0	2.4
2.8	2.1	2.4
3.0	2.1	2.5
3.2	2.1	2.6
3.4	2.2	2.6
3.6	2.2	2.7
3.8	2.2	2.7
4.0	2.3	2.8
4.2	2.4	2.9
4.4	2.4	2.9
4.6	2.5	2.9
4.8	2.7	3.0
5.0	2.7	3.0
5.2	2.8	3.1
5.4	2.8	3.1
5.6	2.8	3.1
5.8	2.9	3.2
6.0	2.9	3.2
6.2	3.0	3.2
6.4	3.0	3.2
6.6	3.0	3.3
6.8	1.7	2.7
7.0	1.4	1.5

TOTAL GROWTH VOLUME 0.40E-01 CM^3

SEQUENCE NUMBER IV

FILM 11

DISTANCE FROM SUBSTRATE (MM)	MEAN SIDE WIDTH (MM)	MEAN TOP/ BOTTOM WIDTH (MM)
0.1	2.0	2.2
0.2	1.9	2.4
0.3	1.9	2.8
0.4	1.9	2.8
0.5	1.9	2.9
0.6	1.9	2.7
0.7	1.9	2.7
0.8	1.9	2.7
0.9	1.7	2.8
1.0	1.8	2.6
1.1	1.8	2.6
1.2	1.7	2.5
1.3	1.6	2.6
1.4	1.2	2.6
1.5	1.1	2.7
1.6	0.9	1.7
1.7	0.8	1.7
1.8	0.6	1.0
1.9	0.5	1.0
2.0	0.6	0.9
2.2	0.4	1.1
2.4	0.2	0.9
2.6	0.0	0.3
2.8	0.0	0.1

TOTAL GROWTH VOLUME 0.75E-02 CM^3

Tables 38 and 39. As in Tables 34 and 35.

SEQUENCE NUMBER V

FILM 12

DISTANCE FROM SUBSTRATE (MM)	MEAN SIDE WIDTH (MM)	MEAN TOP/ BOTTOM WIDTH (MM)
0.1	1.7	2.0
0.2	1.7	2.1
0.3	1.8	2.1
0.4	1.7	2.1
0.5	1.7	2.1
0.6	2.0	2.1
0.7	2.2	2.2
0.8	2.1	2.2
0.9	2.1	2.1
1.0	1.9	1.9
1.1	2.0	1.9
1.2	2.0	1.9
1.3	1.9	1.8
1.4	1.9	2.0
1.5	1.8	1.8
1.6	1.8	1.7
1.7	1.4	1.9
1.8	1.2	1.8
1.9	0.9	1.8
2.0	1.0	1.2
2.2	0.5	1.0
2.4	0.0	0.3

TOTAL GROWTH VOLUME 0.69E-02 CM^3

SEQUENCE NUMBER VI

FILM 12

DISTANCE FROM SUBSTRATE (MM)	MEAN SIDE WIDTH (MM)	MEAN TOP/ BOTTOM WIDTH (MM)
0.1	1.5	1.4
0.2	1.4	1.4
0.3	1.5	1.4
0.4	1.5	1.5
0.5	1.6	1.7
0.6	1.7	1.7
0.7	1.7	1.7
0.8	1.8	1.8
0.9	1.9	1.8
1.0	2.0	1.8
1.1	2.0	1.9
1.2	2.0	1.8
1.3	2.1	1.7
1.4	2.2	1.8
1.5	2.3	1.9
1.6	2.4	1.9
1.7	2.4	1.9
1.8	2.5	1.9
1.9	2.6	2.0
2.0	2.4	2.1
2.2	2.3	2.0
2.4	2.3	1.9
2.6	2.4	2.1
2.8	2.4	2.1
3.0	2.5	2.2
3.2	2.6	2.3
3.4	2.6	2.3
3.6	2.8	2.4
3.8	2.6	2.4
4.0	2.6	2.5
4.2	2.6	2.5
4.4	2.7	2.5
4.6	2.8	2.5
4.8	2.7	2.6
5.0	2.8	2.6
5.2	2.8	2.7
5.4	2.9	2.7
5.6	2.9	2.9
5.8	2.9	3.0
6.0	2.2	2.6
6.2	0.2	0.7

TOTAL GROWTH VOLUME 0.33E-01 CM^3

Tables 40 and 41. As in Tables 34 and 35.

SEQUENCE NUMBER VII

FILM 13

DISTANCE FROM SUBSTRATE (MM)	MEAN SIDE WIDTH (MM)	MEAN TOP/ BOTTOM WIDTH (MM)
0.2	1.6	1.5
0.4	1.7	1.7
0.6	1.7	1.9
0.8	1.7	1.9
1.0	1.7	1.9
1.2	1.7	2.2
1.4	1.8	2.1
1.6	2.0	2.2
1.8	2.1	2.2
2.0	2.2	2.4
2.2	2.2	2.3
2.4	2.1	2.4
2.6	2.2	2.4
2.8	2.1	2.6
3.0	2.2	2.6
3.2	2.2	2.6
3.4	2.3	2.8
3.6	2.3	2.9
3.8	2.4	2.9
4.0	2.4	2.9
4.2	2.5	2.9
4.4	2.5	3.0
4.6	2.4	3.1
4.8	2.4	3.1
5.0	2.5	3.2
5.2	2.6	3.1
5.4	2.6	3.1
5.6	2.6	3.1
5.8	2.7	3.2
6.0	2.8	3.3
6.2	2.8	3.4
6.4	2.9	3.4
6.6	2.9	3.5
6.8	3.0	3.5
7.0	3.1	3.6
7.2	3.1	3.6
7.4	3.0	3.6
7.6	3.0	3.6

TOTAL GROWTH VOLUME 0.52E-01 CM^3

SEQUENCE NUMBER VIII

FILM 13

DISTANCE FROM SUBSTRATE (MM)	MEAN SIDE WIDTH (MM)	MEAN TOP/ BOTTOM WIDTH (MM)
0.1	1.8	2.0
0.2	2.2	2.2
0.3	2.2	2.4
0.4	2.3	2.6
0.5	2.7	2.8
0.6	3.0	2.7
0.7	3.0	2.8
0.8	3.1	2.8
0.9	3.0	2.7
1.0	2.9	2.6
1.1	3.1	2.4
1.2	3.1	2.4
1.3	3.1	2.5
1.4	3.0	2.4
1.5	3.1	2.4
1.6	3.1	2.5
1.7	3.1	2.5
1.8	3.2	2.4
1.9	3.1	2.5
2.0	3.1	2.5
2.2	2.3	2.2
2.4	1.2	1.5
2.6	0.1	0.4
2.8	0.0	0.1

TOTAL GROWTH VOLUME 0.16E-01 CM^3

Tables 42 and 43. As in Tables 34 and 35.

SEQUENCE NUMBER IX

FILM 14

DISTANCE FROM SUBSTRATE (MM)	MEAN SIDE WIDTH (MM)	MEAN TOP/ BOTTOM WIDTH (MM)
0.1	2.1	2.4
0.2	2.0	2.0
0.3	2.0	1.9
0.4	3.6	1.5
0.5	3.6	1.4
0.6	3.6	1.3
0.7	3.8	1.4
0.8	3.6	1.4
0.9	3.6	1.6
1.0	3.7	1.4
1.1	3.6	1.6
1.2	4.1	1.6
1.3	4.2	1.6
1.4	4.3	1.7
1.5	4.4	1.6
1.6	4.5	1.7
1.7	4.5	1.9
1.8	4.5	1.8
1.9	4.2	1.9
2.0	4.1	2.0
2.2	3.6	2.0
2.4	3.3	2.0
2.6	1.7	1.4
2.8	0.8	1.3
3.0	0.2	0.7
3.2	0.0	0.5

TOTAL GROWTH VOLUME 0.16E-01 CM^3

SEQUENCE NUMBER X

FILM 14

DISTANCE FROM SUBSTRATE (MM)	MEAN SIDE WIDTH (MM)	MEAN TOP/ BOTTOM WIDTH (MM)
-0.8	0.0	0.8
-0.7	0.9	1.9
-0.6	1.4	1.9
-0.5	1.1	1.6
-0.4	1.0	1.7
-0.3	1.0	0.7
-0.2	1.0	1.0
-0.1	1.0	1.0
0.0	1.2	1.4
0.1	1.1	1.4
0.2	0.7	1.3
0.3	0.7	1.4
0.4	0.8	1.6
0.5	0.8	0.5
0.6	0.4	0.3
0.7	0.2	0.1

TOTAL GROWTH VOLUME 0.18E-02 CM^3

Tables 44 and 45. As in Tables 34 and 35.

SEQUENCE NUMBER XI

FILM 15

DISTANCE FROM SUBSTRATE (MM)	MEAN SIDE WIDTH (MM)	MEAN TOP/ BOTTOM WIDTH (MM)
0.1	0.4	0.9
0.2	0.8	0.9
0.3	0.8	1.0
0.4	1.0	1.0
0.5	1.0	1.1
0.6	1.0	1.1
0.7	1.1	1.3
0.8	1.2	1.2
0.9	1.3	1.4
1.0	1.3	1.4
1.1	1.2	1.4
1.2	1.0	1.1
1.3	0.7	0.9
1.4	0.5	1.0
1.5	0.4	0.8
1.6	0.0	0.2

TOTAL GROWTH VOLUME 0.16E-02 CM^3

SEQUENCE NUMBER XII

FILM 15

DISTANCE FROM SUBSTRATE (MM)	MEAN SIDE WIDTH (MM)	MEAN TOP/ BOTTOM WIDTH (MM)
0.2	1.4	1.6
0.4	1.5	1.7
0.6	1.7	1.7
0.8	1.9	1.7
1.0	2.0	1.7
1.2	2.0	1.9
1.4	2.1	2.1
1.6	2.1	2.0
1.8	2.1	2.1
2.0	2.2	2.2
2.2	2.2	2.3
2.4	2.4	2.4
2.6	2.3	2.4
2.8	2.3	2.5
3.0	2.5	2.5
3.2	2.5	2.5
3.4	2.3	2.6
3.6	2.3	2.7
3.8	2.4	2.9
4.0	2.4	2.9
4.2	2.5	2.9
4.4	2.5	3.0
4.6	2.6	3.0
4.8	2.6	3.1
5.0	2.6	3.0
5.2	2.7	3.0
5.4	2.8	3.1
5.6	2.9	3.2
5.8	2.9	3.2
6.0	3.0	3.2
6.2	3.0	3.3
6.4	3.0	3.4
6.6	2.9	3.4
6.8	3.0	3.4
7.0	0.0	3.4

TOTAL GROWTH VOLUME 0.44E-01 CM^3

APPENDIX E

THE MAGONO AND LEE METEOROLOGICAL CLASSIFICATION OF SNOW CRYSTALS

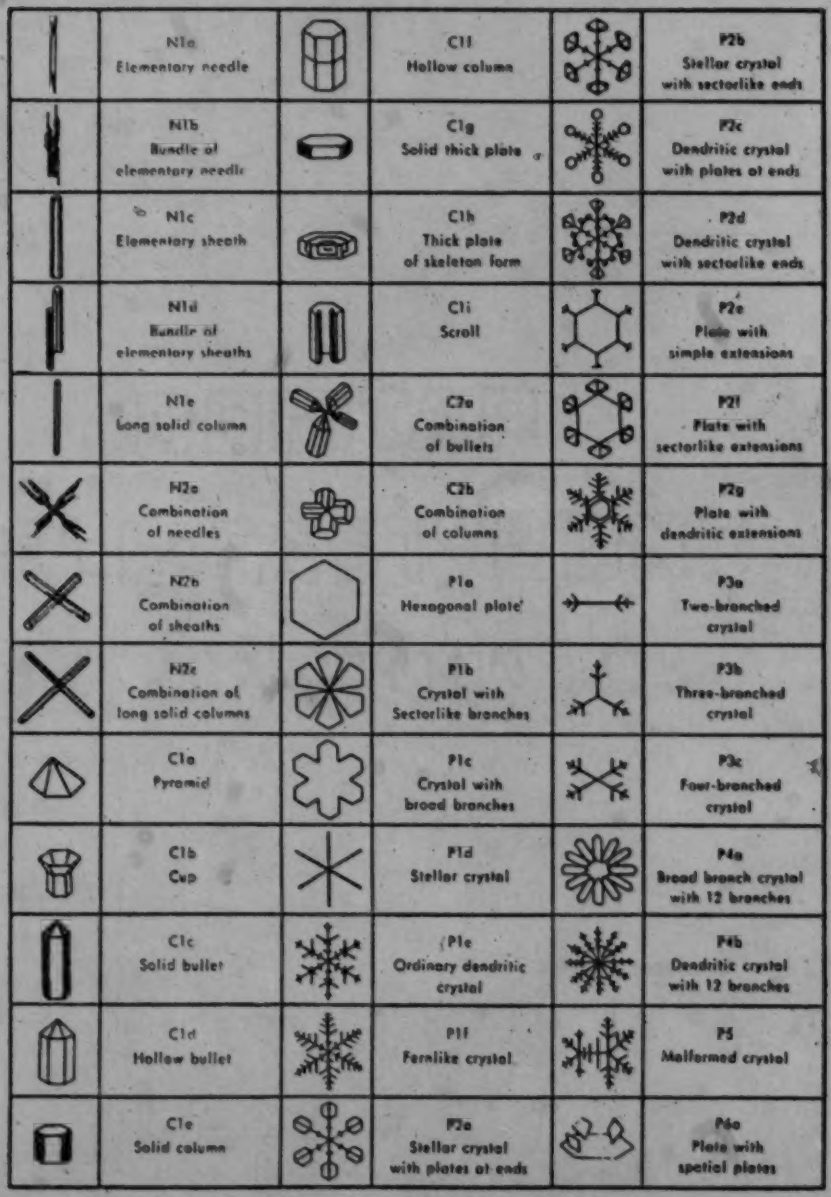

N1a Elementary needle	C1l Hollow column	P2b Stellar crystal with sectorlike ends
N1b Bundle of elementary needle	C1g Solid thick plate	P2c Dendritic crystal with plates at ends
N1c Elementary sheath	C1h Thick plate of skeleton form	P2d Dendritic crystal with sectorlike ends
N1d Bundle of elementary sheaths	C1i Scroll	P2e Plate with simple extensions
N1e Long solid column	C2a Combination of bullets	P2f Plate with sectorlike extensions
N2a Combination of needles	C2b Combination of columns	P2g Plate with dendritic extensions
N2b Combination of sheaths	P1a Hexagonal plate	P3a Two-branched crystal
N2c Combination of long solid columns	P1b Crystal with Sectorlike branches	P3b Three-branched crystal
C1a Pyramid	P1c Crystal with broad branches	P3c Four-branched crystal
C1b Cup	P1d Stellar crystal	P4a Broad branch crystal with 12 branches
C1c Solid bullet	P1e Ordinary dendritic crystal	P4b Dendritic crystal with 12 branches
C1d Hollow bullet	P1f Fernlike crystal	P5 Malformed crystal
C1e Solid column	P2a Stellar crystal with plates at ends	P6a Plate with spatial plates

Fig. 20a. The Magono and Lee (1966) meteorological classification of snow crystals. (from LaChapelle, 1969)

	P4b Plate with spatial dendrites		CP3d Plate with scrolls at ends		R3c Graupel-like snow with nonrimed extensions
	P4c Stellar crystal with spatial plat		S1 Side planes		R4a Hexagonal graupel
	P4d Stellar crystal with spatial dendrites		S2 Scalelike side plates		R4b Lump graupel
	P7a Radiating assemblage of plates		S3 Combination of side planes, bullets, and columns		R4c Conelike graupel
	P7b Radiating assemblage of dendrites		R1a Rimed needle crystal		I1 Ice particle
	CP1a Column with plates		R1b Rimed columnar crystal		I2 Rimed particle
	CP1b Column with dendrites		R1c Rimed plate or sector		I3a Broken branch
	CP1c Multiple capped column		R1d Rimed stellar crystal		I3b Rimed broken branch
	CP2a Bullet with plates		R2a Densely rimed plate or sector		I4 Miscellaneous
	CP2b Bullet with dendrites		R2b Densely rimed stellar crystal		G1 Minute column
	CP3a Stellar crystal with needles		R2c Stellar crystal with rimed spatial branches		G2 Germ of skeleton form
	CP3b Stellar crystal with columns		R3a Graupel-like snow of hexagonal type		G3 Minute hexagonal plate
	CP3c Stellar crystal with scrolls at ends		R3b Graupel-like snow of lump type		G4 Minute stellar crystal
					G5 Minute assemblage of plates
					G6 Irregular germ

Fig. 20b. The continuation of Fig. 20a.